REMOTE SENSING STUDIES AND MORPHOTECTONIC INVESTIGATIONS IN AN ARID RIFT SETTING, BAJA CALIFORNIA, MEXICO

A Dissertation

by

HESHAM FAROUK EL-SOBKY

Submitted to the Office of Graduate Studies of
Texas A&M University
in partial fulfillment of the requirements for the degree of

DOCTOR OF PHILOSOPHY

August 2007

Major Subject: Geology

REMOTE SENSING STUDIES AND MORPHOTECTONIC INVESTIGATIONS IN AN ARID RIFT SETTING, BAJA CALIFORNIA, MEXICO

A Dissertation

by

HESHAM FAROUK EL-SOBKY

Submitted to the Office of Graduate Studies of
Texas A&M University
in partial fulfillment of the requirements for the degree of

DOCTOR OF PHILOSOPHY

Approved by:

Co-Chairs of Committee,	Steven L. Dorobek
	Vatche P. Tchakerian
Committee Members,	Joel Watkins
	Raghavan Srinivasan
Head of Department,	John Spang

August 2007

Major Subject: Geology

ABSTRACT

Remote Sensing Studies and Morphotectonic Investigations in an Arid Rift Setting, Baja California, Mexico. (August 2007)

Hesham Farouk El-Sobky, B.S., Alexandria University;

M.S., Alexandria University

Co-Chairs of Advisory Committee: Dr. Steven L. Dorobek
Dr. Vatche P. Techakerian

The Gulf of California and its surrounding land areas provide a classic example of recently rifted continental lithosphere. The recent tectonic history of eastern Baja California has been dominated by oblique rifting that began at ~12 Ma. Thus, extensional tectonics, bedrock lithology, long-term climatic changes, and evolving surface processes have controlled the tectono-geomorphological evolution of the eastern part of the peninsula since that time. In this study, digital elevation data from the Shuttle Radar Topography Mission (SRTM) from Baja California were corrected and enhanced by replacing artifacts with real values that were derived using a series of geostatistical techniques. The next step was to generate accurate thematic geologic maps with high resolution (15-m) for the entire eastern coast of Baja California. The main approach that we used to clearly represent all the lithological units in the investigated area was object-oriented classification based on fuzzy logic theory. The area of study was divided into twenty-two blocks; each was classified independently on the basis of its own defined membership function. Overall accuracies were 89.6 %, indicating that this approach was highly recommended over the most conventional classification techniques.

The third step of this study was to assess the factors that affected the geomorphologic development along the eastern side of Baja California, where thirty-four drainage basins were extracted from a 15-m-resolution absolute digital elevation model (DEM). Thirty morphometric parameters were extracted; these parameters were then reduced using principal component analysis (PCA). Cluster analysis classification defined four major groups of basins. We extracted stream length-gradient indices, which highlight the differential rock uplift that has occurred along fault escarpments bounding the basins. Also, steepness and concavity indices were extracted for bedrock channels within the thirty-four drainage basins.

The results were highly correlated with stream length-gradient indices for each basin. Nine basins, exhibiting steepness index values greater than 0.07, indicated a strong tectonic signature and possible higher uplift rates in these basins. Further, our results indicated that drainage basins in the eastern rift province of Baja California could be classified according to the dominant geomorphologic controlling factors (i.e., fault-controlled, lithology-controlled, or hybrid basins).

This dissertation is dedicated to
my beloved wife, Dr. *Yousra Soliman*,
my sweet lovely angels, *Mohanad* and *Yazeed*, and
my kind beloved parents.

ACKNOWLEDGMENTS

The dissertation work is not solely the product of the student. Committee members, other faculty members, family, and friends all play important roles in the completion of the degree. I am grateful to all of them.

I especially thank my committee co-chair, Dr. Steve Dorobek, for his unceasing moral, financial and scientific support and his invaluable and thorough critical reviews of my proposals and dissertation. I am extremely grateful to him for having me as a member of his team, working under his supervision, where I gained invaluable experience. Without him, this work would not have been possible and could not have been completed.

I thank my committee co-chair, Dr. Vatche Tchakerian for his unconditional support and guidance, for his prompt reviews of my work, and for his succinct scientific inputs. I thank Dr. Joel Watkins for helping me through the different stages of my research and for his interest in my work. He provided me with motivation, and he was exceptionally helpful during the different stages of my study. I am extremely grateful for Dr. Raghavan Srinivasan for his guidance, support, and the remote sensing facilities that he provided through the different stages of my research

I would like to thank NASA for funding most of my study at Texas A&M University through the Earth System Science fellowship merit award. Thanks also to ConocoPhillips and to the AAPG for supporting part of my studies.

I am grateful to the Department of Geology and Geophysics at Texas A&M University for the assistantships they provided. Thanks to the faculty, staff members, and

my colleagues in the Department of Geology and Geophysics, who made my study at A&M a great experience.

I am very grateful and thankful to my beloved family for their endless care and support. I am grateful to my wife, Yousra, who has always been encouraging and supportive. I would also like to thank my beloved sons, the most beautiful things in this world, Mohanad and Yazeed, for their love and outstanding and highly appreciated patience. I am very grateful to my kind parents for their endless support from the very beginning and for their prayers throughout my life.

TABLE OF CONTENTS

CHAPTER Page

LIST OF TABLES

Page

LIST OF FIGURES

Page

Page

Page

CHAPTER I

GENERAL INTRODUCTION

I.1. Overview

The Gulf of California and surrounding land areas provide a classic example of recently rifted continental lithosphere, where back-arc stretching of a continental volcanic arc has culminated in the ongoing seafloor spreading that characterizes the present-day axis of the gulf. The recent tectonic history of eastern Baja California, which includes most of the land area eastward of the main drainage divide that extends north-south along the length of the peninsula, has been controlled by oblique rifting. This rifting began at about 12 Ma and has separated the peninsula of Baja California from mainland Mexico. Thus, extensional tectonics, bedrock lithology, long-term climatic changes, and evolving surface processes have controlled the tectono-geomorphological evolution of the eastern part of the peninsula since 12 Ma. No previous studies, however, have examined the current tectono-geomorphologic characteristics of eastern Baja California resulting from the combined effects of these factors.

The proposed study will investigate several important themes or concepts in modern tectono-geomorphologic studies, using the present-day eastern part of Baja California as an ideal analog for intracontinental rift systems in arid climatic settings. The present-day arid climatic conditions and meager vegetative cover across Baja California make this

---

This dissertation follows the style of *Photogrammetric Engineering and Remote Sensing*.

area especially favorable for tectono-geomorphologic analysis using remote sensing techniques. In addition, the numerous rift basins along the entire length of the peninsula and their various stages of tectonic evolution (from tectonically inactive to ongoing displacements along basin-bounding faults) also make the area suitable for statistical analyses of various morphometric indices that characterize the topography and drainage networks within each rift basin.

The proposed study will utilize remote sensing data, various software packages, and statistical analyses to investigate the tectono-geomorphologic evolution of the eastern rift province of Baja California. Although satellite data only provide images of present-day landforms, the arid climate of the peninsula and the relatively short phase of post-rift history for most basins (some basin-bounding faults are still seismically active) allow remnants of many rift-generated geomorphologic features to be preserved to varying degrees across the eastern part of the peninsula. Thus, the numerous rift basins of eastern Baja California provide sufficient examples for investigating the relative influence of various geological factors on the tectono-geomorphological evolution of these basins.

I.2. Introduction to Baja California, Mexico

Baja California is an excellent location to study continental rifting processes because: (1) offshore Gulf of California is an area of active rifting; (2) the history of extension and regional geology of Baja California are reasonably well understood; (3) the study area is an arid to semi-arid region, where limited vegetation makes remote

sensing an excellent tool for regional geologic mapping and analysis; and (4) Baja California is highly accessible for field work.

Baja California is a peninsula bounded to the west by the Pacific Ocean and to the east by the Gulf of California (also known as the Sea of Cortez). The proposed study will focus on the Neogene extensional province, which is mainly found along the eastern side of the peninsular divide.

I.3. Geology and tectonics framework for Baja California

The Gulf of California rift forms a geologically young and active plate boundary that links the San Andreas strike-slip fault system in California to the oceanic spreading system of the East Pacific Rise. Previous tectonic and structural studies suggest a complex geological evolution for the Gulf of California and surrounding continental regions (Hamilton, 1961; Atwater, 1970; Karig and Jensky, 1972; Mammerickx and Klitgord, 1982; Gastil *et al.*, 1983; Lonsdale, 1989; Stock and Hodges, 1989). Baja California is also an excellent modern example of a continental block, or terrain that has been horizontally translated ~ 300 km to the NW because of highly oblique rifting and sea floor spreading in the Gulf of California (Umhoefer and Dorsey, 1997). The peninsula was originally connected to the west coast of mainland Mexico but rifted and drifted away by differential movements of the Pacific and North American plates over the past 6-12 Myr.

The tectonic evolution of eastern Baja California has been controlled by dynamic processes of oblique continental rifting that are still poorly understood. Geologic

structures, geomorphologic features, and sedimentary basins along the eastern side of Baja California preserve a critical record of these processes.

Ochoa-Landín (1998) recently summarized the geologic evolution of the Gulf of California and Baja California from ~ 23 Ma to the present. During Oligocene time, an eastward-dipping subduction zone had developed along the Pacific side of Baja due to subduction of the Farallon plate beneath the western margin of North America (McDowell and Clabaugh, 1979; Sawlan and Smith, 1984). Subduction of oceanic lithosphere created a north-south trending volcanic arc along nearly the entire length of Baja from ~ 24-11Ma (Atwater, 1970; Stock and Hodges, 1989). As subduction slowed during Middle Miocene time, parts of western North America became coupled to the Pacific Plate along the former subduction zone (Atwater, 1989; Stock and Hodges, 1989; Nicholson *et al.*, 1994; Bohannon and Parsons, 1995), causing initial riftting in the Gulf of California, the formation of a new plate boundary there, and the transfer of Baja California lithosphere onto the Pacific Plate. According to Dickinson and Snyder (1979), eastward-directed subduction was terminated as a transform boundary began to develop at the northern end of Baja California, with the northward migrating Mendocino triple junction simultaneous with southward migrating Rivera triple junction, and the start of transform shear. Gans (1997) suggested that the transform boundary had a collinear position with respect to the trench and maintained a stable configuration until about 5.5 Ma when the plate boundary moved into the Gulf of California. Subduction stopped at ~12 Ma (Middle Miocene), which has been related to the shutdown of spreading along the Pacific-Guadalupe ridge (Mammerickx and Klitgord, 1982).

Extension in the Gulf of California began at ~12 Ma, in an east-west to northeast–southwest direction, roughly orthogonal to the trend of normal faults that formed during rifting (Angelier, 1981 *et al.*; Atwater, 1989; Lonsdale, 1991; Stock and Hodges, 1989; Stock and Lee, 1994; Axen, 1995; Lee *et al.*, 1996; Axen *et al.*, 2000). Also near the Santa Rosalia Basin, Sawlan and Smith (1984) recognized that the onset of crustal extension coincided with a coeval change in volcanism from calcalkaline to transitional-calcalkaline at around 12-10 Ma. This extension is responsible for the translation of Baja California as much as 100-150 km WSW relative to North America before about 5.5 Ma (Late Miocene). The complete translation of Baja California from the North American plate to the Pacific Plate is related to the activation and connection of the San Andreas Fault system with the East Pacific Rise, which has been dated at about 3.5 Ma (Lonsdale 1991, Stock and Hodges 1989). This connection may have increased displacement of Baja California from mainland Mexico more than 260 km due to dextral strike-slip displacement along the San Andreas Fault system and the initiation of seafloor spreading in the Gulf of California (Landin, 1998). On the other hand, Angelier *et al.* (1981) recognized N-S striking normal faults and NNW-SSE to NW-SE dextral-slip and oblique faults in the Pliocene to Recent strata of Santa Rosalia basin, which have been related to a clockwise rotation of the extension direction from NE-SW to E-W that is associated with dextral strike-slip motion along the San Andreas fault system. At present, nearly all of the modern Pacific-North American relative plate motion is accommodated within the axis of the Gulf of California and the Salton trough (e.g., Lonsdale, 1989; DeMets, 1995; Bennett *et al.*, 1996). The Baja California-North America spreading rate recorded by

magnetic anomalies in the axis of the gulf accelerated from ~43 mm/yr to ~51 mm/yr at ~0.78 Ma (DeMets, 1995; DeMets and Dixon, 1999; Spencer and Normark, 1979; Stock and Hodges, 1989). Recently, Axen *et al.* (2000) suggested that significant oblique rifting has probably characterized the gulf since at least ~8 Ma, and possibly throughout its history. Since ~6.5 Ma, most plate-margin translation has been concentrated in the gulf, where long dextral transforms link short spreading ridges (e.g., Lonsdale, 1989).

Baja California can be divided into three major domains (Umhoefer and Dorsey, 1997): 1) a northern domain, which extends from Puertecitos to the Salton trough, 2) a central domain, from latitude ~30°N to ~25°N, and 3) a southern domain, from latitude ~25°N to the mouth of the Gulf of California. These three main domains are defined by active transform faults in the gulf, as indicated by bathymetry (Larson *et al.*, 1968; Lonsdale, 1989), seismicity (Molnar, 1973; Goff *et al.*, 1987), and active onshore faults that cross the peninsula. In the northern domain, many strike-slip faults diverge westward from the transform faults offshore and cut across Baja California and southern California (e.g., Suarez- Vidal *et al.*, 1991). Thus, the active plate boundary is at least 200–300 km wide and is characterized by numerous strike-slip and normal faults (Umhoefer and Dorsey, 1997).

In the central domain, most seismicity occurs along major transform faults in the Gulf of California (Goff *et al.*, 1987), and there are no active faults cutting across Baja California. Geomorphic and seismic data suggest that an important, but probably minor, component of active faulting is occurring along the eastern margin of central Baja California. Umhoefer and Dorsey (1997) further divided the central domain into western

and eastern segments. The western part of the central domain is a largely unfaulted region of flat to gently inclined strata of the Miocene fore arc and older units. The eastern part of the peninsula and the narrow shelf in the Gulf of California, however, are part of the gulf extensional province, which contains virtually all of the structures related to rifting (Gastil *et al.*, 1975). A nearly continuous, east-facing rift escarpment forms the western boundary of the Gulf of California extensional province. In the southern domain, seismically active normal and oblique faults, especially the La Paz fault cut across Baja California (Normark and Curray, 1968). The relationship of these faults to the transform fault system offshore is unknown (Umhoefer and Dorsey, 1997).

I.4. Statement of the problem

In Baja California, no regional morphotectonic study has been done to investigate the role of the major forcing factors that have controlled the landscape of the peninsula, exposed lithology, tectonics, and climate. Climate and bedrock lithologies are relatively constant along the entire length of the eastern rift province, so tectonism has probably played a dominant role in the variable topographic evolution of this area.

Watersheds are the geomorphic boundary of terrestrial sedimentary basins and are typically composed of one or more drainage basins. Detailed study of the drainage basins in Baja California, including the extraction of drainage basin attributes (e.g., hill shades, aspects, slope, etc), along with multivariate statistics will reveal the role of extensional tectonics in controlling the geomorphology of the eastern rift province of Baja California.

I.5. Tectonic geomorphology of rift basins and Baja California

Drainage networks in continental rift basins are strongly linked to bedrock lithology, climate, fault systems, and surface processes, although quantitative measurements and statistical analyses that demonstrate any interdependent relationships between these factors are generally lacking.

Drainage networks can be demonstrably linked to the growth and linkage of extensional fault systems and regional development of topography in intracontinental rift systems (Leeder and Gawthorpe, 1987; Braun and Beaumont, 1989; Frostick and Reid, 1989; Gilchrist and Summerfield, 1990; Summerfield, 1991; Foster and Gleadow, 1992; ten Brink and Stern, 1992; Gawthorpe and Hurst, 1993; Arvidson *et al.*, 1994; Seidl *et al.*, 1996; Gawthorpe and Leeder, 2000; Contreras and Schultz, 2001; Doglioni *et al.*, 2003; 2005). Baja California represents a unique continental rift setting because older, volcanically constructed, topographic features are spatially juxtaposed and temporally overprinted by younger, rift-related structures and topographic patterns (El-Sobky and Dorobek, 2004). The similar climatic conditions along the length of Baja California, but variable timing and intensity of late Miocene to Recent rifting and the unique dimensions and bedrock lithologies of individual rift basins, means that the present-day tectono-geomorphologic characteristics of different basins likely reflect different stages in the tectonic evolution of each basin. In other words, the tectono-geomorphologic "maturity" of individual rift basins is most likely related to pre-rift topography, local variations in bedrock lithologies, and when the most recent displacements occurred along basin-bounding fault systems.

This study will investigate a number of different morphometric indices and analyze topographic and hypsometric profiles of individual rift basins to characterize the tectono-geomorphologic maturity of each basin. Preliminary analyses show that basins along the eastern side of Baja California can be subdivided into several basin types:

- *Immature basins,* which are bounded by obvious fault scarps or abrupt and steep topographic inflections along the edges of basins. These abrupt topographic changes along the basin edges suggest recent vertical displacements on basin-bounding faults. Other characteristics of tectono-geomorphologically immature basins include complex drainage networks and stream ordering relationships, stream and valley incisions that have very little accumulated sediment at the present time, steep alluvial-fan surfaces, and trunk streams that are shifted toward axial positions near recently active normal faults that bound the basin.
- *Transitional basins,* which are in intermediate stages of tectono-geomorphologic evolution. Remnant rift-generated topography is still preserved, although subdued by the combined effects of erosion and sediment accumulation. Topographic and hypsometric profiles across transitional basins are highly variable, even within the same basin, which indicates that these basins are evolving into more mature basins.
- *Mature basins,* with basin margins that are not obviously fault-bounded. Fault scarps are not apparent, topographic and hypsometric profiles from basin flanks to basin centers are generally concave upward and fairly consistent across

individual basins, and many fluvial incisions are floored by significant sediment accumulations.

I.6. Objectives

I will investigate longer term geomorphologic and drainage-network evolution across the study area by examining all scales of stream development and how they relate to tectonically generated topography and bedrock lithologies. I am particularly interested in areas where stream profiles and stream patterns are not in equilibrium with more regional topographic profiles, which would suggest that the streams are in the process of adjusting to previous surface deformations. I will also investigate how stream patterns are influenced by local structural features.

The particular objectives of the project proposed here are threefold: 1) to generate 15-m spatial resolution absolute DEM for the study area and provide these data for the research community in the public domain, 2) to investigate the implementation of the object-oriented classification and stacked-vector techniques to generate a high-resolution hybrid classified map for the study area, and 3) to study the role of crustal deformation during rifting and tectonic reactivation in determining the geometry and distribution of extensional faults and their effects on drainage basins.

I.7. Data and resources

The required data for this study include: (1) LANDSAT 7 ETM+ satellite images, (2) ASTER satellite images, (3) SRTM digital elevation model (DEM) data, (4) topographic

maps, (5) geological maps, and (6) ground control points (GCPs). LANDSAT ETM+ images were acquired for the entire study area from the USGS. Six scenes will be used in this study, which cover about two-thirds of the peninsula. The images will be utilized to verify and/or enhance the surface geology. Thirty-two ASTER images were also acquired, which cover the eastern rift province of the peninsula. The ASTER images will be used to generate a relative DEM with 15-m spatial resolution. The shuttle radar topographic mission (SRTM) DEM data have also been acquired for the study area from the USGS (1:250,000 scale data at 90-m resolution). These data will be enhanced using appropriate geostatistical techniques, which after resampling and integration with the ASTER data will be used to generate an absolute 15-m spatial resolution DEM. The SRTM digital elevation is available in 1° x 1° blocks (geographic coordinate system, WGS 1972 datum, units are decimal degrees) and requires some processing before conducting any geological analyses. 1:50,000 topographic maps are available and cover most of the peninsula. A representative number of GCPs scattered across the study area were collected using a hand -held GARMEN 72 GPS unit during field work in Junuary 2004.

I.8. Materials and methods

I.8.1. Digital elevation model and geostatistical manipulations

A DEM is crucial for this study, so much time and effort will be devoted to generating a reliable, robust, and precise DEM for the study area. The accuracy of the extracted morphometric parameters and indices rely completely on the accuracy and

precision of the derived DEM. DEMs are generally defined as binary raster files that have spatial elevation gridded in a regularly spaced pattern. In many earth and environmental science applications, DEMs serve as inputs for detailed spatial analyses, such as the determination of the extent of hydrographic networks and the classification of geological terrains (Moore *et al.* 1991; Weibel and Heller 1991; Kyriakidis *et al.* 1999). Tectonogeomorphic studies also need accurate and precise values for elevation of planetary surfaces. The shuttle radar topography mission (SRTM) DEM has 90-m spatial resolution and will be used in this study. The SRTM elevation data provide the most complete, high-resolution digital topographic database for Earth's surface. The SRTM data, however, contain artifacts and data gaps with null values, which appear as empty pixel elements in the DEM. For small areas, it is possible to use various interpolation methods to generate a DEM from the SRTM data that is completely free of such data gaps. For larger areas, however, interpolation becomes increasingly difficult. Null areas in the SRTM data are typically due to very steep relief, dense dark vegetation, very dark shadows, or the surface of bodies of water.

Artifacts and data gaps in the SRTM data can be removed or filled with estimated values that resemble true values by using various geostatistical techniques. Increasing the resolution of the SRTM DEM beyond its actual spatial limits is also an objective.

The power of geostatistical approaches lies in their ability to honor any intrinsic spatial information associated with regionalized variables. Geostatistics is distinct from conventional statistical techniques in that: 1) geological origins of the data are considered, 2) geostatistical methods provide definite modeling and treatment of spatial

correlations between data, and 3) geostatistical methods have the ability to handle data at different scales and levels of precision (Deutsch, 2002). In the present study, ordinary kriging and cokriging methods will be used to fill missing data in the original SRTM DEM. Results from ordinary kriging and cokriging methods can then be compared to evaluate the accuracy of the estimated values for the data gaps in the SRTM DEM. In the cokriging method, altitude is used as a primary or hard variable and co-regionalized with the reflectance attribute. The reflectance attribute is generated by summing the transformed spectral reflectance bands using the ACE (alternating conditional expectation) approach. The reflectance attribute is then used as a secondary or soft variable and formalized in a coherent set of variograms, one for the hard variable, one for the soft variable, and the cross-variogram between the pair of variables involved in the estimation (cf. Atkinson *et al.*, 1992).

The gap-free SRTM DEM generated using the new technique developed during early stages of this study (El-Sobky and Dorobek, in review) is very important, especially when involved in any automated computational algorithms. For example, automated extraction of the various morphometric indices using a gap-free DEM is more convenient, accurate, and fast, and the computing algorithm will not suffer any complications while running.

I.8.2. Object-oriented classification

Classification of satellite imagery is the process of clustering data into a number of uniquely identified classes that have similar spectral characteristics. Clustering is based

on the degree of similarity and dissimilarity between the different groups, so data points that belong to the same group should be highly similar, but dissimilar to the other groups. Unfortunately, different results can be achieved for the same data set by implementing different classification algorithms (Benediktsson *et al.*, 1990a, b; Hepner *et al.*, 1990; Key *et al.*, 1989; Bischof *et al.*, 1992; Kanellopoulos *et al.*, 1992; Civco, 1993; Paola and Schowengerdt, 1994; Solaiman and Mouchot, 1994; Skidmore *et al.*, 1997). Development of an optimal classification algorithm is a challenging problem (Ho *et al.*, 1994) and no image classifier provides perfect results (Matsuyama, 1989). Thus, Kanellopoulos *et al.* (1993) and Brown *et al.* (2000) suggested that combining classifiers could be a useful and practical approach to increase classification accuracy as well as optimize classification performance.

Input data sets typically play a critical role in guiding the selection of an appropriate algorithm for the classification process. An object-oriented classification technique is chosen for the present study to perform the classification tasks. The concept behind object-oriented classification is that classification is based on the image objects and their mutual relationships rather than on the characteristics of a single pixel. The strength of this technique is that it utilizes a broad spectrum of different object features, such as spectral values, shape, or texture, for classification. However, in order to deal with a multisource classification, an augmented- vector method (also known as stacked-vector methods) will be used. According to Tso and Mather (2001), there are three main issues involved with using this method. The first issue is the possible differences in scale and measurements of each data source. To overcome this problem a normal score transform

(NST) will be used. An NST is a graphical transform that allows one to normalize any distribution, regardless of its shape. The NST algorithm will be used to transform the multisource data sets into normal distribution and to normalize each data set, such that the mean has zero value and standard deviation equals unity. The second issue is the computationally intensive nature of this method. Reducing the numbers of data vectors is the best way to reduce the computational requirements of this technique. Data reliability or uncertainty comprises the third issue of this technique. To overcome this problem, input vectors will be assigned different weights in the object-oriented classification algorithm based on the degree of correlation between these vectors and the separability analysis.

I.8.3. Tectonics and evolution of topography and drainage networks

The links between tectonically generated topography and surficial drainage networks have been investigated in a number of tectonic settings (e.g., compressional orogens and their associated foreland basins: Tucker and Slingerland, 1996; Schlunegger *et al.*, 1998; Kühni and Pfiffner, 2001; Schlunegger and Hinderer, 2001; intracontinental strike-slip deformation zones: Replumaz *et al.*, 2001), although intracontinental rift systems and their associated rift-flank uplifts have probably been investigated more extensively than any other setting (e.g., Braun and Beaumont, 1989; Frostick and Reid, 1989; Gilchrist and Summerfield, 1990; Summerfield, 1991; Foster and Gleadow, 1992; Ten Brink and Stern, 1992; Gawthorpe and Hurst, 1993; Arvidson *et al.*, 1994; Seidl *et al.*, 1996; Gawthorpe and Leeder, 2000; Doglioni *et al.*, 2003). Most tectonogeomorphologic

studies of intracontinental rift systems have focused on long-wavelength topographic variations that are most likely to be related to the deformation and rheological evolution of continental lithosphere during and after rifting. Far less research, however, has focused on more local structural features (e.g., individual half-graben elements and transfer fault zones) and the topographic and drainage patterns that are associated with these features. Even less is known about how local tectono-geomorphology is related to longer wavelength topographic variations. That is, there have been few integrated studies that have investigated all scales of geomorphologic and drainage evolution as they relate to various scales of tectonic deformation and tectonically generated topography (cf. Arvidson *et al.*, 1994).

In the present study I will use remote sensing data to characterize all scales of topographic variability across the eastern region of the peninsula that borders the Gulf of California. With respect to long-wavelength patterns of rift-flank uplift, I am particularly interested in how topographic patterns caused by younger transtensional deformation in the Gulf of California region have overprinted the older rift-flank uplift that formed during earlier, more orthogonal rifting phases.

I.8.4. Watersheds and basin geomorphometries

Baja California is an active tectonic region. In active tectonic settings, topographic features can be analyzed to quantitatively characterize the interactions between tectonics and surface processes, thus providing a basis for modeling landscape evolution. In this study, the tectonic geomorphology of the Baja rift province will be examined with

emphasis on the general topographic indices, drainage patterns, and major longitudinal profiles. A major goal is to express the influence of tectonics on drainage patterns, where streams adjust to the local tectonic deformation especially along the eastern side of the main peninsular divide. The main peninsular divide in Baja California is likely due to volcanically constructed topography that was enhanced by rift-flank uplift during Miocene to Recent time. Isostatic flexural uplift of the rift-flank keeps it high-standing, preventing the drainages from dissecting the landscape. As a result, the geomorphic expression of active normal faulting is expected. Results from this study may determine the time scales necessary for a landscape to transform from one tectonic and base level condition to another. Such different mechanisms for generating topography should impart a unique fingerprint in the resulting landforms (e.g. Wells *et al.*, 1988).

Similar hypotheses have been examined in the Italian Apennines, where geologic and geomorphic data reveal topographic evolution during the different phases of major plate convergence and crustal shortening (Castellarin *et al.*, 1986; Colella *et al.*, 1987; Thomson, 1994; Tortorici *et al.*, 1995; Argnani *et al.*, 1997; Bertotti *et al.*, 1997; Coltorti and Pieruccini, 2000).

The identification of drainage basins is an important process in both characterising a surface and in defining spatial units that are appropriately related to geomorphological processes. The 15-m spatial resolution DEM is fundamental for this study because fractal measures such as the perimeter (contour length) and the surface area of topography are a function of DEM spatial resolution.

Multivariate statistics such as factor analysis and cluster analysis will be an important tool used to manipulate the different derived topographic attributes as well as for facilitating the interpretations.

I.9. Significance of the present study

Baja California is kinematically linked to the Gulf of Claifornia rift system. Although this area has been studied extensively from the tectonic point of view, there is only a limited understanding of the relationships between progressive surface deformation and its effects on sedimentation, geohazard potential, and drainage-network and geomorphologic evolution, especially during the last few million years of deformation. Thus, understanding recent surface deformation will provide insight into the styles, rates, and processes of ongoing tectonic activity in this region.

Other studies in modern, tectonically active settings have shown that surficial drainage patterns provide important information on intermediate to longer term patterns of tectonic deformation and related surface deformations. Thus, an integrated study that combines analysis of recent surface deformations, mapped structural features, regional to local topographic patterns, and the evolution of drainage networks and alluvial depositional systems is essential for describing and explaining the links between tectonic deformation and erosion/sedimentation patterns across the Baja California region.

CHAPTER II

GEOSTATISTICAL TECHNIQUES FOR GENERATING HIGH-RESOLUTION GAP-FREE DEM FROM SRTM DATA

Shuttle radar topography mission (SRTM) digital elevation data from Baja California were corrected and enhanced by replacing artifacts with real values derived using a series of geostatistical techniques. Ordinary kriging was used initially to regionalize the DEM (hard variable) and provide estimates for missing data. A sum of transformed reflectance bands of the ETM+ images was derived by using the alternating conditional expectations (ACE) algorithm; these results were then used as a soft variable for cokriging. Modeled experimental semivariograms for both hard and soft variables and cross semivariograms for the spatially correlated variables were then evaluated using cross-correlation methods to assess the accuracy of the techniques. Cokriging was more accurate and efficient than ordinary kriging for retrieving the missing data and for creating more geologically realistic maps. This technique provides a new and accurate way to quantitatively correct and enhance DEMs and to incorporate spectral reflectance as a soft constraint for estimating missing values.

II.1. Introduction

Digital elevation models (or DEMs) are generally defined as binary raster files that have spatial elevation gridded in a regularly spaced pattern. In many earth and environmental science applications, DEMs serve as inputs for detailed spatial analyses, such as the determination of the extent of hydrographic networks and the classification of geological terrains (Moore *et al.* 1991; Weibel and Heller 1991; Kyriakidis *et al.* 1999). Tectonogeomorphic studies also need accurate and precise values for elevation of planetry surfaces. Shuttle Radar Topography Mission (SRTM) DEM with 90-m spatial resolution is used in the present study. The SRTM obtained elevation data on a near global scale to generate the most complete, high-resolution digital topographic database for Earth's surface. The SRTM data, however, contain artifacts and data gaps with null values, which appear as empty pixel elements in the DEM. For small areas, it is possible to use various interpolation methods to generate a DEM from the SRTM data that is completely free of such data gaps. For larger areas, however, this becomes increasingly difficult. Null areas in the SRTM data are typically due to very steep relief, dense dark vegetation, very dark shadows, or the surface of bodies of water.

The purpose of this study was to demonstrate that artifacts and data gaps in the SRTM data can be removed or filled with estimated values that resemble true values by using various geostatistical techniques. Increasing the resolution of the SRTM DEM beyond their actual spatial limits was also an objective.

The power of geostatistical approaches lies in their ability to honor any intrinsic spatial information associated with regionalized variables. Geostatistics is distinct from

conventional statistical techniques in that: 1) geological origins of the data are considered, 2) geostatistical methods provide definite modeling and treatment of spatial correlations between data, and 3) geostatistical methods have the ability to handle data at different scales and levels of precision (Deutsch, 2002). In the present study, ordinary kriging and cokriging methods were used to fill missing data in the original SRTM DEM. Results from ordinary kriging and cokriging methods were compared to evaluate the accuracy of the estimated values for the data gaps in the SRTM DEM. In the cokriging method, altitude was used as a primary or hard variable and co-regionalized with the reflectance attribute. The reflectance attribute was generated by summing the transformed spectral reflectance bands using the ACE approach. The reflectance attribute was then used as a secondary or soft variable and formalized in a coherent set of variograms, one for the hard variable, one for the soft variable, and the cross-variogram between the pair of variables involved in the estimation (cf. Atkinson *et al.*, 1992).

II.2. Previous studies

Geostatistical interpolations are commonly used in remote sensing studies to solve problems with greater accuracy and precision than conventional statistical methods (e.g, Addink and Stein, 1999; Lohani and Mason, 1999; Oliver *et al.*, 2000; Chica-Olmo and Hernandez, 2000; Herzfeld, 1999; Atkinson and Tate, 2000). In particular, kriging and cokriging techniques have been used with great success. For example, Lohani and Mason (1999) applied kriging and cokriging techniques to Airborne Thematic Mapper

(ATM) images to construct a DEM for a narrow and steep beach. Lloyd and Atkinson (2002) generated a digital surface model (DSM) from LiDAR data using both ordinary kriging and the kriging with trend model (also known as universal kriging). Regionalization theory is more successful than most other methods (e.g., time-series analysis, correlograms and Fourier transformation) because regionalization theory honors most natural phenomena captured by remote sensing methods, which are randomly or continuously distributed and commonly have high spatial variability across Earth's surface.

II.3. Methodology

The work flow for the methods described in this paper is shown in Figure 2.1.

II.3.1. Study area

The area under investigation (Baja California, Mexico) has a complex tectonic history and spectacular geomorphologic patterns (Figure 2.2). Developing a high-resolution artifact-free DEM for the peninsula using SRTM data is critical for identifying most tectonic features and for statistical analysis of the geomorphologic characteristics of the region.

Baja California is a ~ 1200-km-long by 50 to 200-km-wide peninsular that is bounded by the Gulf of California on the east and the Pacific Ocean on the west (Figure 2.2a). Our ongoing studies are focusing on the middle two-thirds of the peninsula

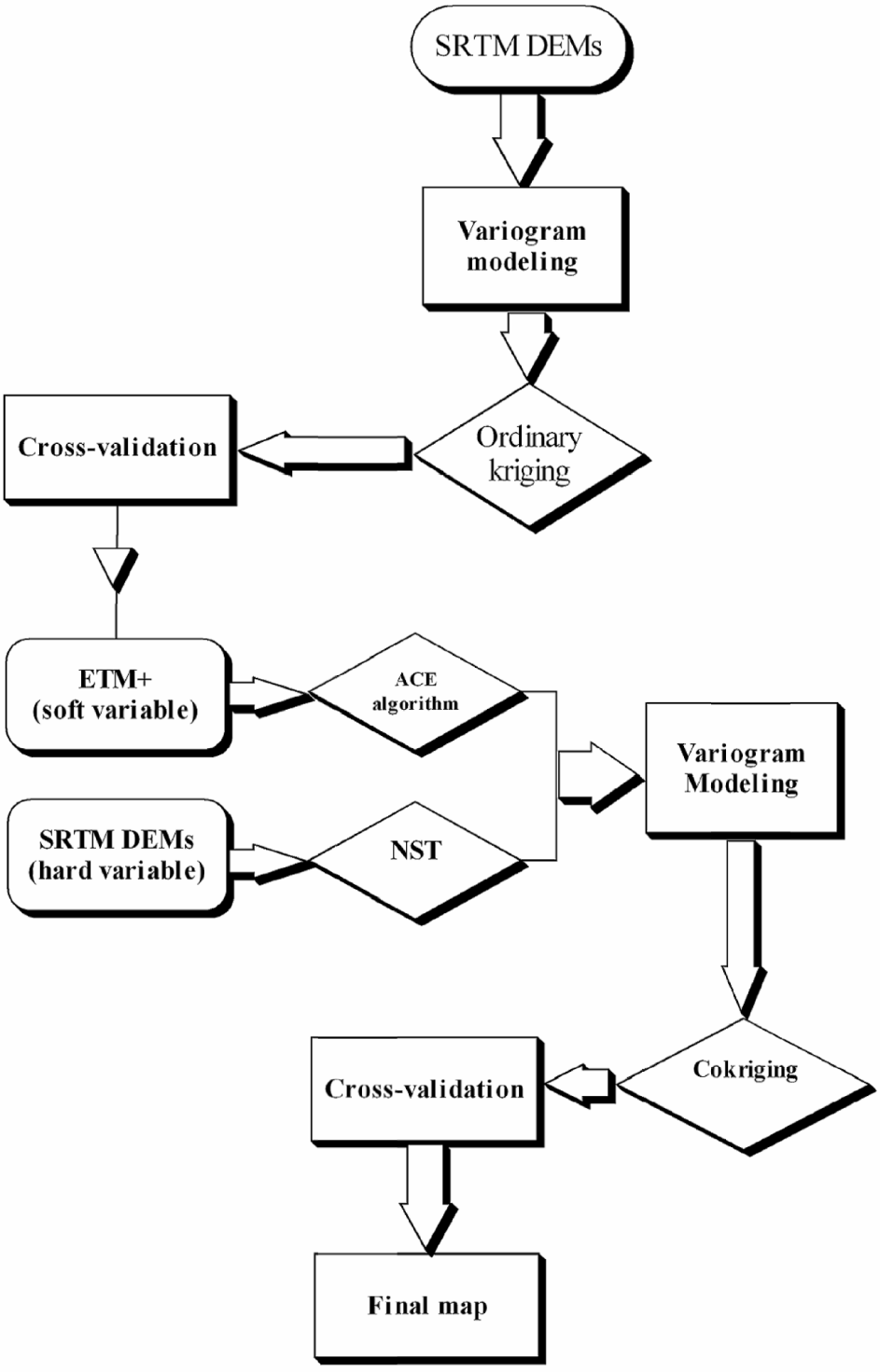

Figure 2.1. Work flow for the proposed technique.

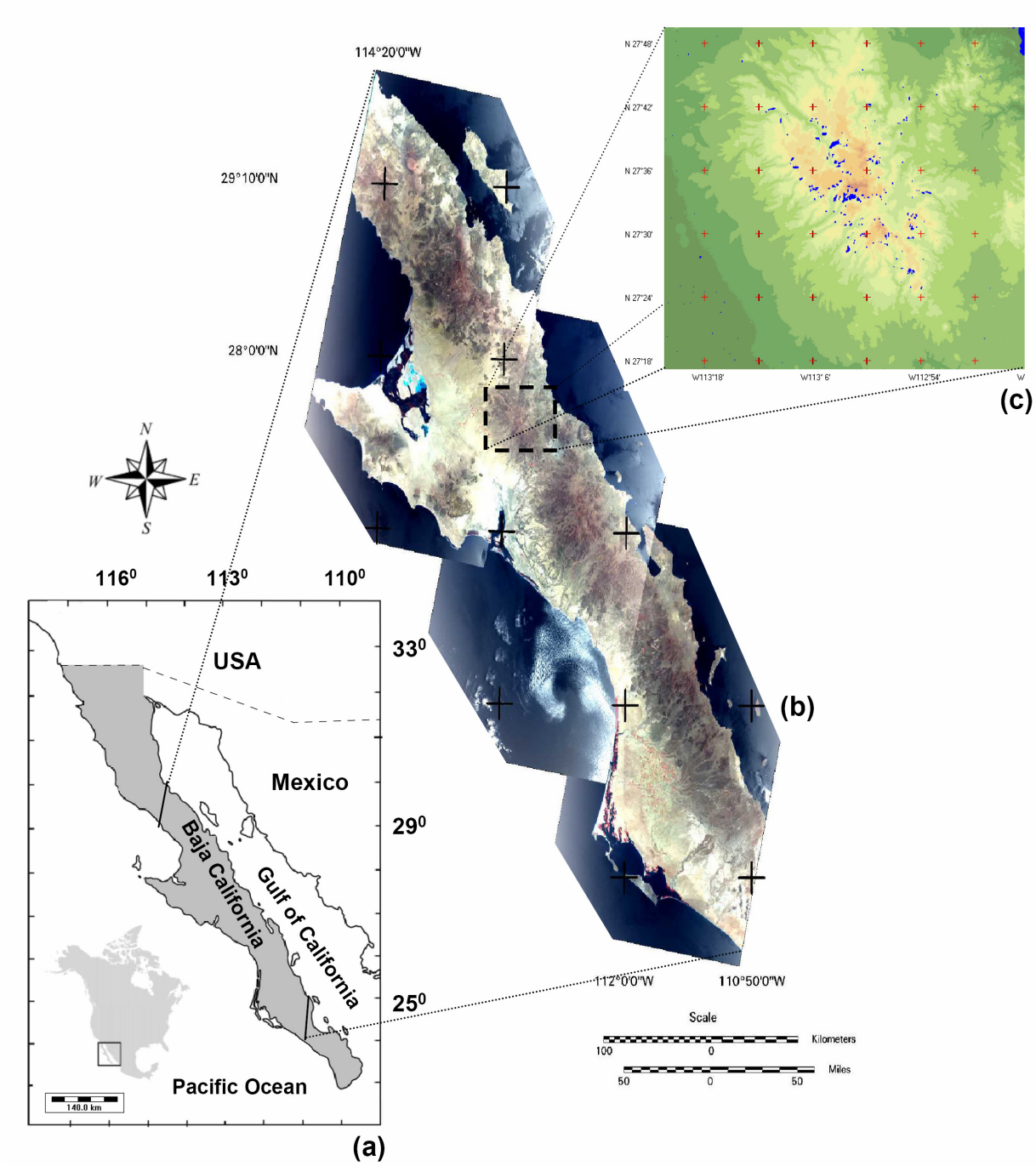

Figure 2.2. (a) Location map of Baja California. (b) Mosaic of ETM+ images. (c) SRTM digital elevation model of the selected test area. Blue patches are data gaps in the SRTM DEM.

(Figure 2.2b), which is representative of much of Baja California. In this paper, however, we focus on a selected test area (Figure 2.2c) in order to illustrate the veracity and utility of our proposed techniques.

II.3.2. Variography

Before using any geostatistical methods of estimation, the strength of spatial correlation similarities and dissimilarities between samples must be inferred. Variograms are basic diagnostic tools for graphically representing geostatistical relationships that describe and quantify the spatial variation of regionalized variables (Olea, 1994; Deutsch, 2002). A variogram can be described as a measure of dissimilarity or increasing variance as a function of distance between pairs of measured pixel values. Variography usually includes two main steps (Chambers and Yarus, 2001). First, an experimental variogram is computed that accounts for anisotropy and azimuthal directions. Second, the experimental variograms are modeled with continuous functions.

Pixel values in a DEM or remotely sensed image, whether elevation or digital number (DN), are considered geostatistically as regionalized variables, which then can be characterized by both random and spatial correlation aspects. Thus, these values can be studied simultaneously through the variogram function concept. A variogram function $\gamma(\mathbf{h})$ is a statistically robust spatial-estimator tool. A variogram function characterizes the spatial correlation between paired samples by computing the squared differences between their values. A variogram function can be expressed as follows:

$$\gamma(\mathbf{h}) = \frac{1}{2N(\mathbf{h})} \sum_{i=1}^{N(h)} [z(x_i) - z(x_{i+\mathbf{h}})]^2 \qquad (1)$$

where $\gamma(\mathbf{h})$ is the estimation variogram value for lag vector (h) between pixel z (x_i) and pixel z (x_{i+h}), and $N(\mathbf{h})$ is the number of pairs of pixels separated by **h**.

The ideal experimental variogram model consists of: (1) The range (A_o), which is the distance where the variogram reaches zero spatial correlation. The range of the variogram is controlled by the sill, where the spatial correlation between the data points after the range is almost zero. (2) The sill, which is the semivariance ($C_o + C$) where the variogram reaches its range. (3) A nugget (C_o) may be present, which is usually related to the presence of random noise, short scale variability, or measurement errors (Chambers and Yarus, 2001).

Variogram models must honor the condition of positive definiteness (Deutsch, 2002), which ensures a unique solution for the kriging equations and that the variance of any linear combination of data values will be positive (Kupfersberger and Deutsch, 1999). Spherical, exponential, and Gaussian models (Isaaks and Srivastava, 1989; Deutch and Journal, 1992; Goovaerts, 1997) are the most commonly used models that honor the condition of positive definiteness.

· The spherical model is defined by:

$$\gamma(\mathbf{h}) = c[1.5(h/a) - 0.5(h/a)^3],\ h \leq a \qquad (2)$$

$$\gamma(\mathbf{h}) = c,\ h > a$$

· The Gaussian model is defined by:

$$\gamma(\mathbf{h}) = c[1 - \exp(-h^2/a^2)] \qquad (3)$$

· The exponential model is defined by:

$$\gamma(\mathbf{h}) = c[1 - \exp(-h/a)] \qquad (4)$$

Where, h is the offset, a is the range, and c is the sill of the model.

Depending on the spatial behavior of the specific variable, the variogram can reveal several spatial characteristics such as continuity, anisotropy, zone of influence, zonality, and trend (Sahin *et al.*, 1998).

II.3.3. Ordinary kriging

Kriging was introduced by Krige (1951, 1966) and has become an important geostatistical estimation procedure. Kriging is recommended over conventional estimation methods because its estimates are unbiased, have minimal variance, can provide larger or smaller estimates than any of the sample values, take advantage of both distance and geometry to weight samples, and minimize the difference between the estimated and true values through a conceptual probabilistic random function model of the true values (Issak and Srivastava, 1989; Oliver *et al.*, 1989a, 1989b; Rossi *et al.*, 1994).

Ordinary kriging was used in this study and is the method typically used in the univariate case. Ordinary kriging is relatively simple and robust, especially when the kriging neighborhood is kept small (Arik, 2002). The detailed theory and equations that described ordinary kriging can be found in Journel and Huijbregts (1978), Issak and Srivastava (1989), and Wackernagel (2003). The advantage of using ordinary kriging is that it honors the data values at their locations, which is known as the exactitude property. The general equation for ordinary kriging is:

$$\sum_{i=1}^{N} \lambda_i \sigma_{ie}^{2} - \mu = \sigma_{oe}^{2} \qquad (5)$$

$$\sigma_{ie}^{2} = \mathrm{cov}\left(z_i, z_e\right) \quad , \quad \sigma_{oe}^{2} = \mathrm{cov}\left(z, z_e\right)$$

where N is the number of the primary variable, λ_i is the weight of the primary variable, σ_{ie}^{2} is the covariance between the known data points, σ_{oe}^{2} is the covariance between the known and unknown data points, and μ is the Lagrange Multiplier. Variance, in turn, can be calculated as

$$\sigma_{e}^{2} = \sigma_{o}^{2} - \sum_{i=1}^{N} \lambda_i \sigma_{oe}^{2} + \mu \qquad (6)$$

II.3.4. Cokriging

Cokriging is commonly used in the multivariate case. It is an interpolation technique that allows better estimation of the hard (or primary) variables using the soft (or secondary) variables, which are more intensely sampled and have a degree of correlation with the primary variables. According to Isaaks and Srivastava (1989), the spatial cross-correlation between the sparse primary variable and a spatially denser secondary variable is the key to improve the reliability of estimation. Thus, cokriging seems to be ideally suited for remote sensing problems yet, it has been used only rarely (Bhatti *et al.*, 1991; Atkinson *et al.*, 1994). We show here how cokriging can be used for generating corrected (gap-free) SRTM DEMs from ETM+ reflectivity data.

Topographic effects on radiance in optical satellite images have long been recognized (Stohr and West, 1975; Holben and Justice, 1980; Leprieur *et al.*, 1988;

Thomson and Jones, 1990). The proportion of light reflected toward a satellite also varies with the geometric relationships between the sun, target and viewer, all of which, in turn, vary with topography (Teillet *et al.*, 1982; Hugli and Frei, 1983). Topography also directly affects the spectral characteristics of reflected radiation (Dymond and Shepherd, 1999). The digital number (DN) is used here as a secondary variable that describes topographic effects on reflectance.

The new processing sequence introduced here is the reverse of the normal sequence, where a DEM is typically used to correct topographic effects on reflectivity in mountainous areas. The ETM+ has eight spectral bands, which are used to account for spectral variations related to topographic changes. The estimator in cokriging is given as:

$$z^* = \sum_{i=1}^{N} \lambda_i z_e + \sum_{j=1}^{M} \gamma_j y_r \qquad (7)$$

where z_e is the primary variable (elevation), λ_i is the secondary variable (reflectance), N and M are the number of primary and secondary variables, γ_j and y_r, respectively, are the weights of both primary and secondary variables. In cokriging, the cross-variogram between the primary and the secondary variables is critical for coregionalizing the two variables. Strict limitations are required to ensure a positive estimation variance on the coregionalization model (Isaaks and Srivastava, 1989). A positive definite variogram is a legitimate measure of distance. It then becomes necessary to determine only one value for the secondary variable that incorporates all the variability within the different spectral bands. To solve this problem, we used the alternating conditional expectations (ACE) algorithm to aid in appropriate transformations of the eight bands in order to end

with one variable, as will be explained later. ACE is a nonparametric method developed by Breiman and Friedman (1985) for finding optimal transforms. The source code can be found at http://playfair.stanford.edu, and the code used here was written by Xue *et al.* (1996). The advantage of this algorithm is that no assumption is made about the functional form of the regression (i.e., the regression is nonparametric). Breiman and Friedman (1985) only assumed that the optimal transform of the dependent variable is the sum of the optimal transforms of the independent variables.

The simplified ACE equation is:

$$\theta(\mathrm{z}) = \sum_{i=1}^{p} \phi_i(x) \qquad (8)$$

Where θ and ϕ are the transform functions and p is the number of independent variables, which in this case, are the eight thematic mapper spectral bands. *Z* and *X* are vectors of the data, and both may have random error. The ACE algorithm will find optimal values for θ and ϕ, from which a smoothed *Z* can be calculated from *X* (Zwahlen *et al.*, 1997). The improvement in the estimated results using cokriging is highly dependent on the degree of correlation between the primary and the secondary variables. To improve the correlation, the primary variable is transformed using the normal score transform algorithm (NST).

The cokriging variance can be calculated as:

$$\sigma_{c_e}^2(x) = \sigma_e^2 - \sum_{i=1}^{M} \lambda_i C_e(x, x_i) - \sum_{j=1}^{M} \gamma_j C_{er}(x, x_j) + \mu_1 \qquad (9)$$

where Ce is the covariance of NST elevation, Cr is the covariance of ACE reflectance, and Cer is the cross-variance between e and r.

II.4. Application and results

II.4.1. Data description

The geostatistical methods described above were applied to the SRTM data, which are sampled at intervals of three arc-seconds. The SRTM-3 arc-second data are generated using three-by-three averaging of the one arc-second samples. SRTM data cover Earth between 60^{o}N and 57^{o}S. The DEM is constructed using synthetic aperture radar (SAR) interferometry using phase differences between images. Using the regular processing steps to generate the DEMs does not account for scattered shadows in mountainous areas. Large holes in the land area may remain unfilled and presumably reflect areas where there have been problems with data processing.

Six Landsat ETM+ level 1G images covering almost 75% of Baja California are used in the present study. Landsat ETM+ images have a stable radiometric response with low noise because the radiometric response of each ETM+ detector was calibrated pre-launch as a function of incident spectral radiance (Williams, 2002). Because of their stable radiometric response and high signal-to-noise ratio, ETM+ images are most appropriate in terms of reflectivity for the technique described here.

II.4.2. Ordinary kriging results

Isotropic behavior is very rare in natural geologic settings, thus it is important to investigate directional variograms derived from raw, untransformed satellite data of Earth's land surface. Figure 2.3 illustrates the directional experimental variogram in the four major geographic directions, 0^0, 45^0, 90^0, and 135^0 respectively. Using the parsimony principle, a Gaussian model is used to fit the first two directions, whereas a spherical model is more reasonable for fitting the other directions. The selected window test area (Figure 2.4a), shows no trend in the variogram behavior, although this is not always typical. In other words, the variogram properties are completely controlled by the topography surrounding any gaps within the working window. In remote sensing, we usually deal with millions of pixels, so searching all data to select a kriging neighborhood is computationally prohibitive (Rossi *et al.*, 1994). Thus, a spiral searching algorithm is introduced to select only the closest data to the estimation points (Deutsch and Journel, 1992).

In the technique described here, the working windows are selected visually, where two main constraints are followed. First, the window should be as small as possible, and second, data gaps should be surrounded by sufficient neighboring samples in all directions in order to avoid trend modeling. Modeling data trends is only important if estimates are located at the boundary of a cell (Bailey and Gatrell, 1995). A surface variogram (Figure 2.4b) is used to estimate both major and minor ranges and to prove the anisotropic character of the selected window. The ellipse fitting method applied to

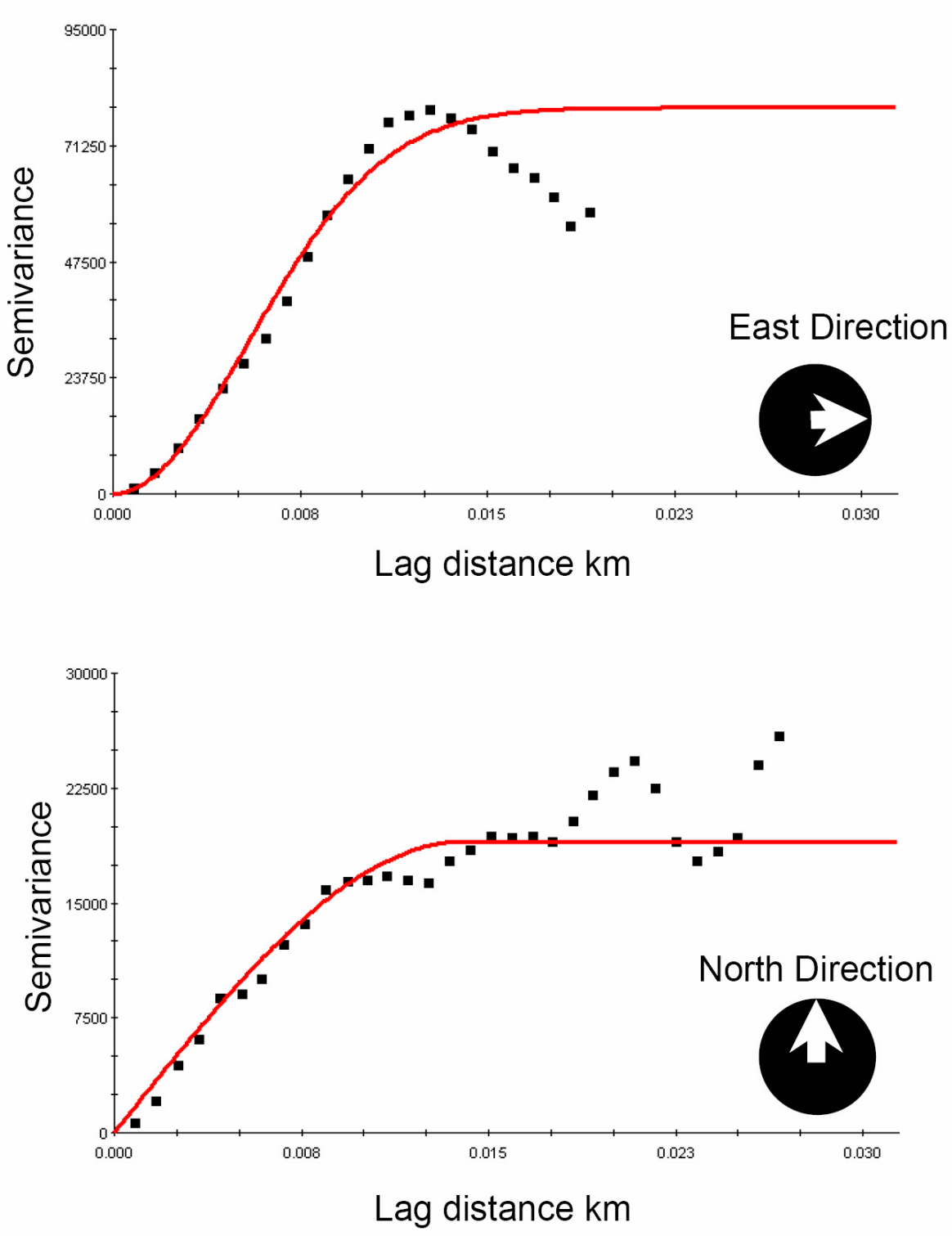

Figure 2.3. Plot of experimental variograms and fitted models in different directions.

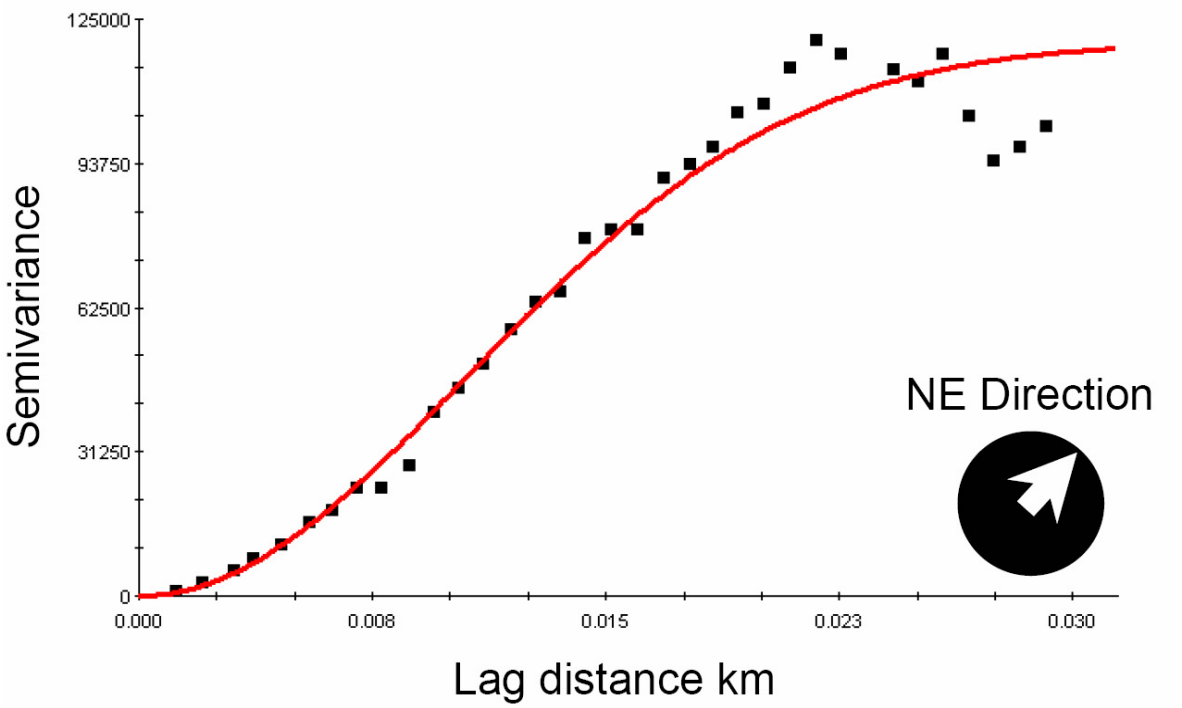

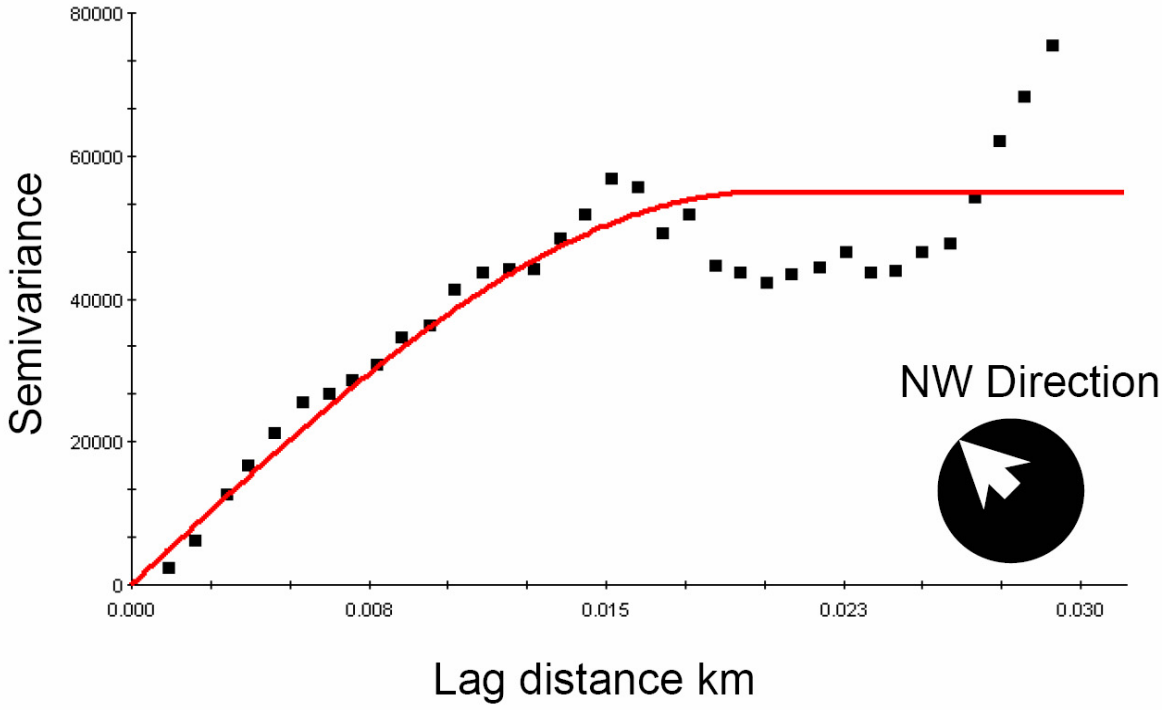

Figure 2.3. (Continued)

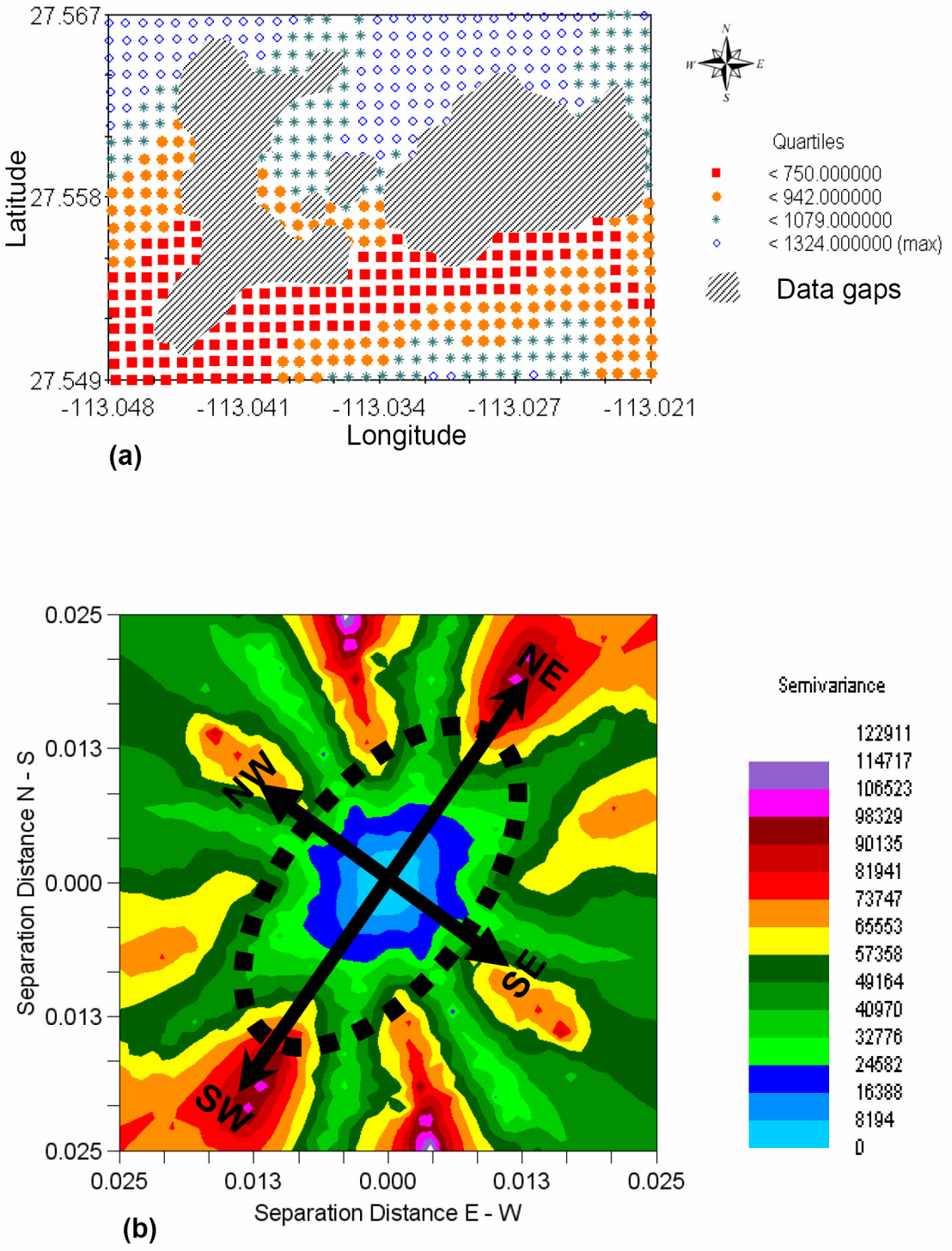

Figure 2.4. (a) Selected window from the test area showing data gaps. (b) Plot of surface variogram showing the elliptical fitting model.

the model ranges reveals the major anisotropy in the NW-SE direction and minor anisotropy in the NE-SW direction.

Figure 2.5a shows the ordinary kriging results for the test area. The interpolation of the data gaps looks geologically acceptable. The smoothing effect, which is a major drawback of ordinary kriging and most other interpolation methods, is dominant and obscures much of the surficial features that might exist. Quantitative evaluation of the results is crucial, where ordinary kriging variance is commonly used as an analog for the uncertainty measurements associated with the ordinary kriging estimates. An Iso-surface contour plot of the estimation variance shows a realistic zonal increase in the estimation variance from the boundary of the data gap toward its middle (Figure 2.5b), which reflects the increase of the uncertainty measurements toward the center of the data gap. It also is worth noting that there are important implications for using the variance as a proxy for the uncertainty. Journel (1993) and Armstrong (1994) referred to the variance as a measure of reliability rather than as a measure of the uncertainty of the ordinary kriging estimate. By using variance in this way, the variance of the errors becomes independent of the actual data values and depends only on the data configuration. This situation is referred to as “homoscedasticity”, which is rarely achieved in practice (Goovaerts, 1997).

A more convenient tool that usually provides a more robust quantification of estimated values for data gaps is cross-validation. Cross-validation basically answers four main questions: (1) Is the variogram model appropriate? (2) Is the search neighborhood appropriately scaled? (3) Are data for any regions underestimated? (4) Are

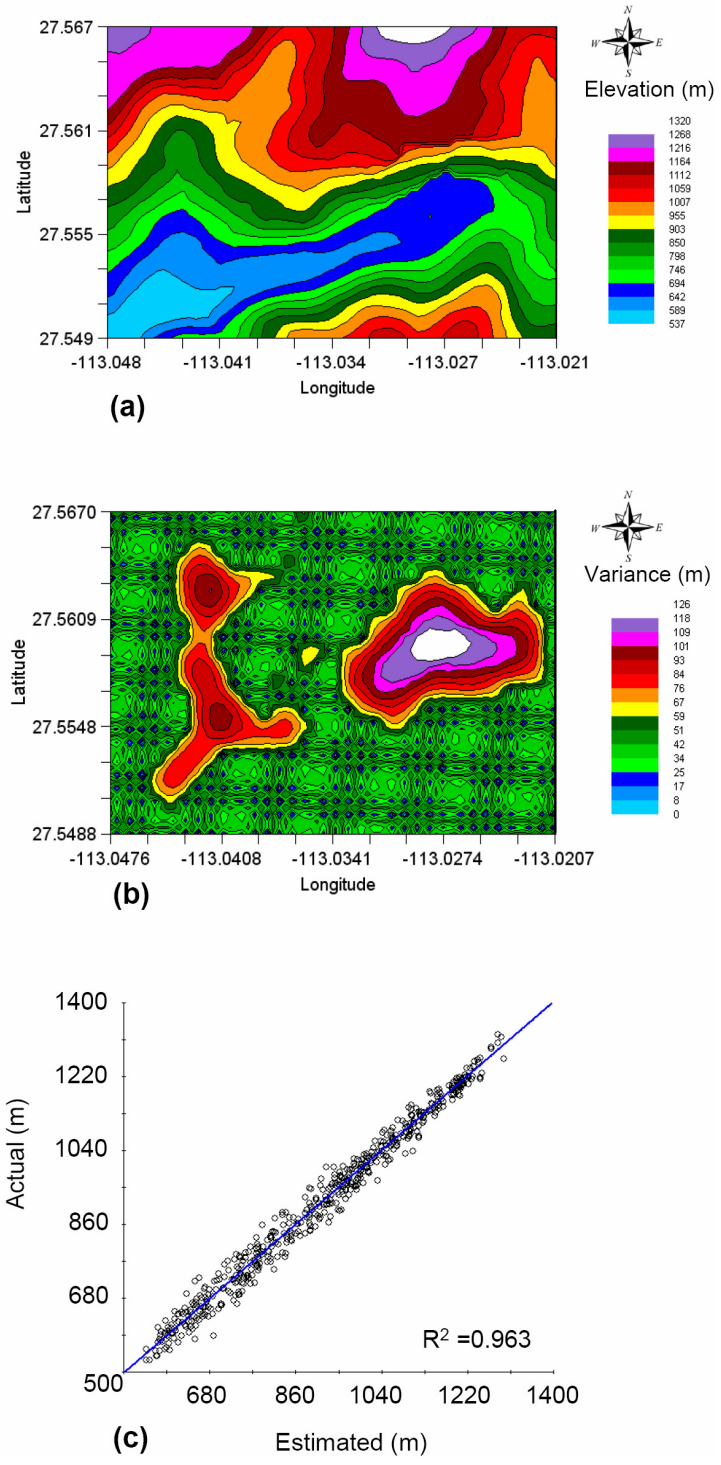

Figure 2.5. (a) Contour map of elevation generated using the ordinary kriging method. (b) Ordinary kriging uncertainty map. (c) Cross-validation of ordinary kriging interpolation.

prediction errors comparable? The "leave-one-out" (or LOO) strategy (Allen, 1974) is the basis for cross-validation, where the value of a known sample is estimated with the help of all other data. This procedure is then repeated for each sample within the data set. Cross-validation results for ordinary kriging are usually expressed as a regression plot between the actual data and the estimations of these actual data (Figure 2.5c).The scattered points around the 45^o line along with the value of the R^2 are key for evaluating the ordinary kriging accuracy. As indicated in the figure, the plotted points are closely scattered around the 45^o line, where no over- or underestimation is observed. At the same time, the value of R^2 (0.963) reflects the high degree of correlation between the actual and estimated data points. Generally speaking, the ordinary kriging method is an unbiased interpolation that provides a valid least-squares estimate of the data gaps. In the absence of reflectance data, ordinary kriging can stand alone as a valid technique to provide acceptable values for the data gaps in the SRTM DEM.

II.4.3. Cokriging results

In order to improve the reliability of the estimated values, the primary variable is transformed to be normally distributed, which then establishes homogeneity within the variance. A normal distribution is usually desired for processing the data statistically. A normal distribution allows the data to be defined by only two parameters: the mean and the standard deviation. Normally distributed data also improve the variogram analysis and kriging results. It is typically unnecessary to transform the data, although some specific analysis, such as Gaussian simulation, may be necessary. The normal score

transform (NST) algorithm was used in this study to transform the data into normal distribution and to normalize the data, such that the mean has zero value and standard deviation equals unity (Figure 2.6). NST is a random non-parametric transformation, that is, the transformation function changes with each data set and the algorithm can partially remove any systematic component within the data. In other words, the NST algorithm suppresses the presence of any underlying or hidden trends. We then assumed isotropic conditions (i.e., no trend), which most gridding algorithms make before running.

The ACE algorithm is used where elevation, the primary variable, is assigned as the dependent variable and the eight ETM+ spectral bands are assigned as the independent variables. Given dependent random variables Y (i.e., elevation) and independent random variables X1 through X8 (i.e., the eight thematic bands), we define the arbitrary mean zero transformation e(Y) and b1(X1), b2(X2),…, b8(X8). The optimal transformation of each variable is then calculated to maximize the correlation (details in Breiman and Friedman, 1985). Thus,

$$e^*(Y) \quad vs. \quad b1^*(X1) + b2^*(X2) + \ldots\ldots\ldots + b8^*(X8) \tag{10}$$

Figure 2.7 shows the optimal transformation of each thematic band and the power function used to fit each transformed band. Figure 2.8a shows elevation versus the sum of the transformed spectral band independent variables. A linear regression in transformed space results in the optimal transformation function (OTF):

$$e^*(Y) = -3.1341E+01 \times (sum\, b_i^*(X_i))^2 + 2.0504E+02 \times (sum\, b_i^*(X_i)) + 9.4787E+02 \quad \ldots\ldots(11)$$

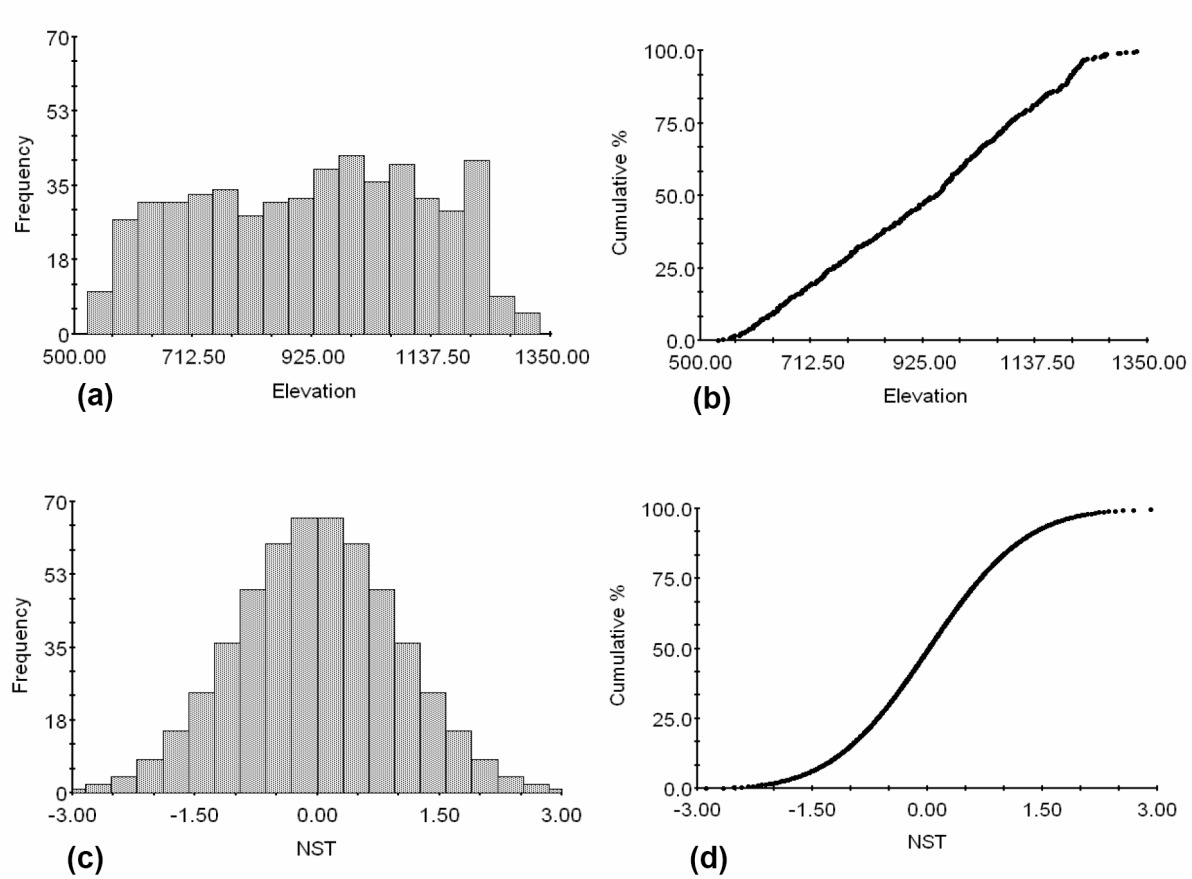

Figure 2.6. Normal score transform results. (a) The untransformed elevation histogram. (b) The untransformed elevation cumulative frequency. (c) NST histogram of elevation. (d) Cumulative frequency curve of elevation.

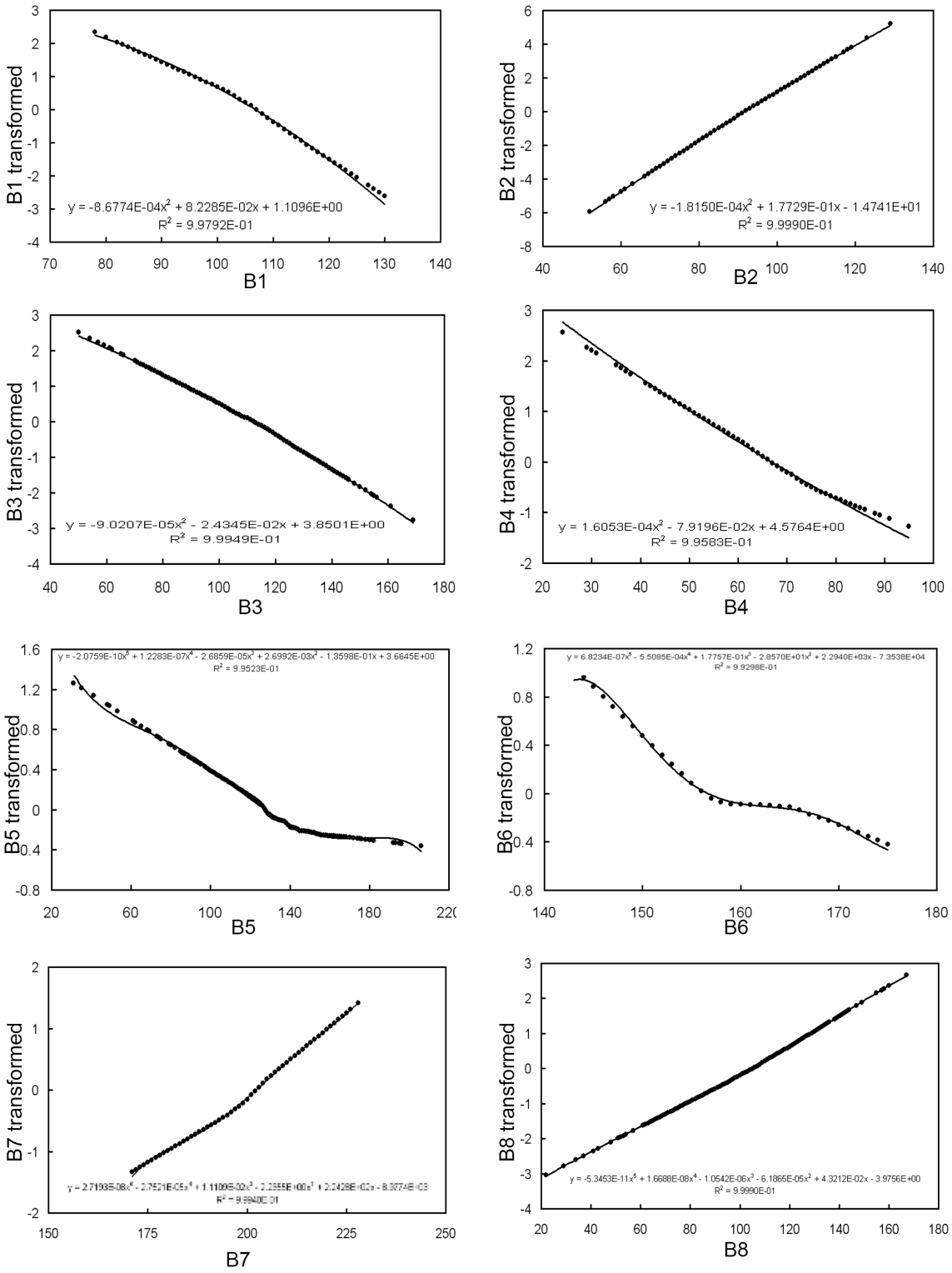

Figure 2.7. Optimal transformation of the eight ETM+ bands.

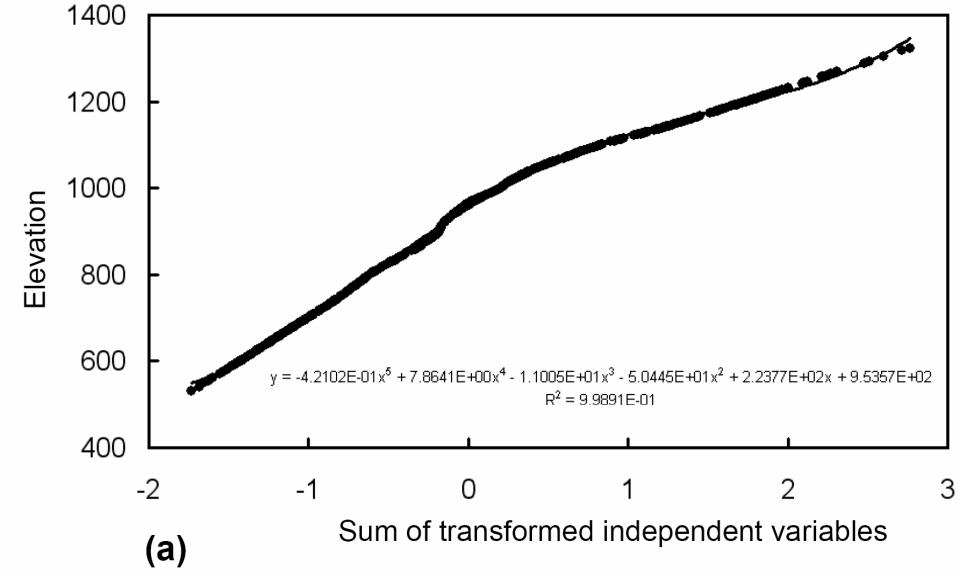

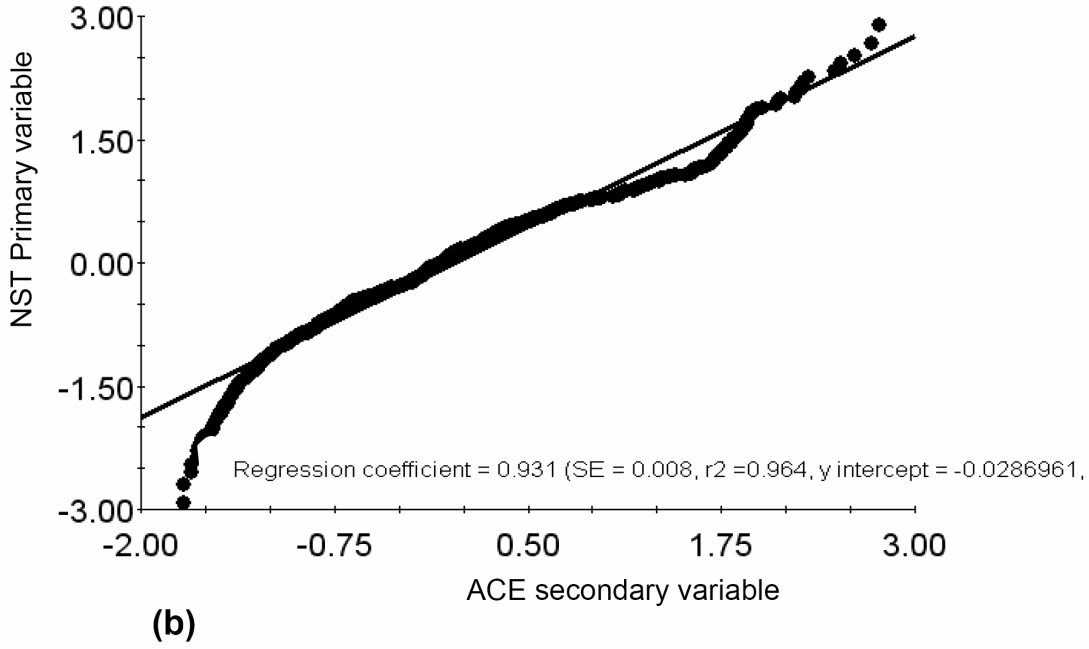

Figure 2.8. (a) Linear regression between the elevation and the sum of the transformed independent variables. (b) Linear regression between the NST primary variable and the ACE secondary variable (covariate).

The ACE secondary variable is defined by one value which represents the sum of OTF of the eight thematic bands. The linear regression between the NST primary variable versus the ACE secondary variable is shown in Figure 8B. Both algorithms, NST and ACE, dramatically increase the degree of correlation between the hard and soft variables.

As discussed earlier, the primary variogram, the secondary variogram, and the cross-variogram are constructed before running the cokriging algorithm. Figure 2.9 illustrates the surface plots of the three variograms, which reveal the isotropic behavior of the data.

In practice, we assume a weak second-order stationary random function. We started with modeling the cross-variogram using transition models that honor the rule of parsimony (i.e., minimum number of models). The spherical model is used where it fits to the data points well (Figure 2.10a). This model exhibits linear behavior at the origin and reaches the sill at distance a , if the proposed variogram equations are:

$$\gamma_e(h) = C_{oe} + C_{1e}\, sph_{a1}(h) \quad (12)$$

$$\gamma_r(h) = C_{or} + C_{1r}\, sph_{a1}(h) \quad (13)$$

$$\gamma_{er}(h) = C_{oer} + C_{1er}\, sph_{a1}(h) \quad (14)$$

The cross-variogram model should also satisfy the third requirement, which is:

$$C_{oer}^{\ 2} \le C_{oe}\, C_{or} \quad (15)$$

$$C_{1er}^{\ 2} \le C_{1e}\, C_{1r} \quad (16)$$

where a and C are the range and sill values, respectively.

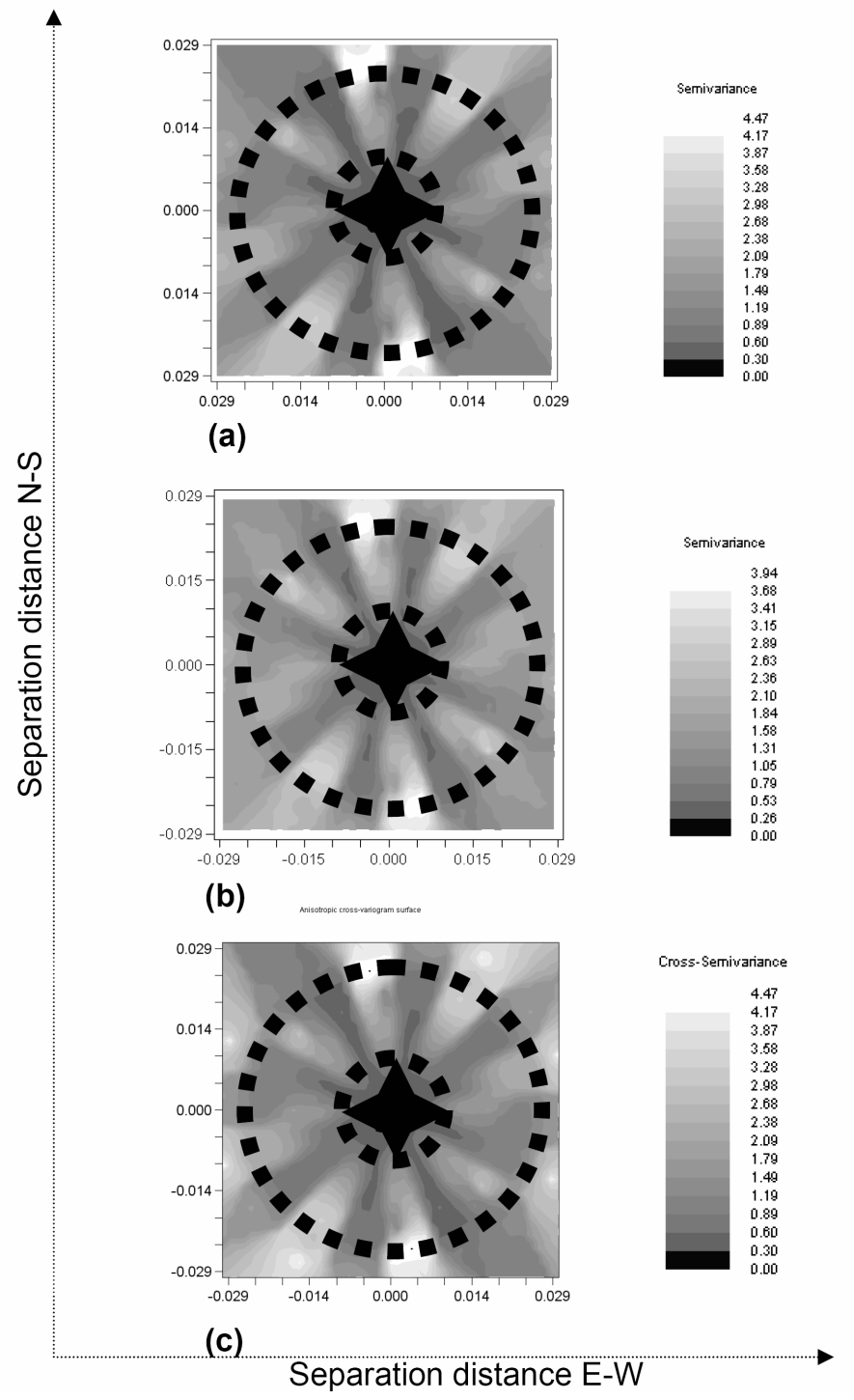

Figure 2.9. Surface variogram plots. (a) Cross-variogram. (b) Primary variogram. (c) Secondary variogram. The three plots reveal the isotropic character of the data.

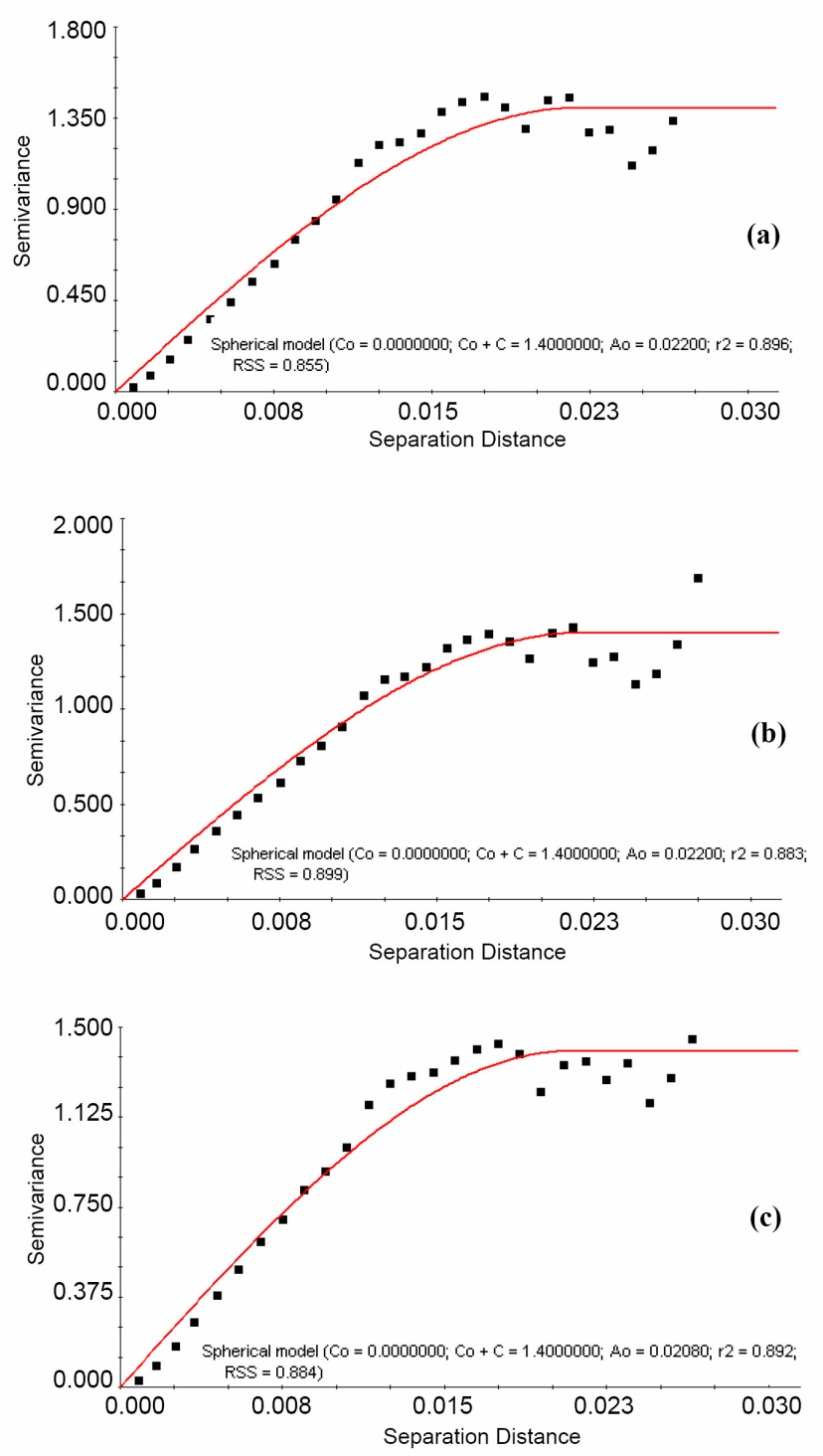

Figure 2.10. Omni-direction variograms, fitted with the spherical model. (a) Cross-variogram. (b) Primary variogram. (c) Secondary variogram.

The regression coefficient (R^2) and residual sums of Squares (RSS) were used to evaluate the fitting of the modeled experimental variogram. R^2 provides an indication of how well the model fits the variogram data. RSS is more sensitive than R^2, and is typically used to ensure and to provide a measure of the best-fit of the variogram model. A low RSS value usually indicates a better model fit. As illustrated in Figures 2.10b and 2.10c, the spherical model is used also to fit the primary and secondary variograms to satisfy the first constraint. The cokriging map of the NST elevation (Figure 2.11a) and the iso-surface contour plot of the estimation variance (Figure 2.11b) show the robustness of the proposed technique. The cokriging map is geologically more realistic and the estimation variances decreased, which reflect an increase in the certainty of the estimates. The cross-validation further supports the improvement, where the R^2 increased from 0.96 using ordinary kriging to 0.99 using cokriging (Figure 2.11c).

The cokriged NST variable must then be back-transformed to yield a corrected DEM. A linear regression between the elevation and its NST is fitted using a fifth-order polynomial equation, which is used to perform the back-transformation. The final results should be tested by measuring the RMSE, which is defined as:

$$RMSE = \sqrt{\frac{\sum (e - w)^2}{n}} \qquad (17)$$

where e is the elevation extracted from the corrected DEM, w is the elevation measured in the field, (which has a higher precision), and n is the number of tested field locations or ground control points. Since our field data did not coincide with the actual data gaps, we generated artificial gaps in the STRM DEM that coincided with our ground control

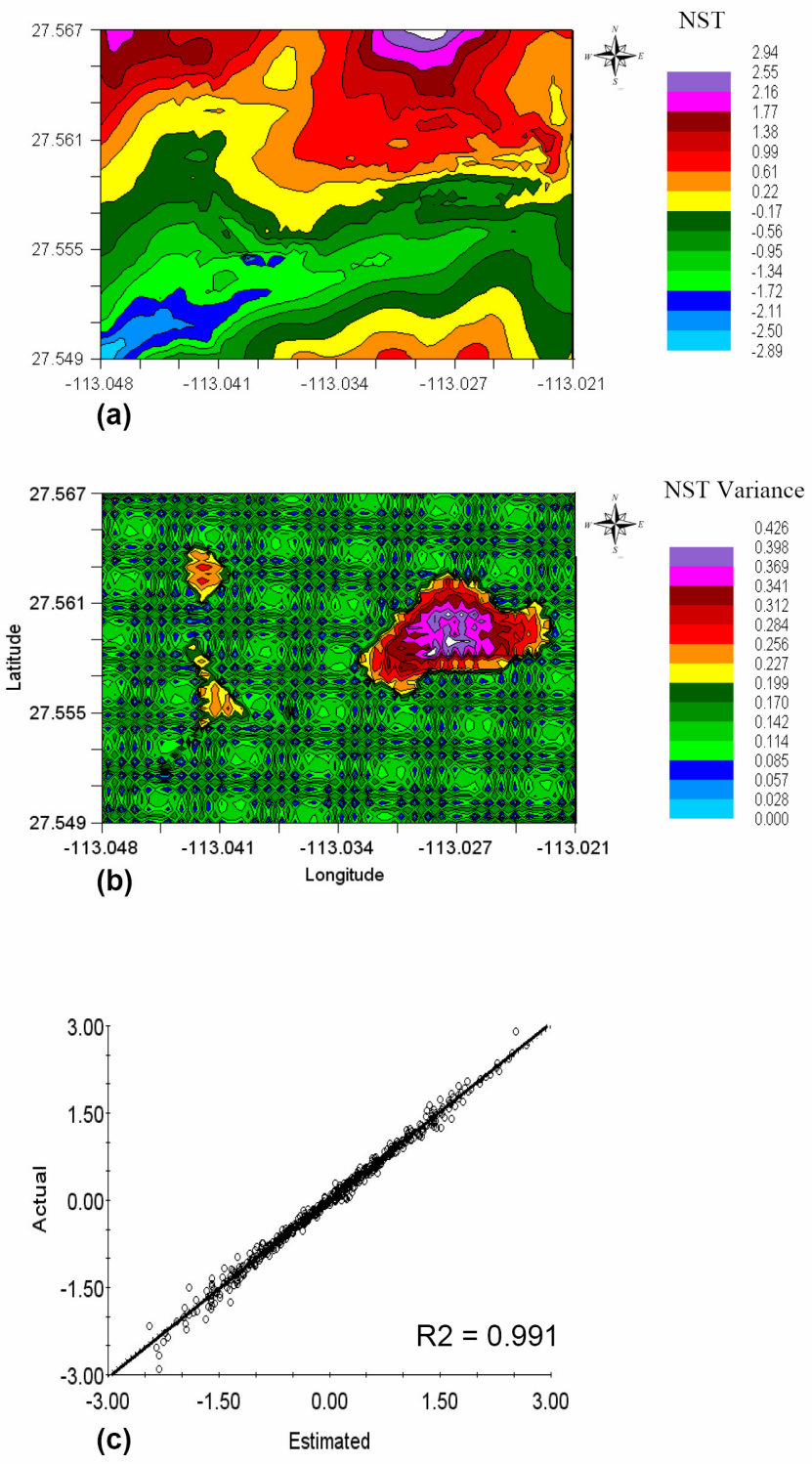

Figure 2.11. (a) Cokriging of the NST contour map. (b) Cokriging uncertainty map. (c) Cross-validation of the cokriging interpolation.

points, where elevation was measured in the field using hand-held GPS units. We then applied cokriging to refill these artificial gaps. Table 2.1 shows the RMSE for the locations that were refilled using cokriging, where the incorporation of the reflectance variable as a soft background improves the estimation and decreases the RMSE.

The cokriging procedures were applied to the entire study area, producing a well-corrected and enhanced DEM with 90-m resolution. Resampling of the corrected DEM using cubic convolution techniques increased the resolution to 30 meters (Figure 2.12). The cubic convolution method calculates an output cell value from a 4 X 4 block of surrounding input cells (details of this method are in the ERDAS Field Guide, 2003). The output value is a distance-weighted average, but the weight values vary nonlinearly as a function of distance. The cubic convolution produces sharper images than both bilinear and nearest neighbor interpolation, although it is the most computationally intensive resampling method. The cubic convolution method is preferred when resampling to a larger output cell size.

To further assess the efficiency of our proposed technique, we introduce the following example as a practical application. One of the important functions of Terra Satellite (Yamaguchi *et al.*, 1998) is to derive DEMs from Advanced Spaceborne Thermal Emission and Reflection Radiometer (ASTER) stereo images. Cloud cover and shadows from clouds create gaps in ASTER images. Automated stereo-correlation techniques (Ackermann, 1984; Ehlers and Welch, 1987; Lang and Welch, 1999) can be used on ASTER data to generate relative DEM, where the elevations are not tied to a ground or map datum and converting the relative DEM into an absolute DEM is

Table 2.1. RMSE for the Final CoK Map Calculated Using 24 GCPs.

NO.	Geographic position (lat/long)	DEM elevation (e) (m)	Field elevation (w) (m)	$(e-w)^2$	$RMSE = \sqrt{\frac{\sum (e-w)^2}{n}}$
1	N 27^0 22` 46.5``	371	360.7	106.09	
2	W 112^0 26` 10.0`` N $27^0$ 23` 06.0``	321	327	36	**7.2234 m**
3	W 112^0 23` 00.4`` N $27^0$ 16` 31.8``	67	73.4	40.96	
4	W 112^0 14` 38.3`` N $26^0$ 27` 20.1``	130	121	81	
5	W 111^0 38` 50.3`` N $26^0$ 53` 19.8``	9	10	1	
6	W 111^0 59` 11.8`` N $27^0$ 18` 05.4``	133	129.8	10.24	
7	W 112^0 53` 33.8`` N $27^0$ 38` 47.1``	82	88.4	40.96	
8	W 113^0 23` 01.8`` N $27^0$ 58` 02.3``	4	7.8	14.44	
9	W 114^0 00` 58.4`` N $28^0$ 55` 42.5``	207	211.5	20.25	
10	W114^0 09` 22.9`` N $29^0$ 43` 44.0``	553	557.4	19.36	
11	W 114^0 43` 03.9`` N $29^0$ 02` 42.6``	331	334	1.69	
12	W 114^0 09` 02.9`` N $28^0$ 59` 35.9``	256	257.3	9	
13	W 113^0 45` 55.2`` N $28^0$ 43` 39.5``	116	118	4	
14	W 114^0 06` 18.1`` N $27^0$ 44` 57.6``	4	3.7	0.09	
15	W 114^0 00` 40.3`` N $26^0$ 12` 27.3``	29	26	9	
16	W 111^0 26` 37.3`` N $26^0$ 00` 38.3``	16	17.2	1.44	
17	W 111^0 21` 35.9`` N $25^0$ 36` 30.5``	361	360.1	0.81	
18	W 111^0 18` 53.0`` N $25^0$ 24` 23.5``	141	142.3	1.69	
19	W 111^0 32` 34.4`` N $25^0$ 19` 54.0``	61	59.4	2.56	
20	W 111^0 38` 06.1`` N $25^0$ 15` 17.0``	37	35	4	
21	W 111^0 46` 31.7`` N $25^0$ 02` 19.5``	52	47	25	
22	W 111^0 40` 32.8`` N $24^0$ 03` 16.0``	255	283.3	800.86	
23	W 110^0 35` 04.2`` N 24^0 07 09.1	20	27	49	
24	W 110^0 26` 11.9`` N $24^0$ 54`43.9`` W 111^0 59` 31.5``	3	-2	25	

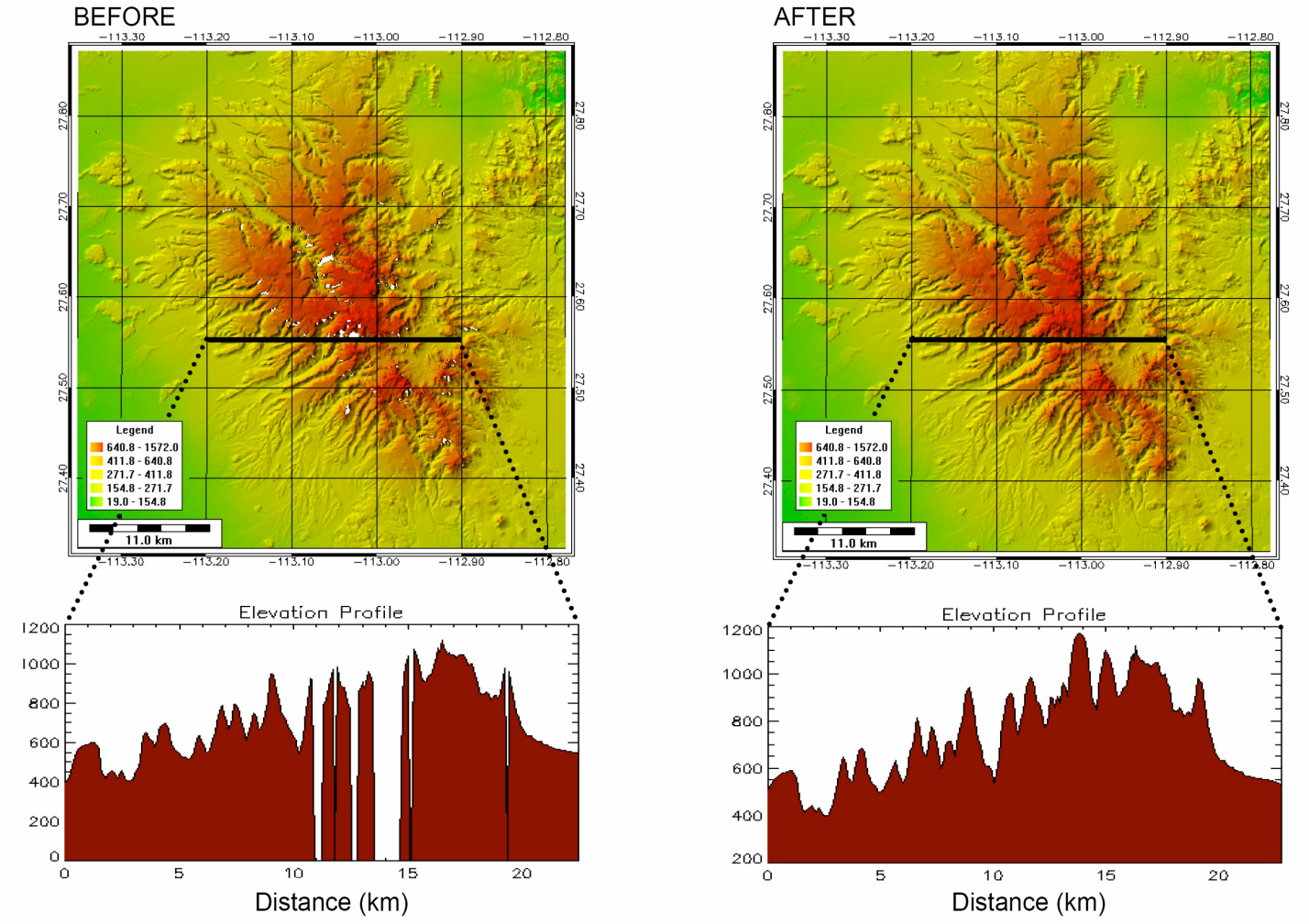

Figure 2.12. DEM and selected topographic profile across study area, before and after corrections and resampling.

controlled by the presence of scattered ground control points. These ground control points are usually collected in the field or sampled from available topographic maps, where error is introduced in both horizontal and vertical coordinates. In addition, the developed ASTER DEMs will still have the same problems with artifacts and data gaps. Thus, instead of using scattered ground control points and to avoid the bias that might be introduced, we used the corrected SRTM DEM. Running the automated stereocorrelation algorithm with the corrected (gap-free) SRTM DEM in the background guided the correlation process and resulted in an accurate, registered, and scaled ASTER DEM without any artifacts (Figure 2.13).

II.5. Summary and outlook

Our results indicate that both ordinary kriging and cokriging are valuable techniques for estimating elevation values for areas of missing data in SRTM DEMs. In this study, accounting for trends was not justified because the shapes of the variograms indicate the absence of any trends in the selected test area. This may not be typical for all data sets, however, so trend investigation should be performed in many cases.

The smoothing effect of any interpolation method is a drawback, but the proposed cokriging method provides significant improvement over the ordinary kriging results. The cokriging method also honors the geological variations in topography and geomorphologic features. The Digital Number (DN) can be used as a proxy for the reflectance to account for the topographic variations within the data gaps. The DN is used because most of the algorithms used for converting reflectance values incorporate

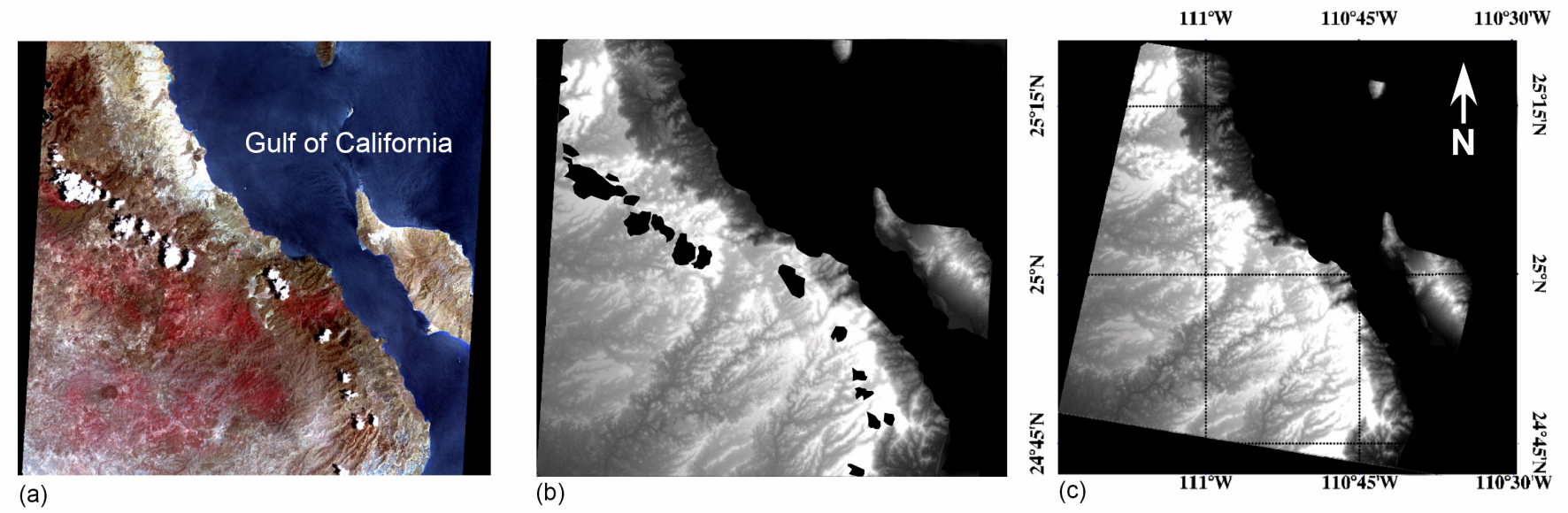

Figure 2.13. (a). ASTER image located in the extreme southern part of the study area. White and black patches are clouds and their shadows. (b) Relative ASTER DEM generated using automated stereocorrelation algorithm. Notice the artifacts (data gaps) that match the cloud and shadow locations. (c) Rectified absolute gap-free ASTER DEM.

atmospheric corrections, which may deteriorate the reflectivity behavior as a direct response to topographic variations. The ACE algorithm was used to generate a single variable that incorporates all of the variability within the eight reflectance bands of the ETM+ data. The ACE algorithm not only provides the sum of the transformed independent variables but also increases the correlation between the soft and hard variables. Normal score transformation (NST) improves both the correlation and interpolation performance of the cokriging.

Mapping the variance is useful for illustrating the uncertainty within the estimated areas. On the other hand, cross-validation techniques provide a robust way to further evaluate the accuracy of the elevation estimates. Our results show an improvement in the elevation estimates using cokriging ($R^2 = 0.991$) rather than using ordinary kriging ($R^2 = 0.95$). This improvement is seen visually in the reduction of smoothing effects in the final cokriging map (Figure 2.11a).

Finally, the RMSE was calculated (Table 2.1) using twenty-four ground control points for validation of the estimated elevation values within data gaps that we artificially introduced into the SRTM DEM. The RMSE had an average value of 7.22-m at the corrected locations, which is a reflection of the robustness of our technique. Using the corrected SRTM DEM in the algorithm of automated stereo-correlation to generate ASTER DEM was very successful. Our proposed technique produces an artifact-free DEM that has 15-m spatial resolution, which is comparable to the USGS 1-arc second DEM (Figure 2.13).

II.6. Conclusions

In this paper, we describe a technique for resolving a problem that commonly arises when working with DEM, namely, how to fill various artifacts with elevation values that are statistically robust and geologically meaningful. The main conclusions from the new technique described here include:

- Ordinary kriging provides estimated elevations for data gaps, but the method fails to account for natural geological and topographical variations that are commonly obscured by smoothing.
- The ACE algorithm provides an optimal non-parametric transformation of the eight bands in ETM+ data, where the sum of the transformed bands is used as a secondary variable for cokriging.
- In our test area, cokriging provides a geologically realistic map with less smoothing effects, although the performance and effectiveness of this method is completely controlled by the degree of correlation between the secondary variables (i.e., the eight thematic mapper bands) and elevation.

Our proposed technique demonstrates that application of spatial geostatistical methods to remote sensing data is fertile ground for advanced approaches in geoscience mapping.

CHAPTER III

AUGMENTED-VECTOR METHOD AND OBJECT-ORIENTED CLASSIFICATION OF BAJA CALIFORNIA, MEXICO

The purpose of this part of the study is to generate accurate thematic geologic maps with high resolution (15-m) for the entire eastern coast of Baja California. The main approach that we used to clearly represent all the lithological units in the investigated area was object-oriented classification based on fuzzy logic theory. We used the supervised maximum likelihood algorithm to define the fuzzy logic membership functions and carried out the fuzzy logic classification procedures using eCognition software developed by Definiens. The area of study was divided into twenty-two blocks, each was classified independently on the basis of its own defined membership function. This division is valuable to decrease the computational time and to increase the overall accuracy of each block. Six raw scenes (level 0) of Landsat 7 ETM+ imagery and thirty-two advanced spaceborn thermal emission and reflectance radiometer (ASTER) images were used as the main optical input for classification, in addition to a 15-m resolution digital elevation model (DEM) and some ancillary scattered geologic maps. All images were rectified precisely until 0.2 RMS errors were achieved. The optical data were stacked with the terrain data and then normally score transformed to eliminate the different-scale issue. Two blocks, block 4 and block 8, were selected to illustrate the results of this semiautomated approach of classification. The results were evaluated by

three main methods: (1) Accuracy assessment by classification stability; (2) Accuracy assessment by best classification results; and (3) Accuracy assessment by error matrix based on test areas. The overall accuracies were 89.6 % and 82.5 % for Blocks 4 and 8 respectively, indicating that this approach was highly recommended over the most conventional classification techniques.

III.1. Introduction

Many attempts have been made to use the advantages of the high resolution satellite data that are available nowadays to generate a coherent spatial classification. Satellite imagery is considered the most accessible and accurate global resource because it provides wider variety and greater quantity of information than traditional mapping data; it is used to produce high quality lithological classification. No "standard" approach in extracting land cover information can be applied for all situations because the problem is affected by a number of complex, often interacting factors that pertain to energy source, sensor, atmospheric condition, energy/matter interactions at the earth's surface, data handling and processing systems, and data users (Lillesand and Kiefer, 1987).

Classification of satellite imagery is the process of clustering data into a number of uniquely identified classes that have similar spectral characteristics. Clustering is based on the degree of similarity and dissimilarity between the different groups, so data points that belong to the same group should be highly similar, but dissimilar from the other groups. Different results can be achieved for the same data set by implementing different classification algorithms (Benediktsson *et al.*, 1990a, b; Hepner *et al.*, 1990; Key *et al.*,

1989; Bischof *et al.*, 1992; Kanellopoulos *et al.*, 1992; Civco, 1993; Paola and Schowengerdt, 1994; Solaiman and Mouchot, 1994; Skidmore *et al.*, 1997). However, these results are often characterized by limited accuracy and low reliability (Haala and Brenner 1999). Development of an optimal classification algorithm is a challenging problem (Ho *et al.*, 1994) and no image classifier provides perfect results (Matsuyama, 1989). Thus, Kanellopoulos *et al.* (1993) and Brown *et al.* (2000) suggested that combining classifiers could be a useful and practical approach to increase classification accuracy and to optimize classification performance.

Input data sets typically play a critical role in guiding the selection of appropriate algorithm for the classification process. We chose an object-oriented classification technique to perform the classification tasks, where object-based techniques have been proven in terms of their potential to consider spatial complexity in the image classification process (Blaschke and Strobl 2001).

Although object-based analysis of multispectral imagery was introduced early in the remote sensing literature (Ketting and Landgrebe, 1976), it has been largely ignored in favors of pixel-based methods, which have always been selected for conducting classification tasks (Lobo, 1997). Several object-based image analysis techniques have been used successfully for forest information extraction purposes (Hay *et al.*, 1996; Pekkarinen, 2002; St-Onge and Cavayas, 1997). This technique has also been widely applied to urban applications (Damm *et al.* 2005; Grenzdörfer 2005, Argialas and Derzekos 2003), biotope classification (Leser 2002) and forest applications. For example, Mitri and Gitas (2002) developed an object-oriented classification model for

burned area mapping. Also, Flanders *et al.* (2003) tested the object-oriented approach for forest cut block delineation. Hese *et al.* (2005) used contextual information to classify forest cover change patterns and (Chubey *et al.*, 2006) analyzed object oriented procedures for forest inventory parameters from Ikonos data. More recently, Arroyo *et al.* (2005) examined object oriented methods for regional fuel mapping with Quickbird data.

The variability of the data on hand prompted the use of such methodology because more information could be extracted and precise results could be achieved from these data. On the other hand, many land cover classification studies have been done using multisource data such as optical data and ancillary data, e.g. digital images, terrain information like elevation, aspect, slope and thematic maps (Benediktsson *et al.*, 1990; Kanellopoulos and Wilkinson 1997, Mather *et al.*, 1998; Haack and Bechdol, 2000; Le Hegarat Mascle *et al.*, 2000), where tremendous improvement in classification accuracy was reported.

The concept behind object-oriented classification is that the classification will be based on the image objects and their mutual relationships rather than on a single pixel. This allows and facilitates the integration of a broad spectrum of different object features such as spectral values, shape, or texture for implementing classification. However, to deal with a multisource classification, we also used an augmented-vector method (also known as staked-vector methods). According to Tso and Mather (2001), there are three main issues involved with using this method. The first issue concerns possible differences in scales and measurements of each data set. To overcome this problem we

used a normal score transform (NST), which is a graphical transform that can normalize any distribution, regardless of its shape. We used the NST algorithm to transform the multisource data sets into normal distribution and to normalize each data set, such that the mean has zero value and standard deviation equals unity. The second issue is the computationally intensive nature of this method. Reducing the number of data vectors is the best way to reduce the computational coast of this technique. The third issue of this technique is data reliability or uncertainty, where the input vectors are treated equally in terms of contribution to the classification. To overcome this problem, we assigned the input vectors different weights in the object-oriented classification algorithm, depending upon the degree of correlation between these vectors and the separability analysis. Figure 3.1 shows a simplified flowchart which summarizes the main classification steps used in this study.

III.2. Study area and geological setting

The Baja California peninsula is a long finger of land in western Mexico extending south from the US state of California. Baja California is bounded to the west by the Pacific Ocean and to the east by the Gulf of California (also known as the Sea of Cortez) and at the northeast tip by the state of Sonora, which is the only land area that joins the Baja California peninsula to the rest of the country (Figure 3.2). The Baja California Peninsula is divided into two states, Baja California (Lower California) and Baja

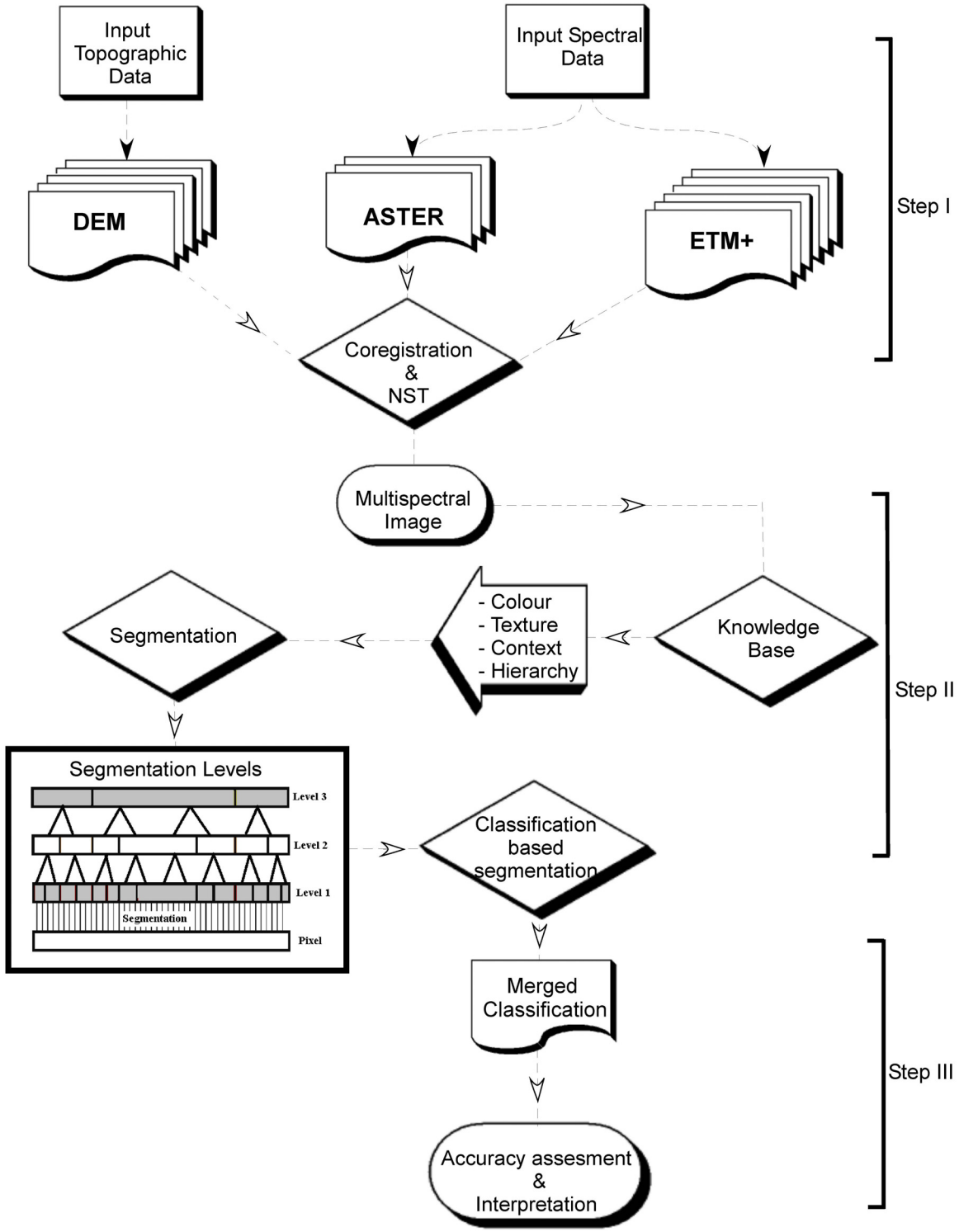

Figure 3.1. Flow chart summarizes the main steps used for semiautomated object classification approach.

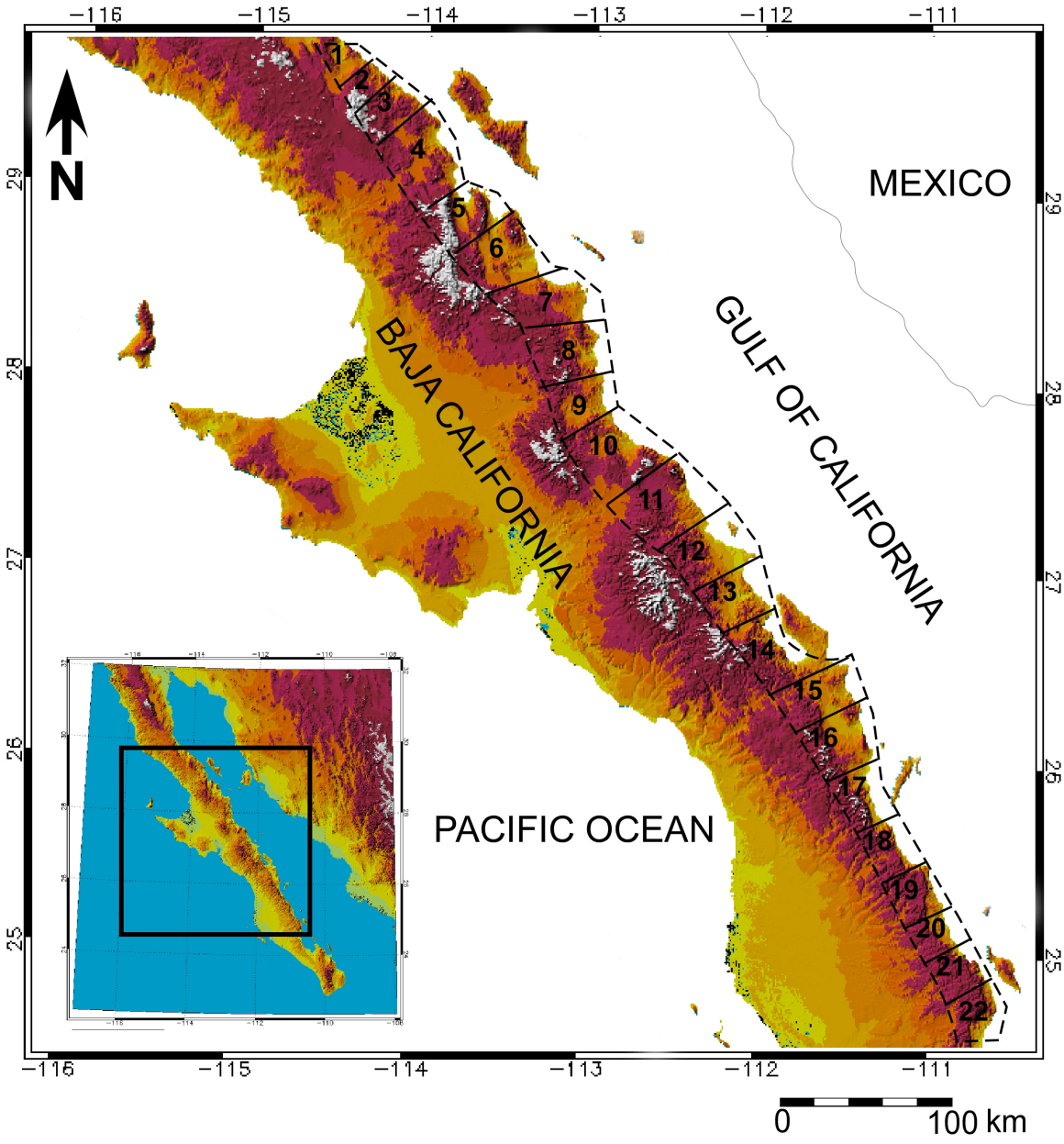

Figure 3.2. Location map of the study area. Twenty-two blocks were selected along the eastern coast of Baja California.

California Sur (Southern Lower California). In this study we will refer to both of these divisions as Baja California.

Previous tectonic and structural studies of Baja California, especially the eastern part of it suggest a complex geological evolution for the Gulf of California and the surrounding continental regions (Hamilton, 1961; Atwater, 1970; Karig and Jensky, 1972; Mammerickx and Klitgord, 1982; Gastil *et al.*, 1983; Lonsdale, 1989; Stock and Hodges, 1989). The tectonic evolution of the eastern Baja California has been controlled by dynamic processes of oblique continental rifting that are still poorly understood. Geologic structures, geomorphologic features, and sedimentary basins along the eastern side of Baja California preserve a critical record of these processes. Baja California is also considered as excellent modern example of a continental block, or terrain that has been horizontally translated ~ 300 km to the NW because of highly oblique rifting and sea floor spreading in the Gulf of California (Umhoefer and Dorsey, 1997). The peninsula was originally connected to the west coast of mainland Mexico but rifted and drifted away by differential movements of the Pacific and North American plates over the past 4-5 Myr.

III.3. Methodology

III.3.1. Data acquisition and ground-truth.

Six raw scenes (level 0) of Landsat 7 ETM+ imagery, acquired on 6 Jun 2000, 2 Jun 2001 and13 Jul 2001, were used in the present study. The available ancillary data included hard copy topographic maps (1:50,000 scale) and an SRTM digital elevation

model (DEM) with 90-m spatial resolution, in addition to thirty-two advanced spaceborn thermal emission and reflectance radiometer (ASTER) images which were used primarily to develop a 15-m spatial resolution DEM (El-Sobky and Dorobek, 2005). Table 3.1 summarizes the details of the data used for this study.

Field data gathering was conducted to collect the prevailing lithological types and ground positioning information needed in identifying and delineating training sample areas and calibrating the DEM. Ancillary scattered geologic maps and plotted hardcopy images were used in identifying various land cover features, especially the lithological rock units, and in describing their spectral characteristics.

III.3.2. Data preparation and image processing

The preprocessing technique is the first stage in any image processing sequence. To fulfill the basic requirements in terms of precision and accuracy, images must be corrected before proceeding with any manipulations. The two essential preprocessing techniques, Radiometric and geometric, are required to transform the 0-level (raw) images into a set of images ready for comparison and numerical combination. The radiometric preprocessing involves the rearrangement of the digital number (DN) in the images so that all areas of the image will have the same linear relationship between the DN and either radiance or backscatter (Moik, 1980).

Geometrical correction is the comparison of digital image content with a map or with another image in order to change the geometrical character of the former image (Mather, 1987). This process is very important for identification of training samples according to

Table 3.1. Spectral Channels of the Sensors Used in This study.

Sensor and Topographic Data	Spectral Channels	Wavelength (μm)	Spatial Resolution (m)
ETM+	Band 1*	0.452-0.514	30
(Enhanced **T**hematic **M**apper +)	Band 2*	0.519-0.601	30
	Band 3*	0.631-0.692	30
	Band 4*	0.772-0.898	30
	Band 5*	1.547-1.748	30
	Band 6	10.31-12.36	120
	Band 7*	2.065-2.346	30
	Band 8(pan) *	0.515-0.896	15
ASTER			
(Advanced **S**paceborne **T**hermal	VNIR		
Emission and **R**eflection	Band 1*	0.52-0.60	15
radiometer).	Band 2*	0.63-0.69	15
	Band 3N*	0.76-0.86	15
	Band 3B*	0.76-0.86	15
	SWIR		
	Band 4	1.600-1.700	30
	Band 5	2.145-2.185	30
	Band 6	2.185-2.225	30
	Band 7	2.235-2.285	30
	Band 8	2.295-2.365	30
	Band 9	2.360-2.430	30
	TIR		
	Band 10	8.125-8.475	90
	Band 11	8.475-8.825	90
	Band 12	8.925-9.275	90
	Band 13	10.25-10.95	90
	Band 14	10.95-11.65	90
Topographic Data:			
DEM			
	Shaded Relief		15
	Slope		15
	Aspect		15
	Average Convexity		15
	Average Curvature		15

map coordinates prior to classification, creating accurate scale maps, ensuring accurate distance and area measurements, and performing any other analysis that requires precise geographic locations. Rectification, by definition, involves dereferencing, which refers to the process of assigning proper map coordinates to image data, since all map projection systems are associated with map coordinates (Erdase manual, 1997). Polynomial equations are used to convert the source file coordinates to rectified map coordinates were the polynomial coefficients for the transformed equation are estimated through sets of ground control points (GCPs) (Jensen, 1986). The complexity of these polynomial equations depends on the degree of distortion in the image, the number of the GCPs and their locations relative to each other. The mathematical details of polynomial models can be found in Schowengerdt (1997).

The number of GCPs is basically controlled by the order of transformation. In general, the minimum number of GCP that is required to perform a transformation of order *t* can be estimated from the following equation:

$$Minimum\ Number\ of\ GCPs = (t+1)(t+2)/2 \qquad (1)$$

Nine GCPs were extracted from the topographic maps and used for each scene. We tried to avoid any substantial changes of these GCPs due to time differences between images and topographic maps by selecting the points away from any possible changes as possible. The number of the selected GCPs reflects that the second order polynomial transformation has been used in this study.

In most cases, a perfect fit of all GCPs does not occur and there are always differences between the desired outputs coordinates of the GCPs after transformation

and the original coordinates. Root mean square error (RMS) error is used to evaluate the accuracy of the transformation process, where RMS error is expressed as a distance in pixel widths in the same coordinate system that could be calculated for each GCP (equations 2 and 3).

$$R_i = \sqrt{XR_i^2 + YR_i^2} \tag{2}$$

where Ri represent the RMS error of GCPi, XRi is the X residual for GCPi and YRi is the Y residual for GCPi. The total RMS error can be calculated from the following formula:

$$T = \sqrt{1/n \sum_{i=1}^{n} XRi^2 + YRi^2} \tag{3}$$

where; T is the total RMS error, N is the number of GCP, and I the GCP number.

Bernstein (1976) pointed out that the maximum allowed RMS error for the geometrically corrected image is ±1 pixel, where as in the present study, the average calculated total RMS error for the study area is ± 0.2 pixel width. The nearest-neighbor interpolation technique is selected to resample the six ETM+ images to avoid any possible alteration of the pixels DN or any smoothing, which is not recommended before classification, and also to avoid the blocky effect of pixels.

The second important step after the rectification is to use the privilege of the ETM+ images over the TM, which is the release of the panchromatic band that has a 15-m spatial resolution. The 30-m spatial resolutions of the six ETM+ spectral bands are then improved through fusion with the ETM+ Panchromatic band to gain the panchromatic band spatial resolution (15-m). This has been done by applying the PanSharp automatic

algorithm (PCI Geomatica software), which preserves spectral characteristics of multispectral channels (Zhang, 1999 & 2002; Lewinski, 2006). The PanSharp automatic algorithm is a dedicated tool for fusing diverse satellite images of various spatial, spectral and radiometric resolutions. It also offers a feature of automatic resampling, i.e. adjusting the size of pixels in the multispectral image to the panchromatic one. The details of data fusion also appear in Savian and Landgrebe, 1991; Kunz *et al.*, 1997; Hahn and Statter, 1998; and Haala and Brenner, 1999. The advantage of this fusion relay essentially is that these bands are simultaneously acquired with the same conditions in terms of solar illumination, season, and sensor parameters, which minimizes or removes any possible spectral distortion that may occur as a result of the fusion (Liu, 2000).

Mosaic generation is the final step, where definite problems arise when attempting to perform this crucial step. There is no one correct approach to solve the problem of constructing mosaic imagery of varied temporal origin. We applied a combination of color balancing and intensity adjustment along with suitable feathering to match edges until an overall seamless image was obtained.

III.3.3. Why object oriented approach

Our primary aim in this part of study is to generate high resolution thematic maps using multiple sources of satellite images in addition to digital terrain data. The use of these multisource data has been successfully proven to resolve any classification ambiguities which might arise from using single-source data (e.g. Hoffer *et al.*, 1975; Strahler *et al.*, 1978; Fleming *et al.*, 1979; Richards *et al.*, 1982; Franklin *et al.*, 1986;

Jones e. al., 1988; Benediktsson, 1989b; Breiman, 1996; Richards and Jai, 1999). Object-oriented classification is then selected to incorporate this data. The reasons behind the selection of object-oriented classification are that it is one of the most important and advanced techniques that has proven, excellent capabilities to accommodate multisource data; and it takes the reliability or uncertainty of each data source into account, which is very important parameter that determine how strongly a given source contributes to the multisource consensus pool (Mather and Tso, 2001). In object-oriented classification, the reliability and uncertainty are considered by assigning a specific input weight parameter to each data source, based on the spectral separability analysis for optical data sources only. If these weighting parameters are not chosen properly, then the multisource consensus will give disappointing results even though it based on a theoretically robust mechanism. Table 3.2 summarizes the main differences between the object-oriented classification approach and the conventional pixel-based classification techniques.

III.3.4. Principles of object oriented image analysis

As pointed out before, the main concept behind the object-oriented classification is to use the image objects rather than the image pixels simply because image objects have the important semantic information necessary to interpret the images. Object-oriented image analysis refers to the extraction of real-world objects, which means it utilizes shape, neighborhood and other contextual information (Baatz and Schäpe, 1999;

Table 3.2. Differences Between Pixel-Based and Object Oriented Classification.

Pixel-Based Classification	**Object Oriented Classification**
Pixel-based land cover map	Image object segmentation polygons
Based on "binary theory," where pixel is classified into only one class or remains unclassified	Based on "fuzzy theory," where one pixel may show affinity to more than one class and the image object will have membership values from 1 to 0
Requires values of gain and offset, sun elevation angle and ground visibility	Applies directly to the image
One-time step classification	Step-by-step classification
Uses the spectral signature as a criterion for classification	Uses properties like heterogeneity, represented by color and shape as criteria for segmentation of the normalized input features
Uses only spectral information and cannot incorporate any ancillary data.	Incorporates spectral and spatial ancillary data like DEM and other vector data besides the image spectral bands
Filters usually applied to reduce image distortion.	Filters usually not used

Benz *et al.*, 2004). In comparison to the pixel-based approaches, the basic processing units are image objects and not single pixels. In other words, this technique allows the analyst to decompose the scene into many relatively homogenous image objects (referred to as patches or segments) using a multiresolution image segmentation process (Benz et al 2004). These objects of interest have to be extracted in a first step called segmentation. During the subsequent classification, the segmented objects are systematically arranged in groups or categories according to defined criteria determined by the user in the class description. In this study, classification is performed using an algorithm developed by Definiens/Munich (2003). In eCognition, classification is based on thresholds and a fuzzy classification system, which are in turn based on membership functions. So a fuzzy classification set is a set whose elements have degrees of membership, which may defined as a full member (100% membership) or a partial member (between 0% and 100% membership). Mathematically, this degree of element membership is defined by a membership function. The major advantage of this theory is that it translates feature values of arbitrary range into fuzzy values between 0 and 1. Figure 4 shows how image analysis is realized in eCognition software. The first step of object-oriented image analysis is always the image segmentation. In eCognition the applied algorithm is called multiresolution segmentation, a technique that allows users to segment images on different levels, with different resolutions and variable segmentation based on four parameters: weight of participation in the segmentation, scale, color, shape (smoothness and compactness). All those parameters are weighted from 0 to 1 to determine the heterogeneity of an image object. During the process of segmentation,

adjacent objects are only merged, where the growing of heterogeneity (f) is the smallest; this underlying optimization procedure of the clustering process stops if a defined threshold (maximum allowed heterogeneity) is exceeded. After the segmentation, we get image objects constituted of homogeneous pixels. Then classification is performed using the objects rather than single pixels. The multiresolution segmentation approach allows for segmentation at different spatial resolutions simultaneously (Chen *et al.*, 2005). Besides the spectral character of the image objects, their attributes such as shape, texture, etc. are the new input for an advanced and reliable classification. Classification using this technique is initially based on a process of image segmentation which is effectively used to create polygonal objects representing spectrally homogenous units at a certain scale. Table 3.3 summarizes the parameters of segmentation that are used in this study for three segmentation levels. See Baatz and Schäpe (2000) and the eCognition user guide (2004) for the detailed description of the techniques and the equations used.

On the other hand, the issue of the different scale of measurements, i.e. different data sources are likely to have different measurements scales, should be solved first before performing segmentation. Normal score transformation is used to normalize the input data to be mapped into the same scale. The normal score is a dimensionless quantity derived by subtracting the population mean from an individual (raw) score and then dividing the difference by the population standard deviation. This transformation will ensure a transformation of the input data into a normally distributed data, with a mean zero and standard deviation unity (Figure 2). As reported before, three target levels

were identified for the study area (Figures 3.3 and 3.4): Level (1) represents small objects at an initial segmentation level to differentiate subclasses by spectral and structure characteristics. Level (2) is the main target of the classification rules. Level (3) was generated through a "classification-based segmentation" procedure that aims to unite objects of the same classified lithological units into larger spatial units. Additionally, small units below a certain threshold surrounded by bigger units classified as similar developmental phases were reassigned to the respective classes of the majority of neighbor objects. This is achieved through a "relation to neighbor objects" parameter in the rule-base (eCognition Manual, 2003).

III.4. Results and discussion

The area of study has been divided into 22 blocks (Figure 3.2). This division facilitated the classification process and avoided the crash of the classification model, where it was impossible to classify the whole study area as one unit. The eCognition™ version 4.0 professional software (Definiens Imaging, 2003) provides a unique object-oriented rule-based approach to image classification (Baatz *et al.*, 2003). Block 4 and Block 8 (Figure 3.2) have been selected to show the classification results. For Block 4, the final classification resulted in thirteen possible classes (Figure 3.5), where as twelve classes were recognized in Block 8 (Figure 3.6). The input layers have been weighted differently from one block to another based upon the degree of spectral seperabilities of each classified rock unit. Unsupervised classification was used first to generate feature

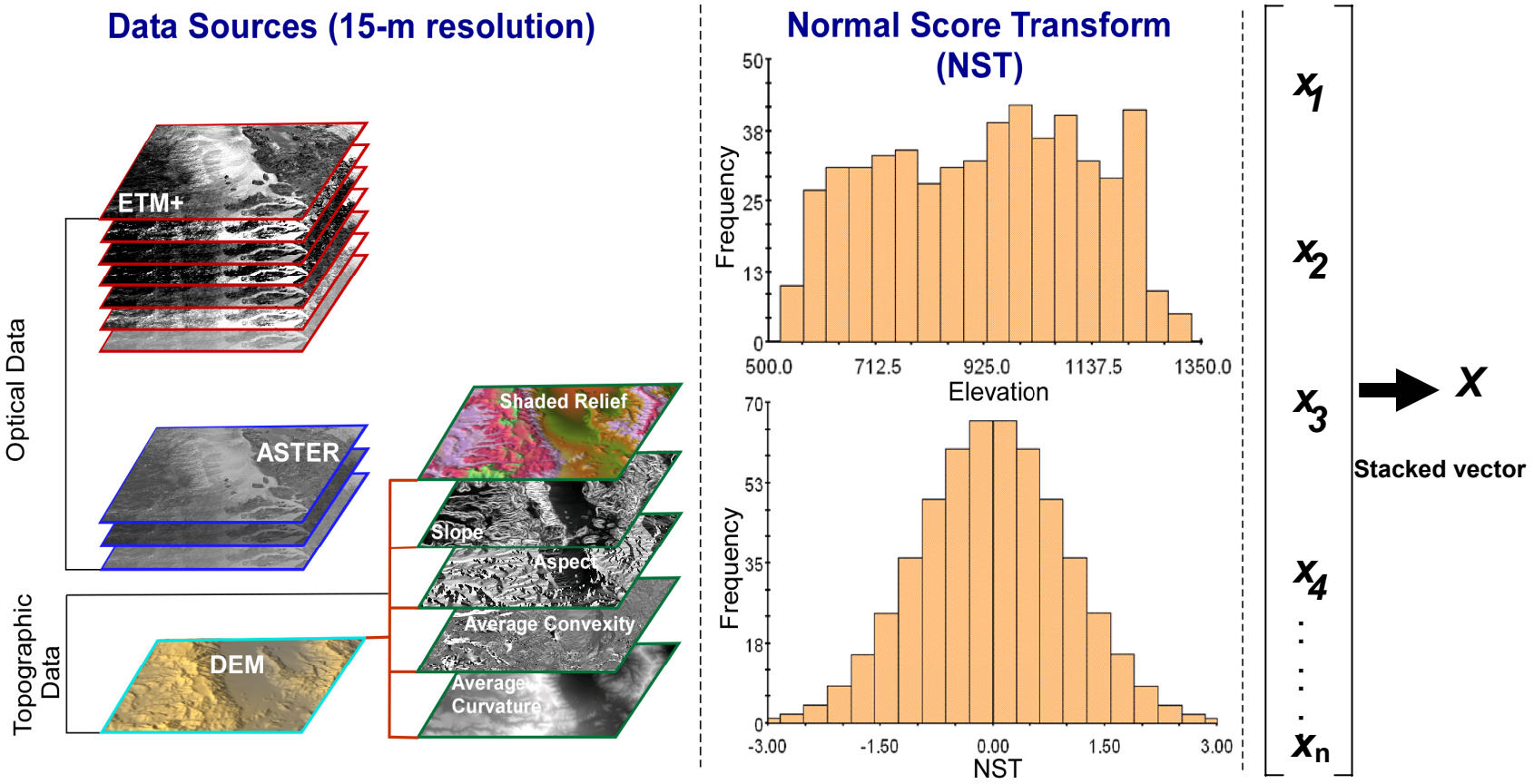

Figure 3.3. The integration of optical and terrain data and normal score transformation process.

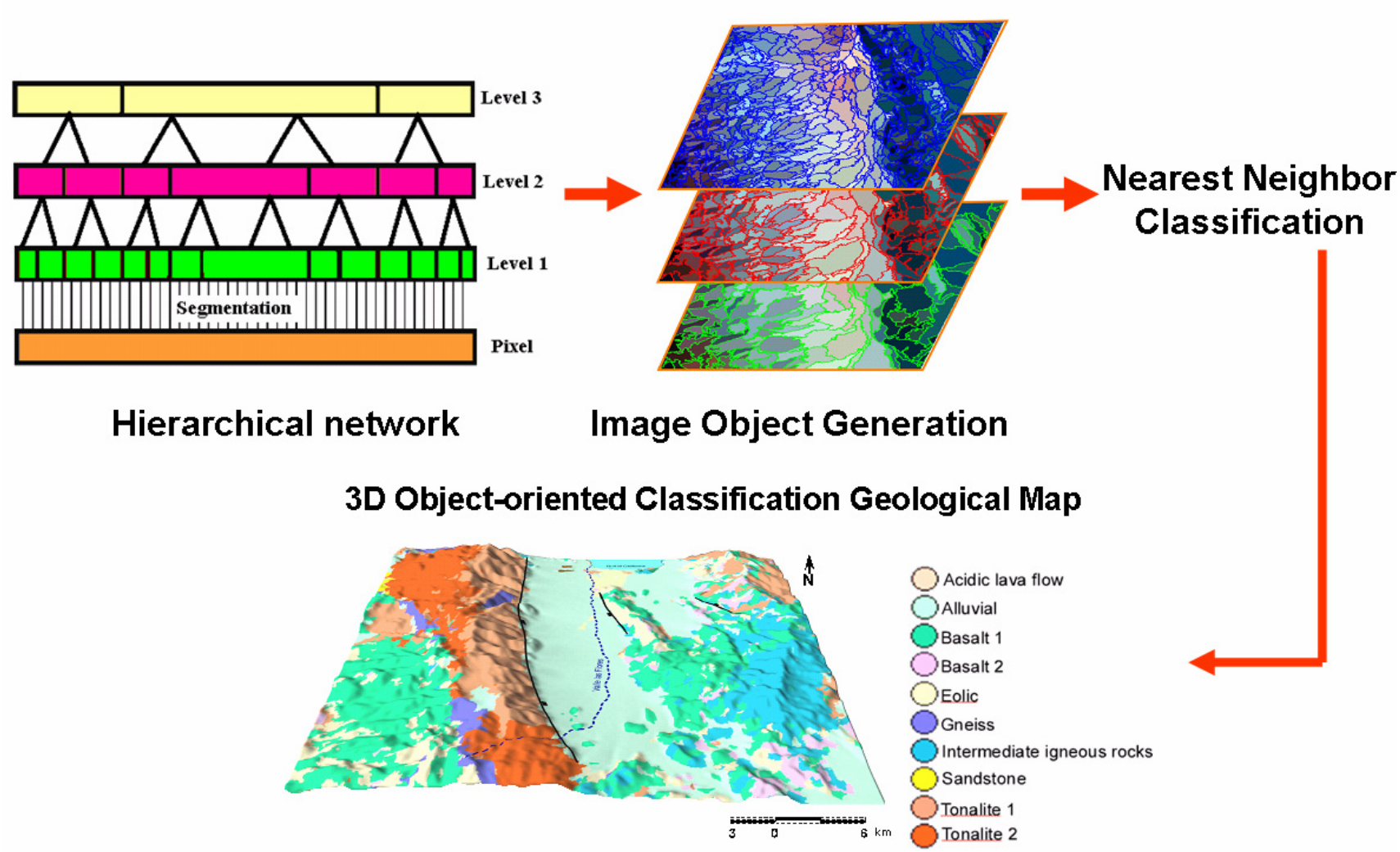

Figure 3.4. Example of the major steps for implementing object-oriented classification in eCognition software.

Table 3.3. Segmentation Criteria and Parameters Used in the Present Study.

Segmentation criteria		Fusion value based on heterogeneity $f = w.h_{color} + (1-w).h_{Shape}$		
		Color $h_{color} = \sum_c w_c \left(n_{Merge}.\sigma_c^{Merge} - \left(n_{Obj1}.\sigma_c^{Obj1} + n_{Obj2}.\sigma_c^{Obj2} \right.$	**Shape** $h_{shape} = w_{cmpct}.h_{cmpct} + (1 - wc_{mpct}).h_{smooth}$	
			Smoothness $h_{smooth} = n_{Merge}.\frac{l_{Merge}}{b_{Merge}} - \left(n_{Obj1}.\frac{l_{Obj1}}{b_{Obj1}} + n_{Obj2}.\frac{l_{Obj2}}{b_{Obj2}} \right.$	**Compactness** $h_{cmpct} = n_{Merge}.\frac{l_{Merge}}{\sqrt{n_{Merge}}} - \left(n_{Obj1}.\frac{l_{Obj1}}{\sqrt{n_{Obj1}}} + n_{Obj2}.\frac{l_{Obj2}}{\sqrt{n_{Obj2}}} \right.$
Segmentation level	1	0.8	0.8	0.2
	2	0.8	0.7	0.3
	3	0.8	0.5	0.5

Note: f is the overall fusion value, σ is the standard deviations of spectral values in each layer, w is the user defined weight for color against shape for each layer, n is the object size, l is the perimeter of the object, b is the perimeter of the bounding box of an image object.

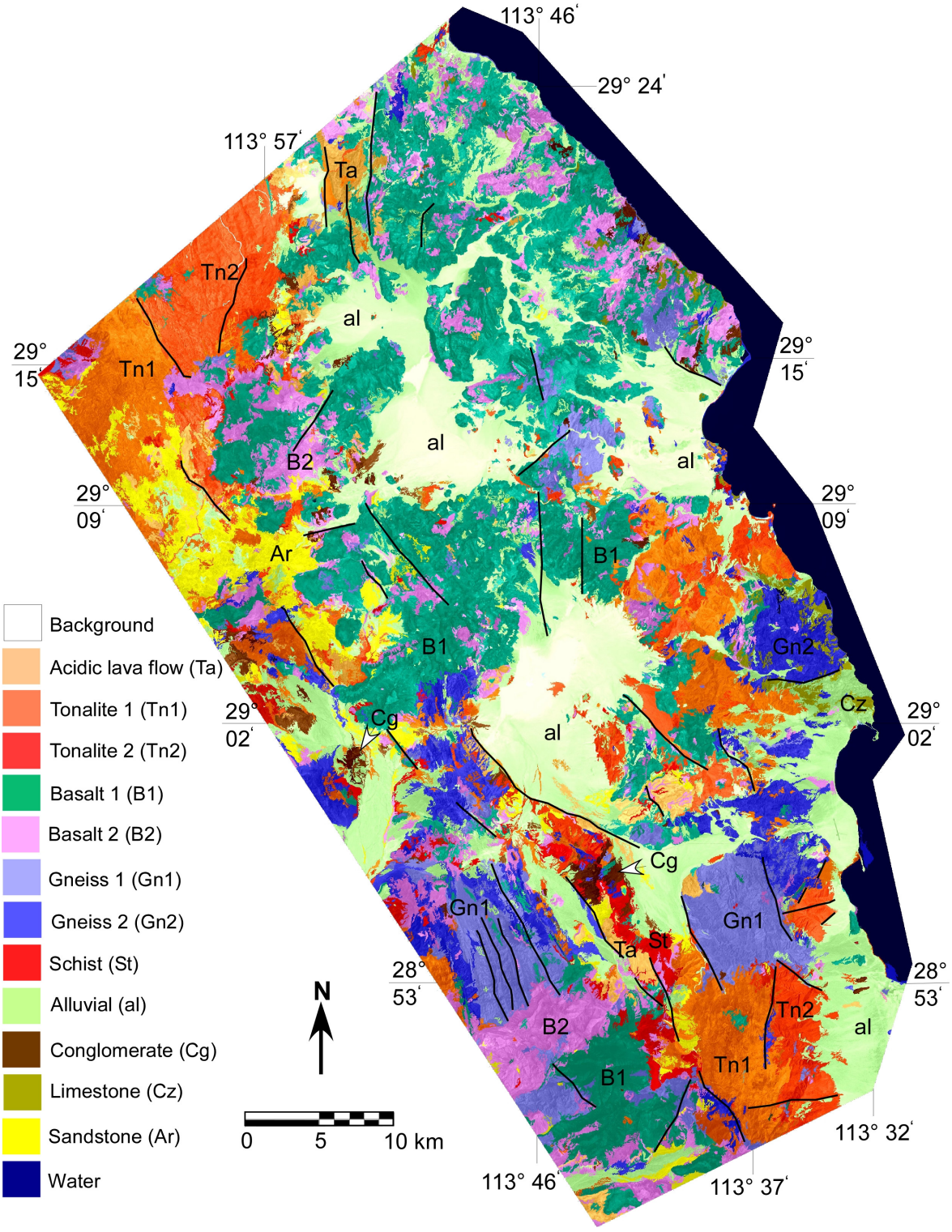

Figure 3.5. Block 4 object-oriented classification geological map.

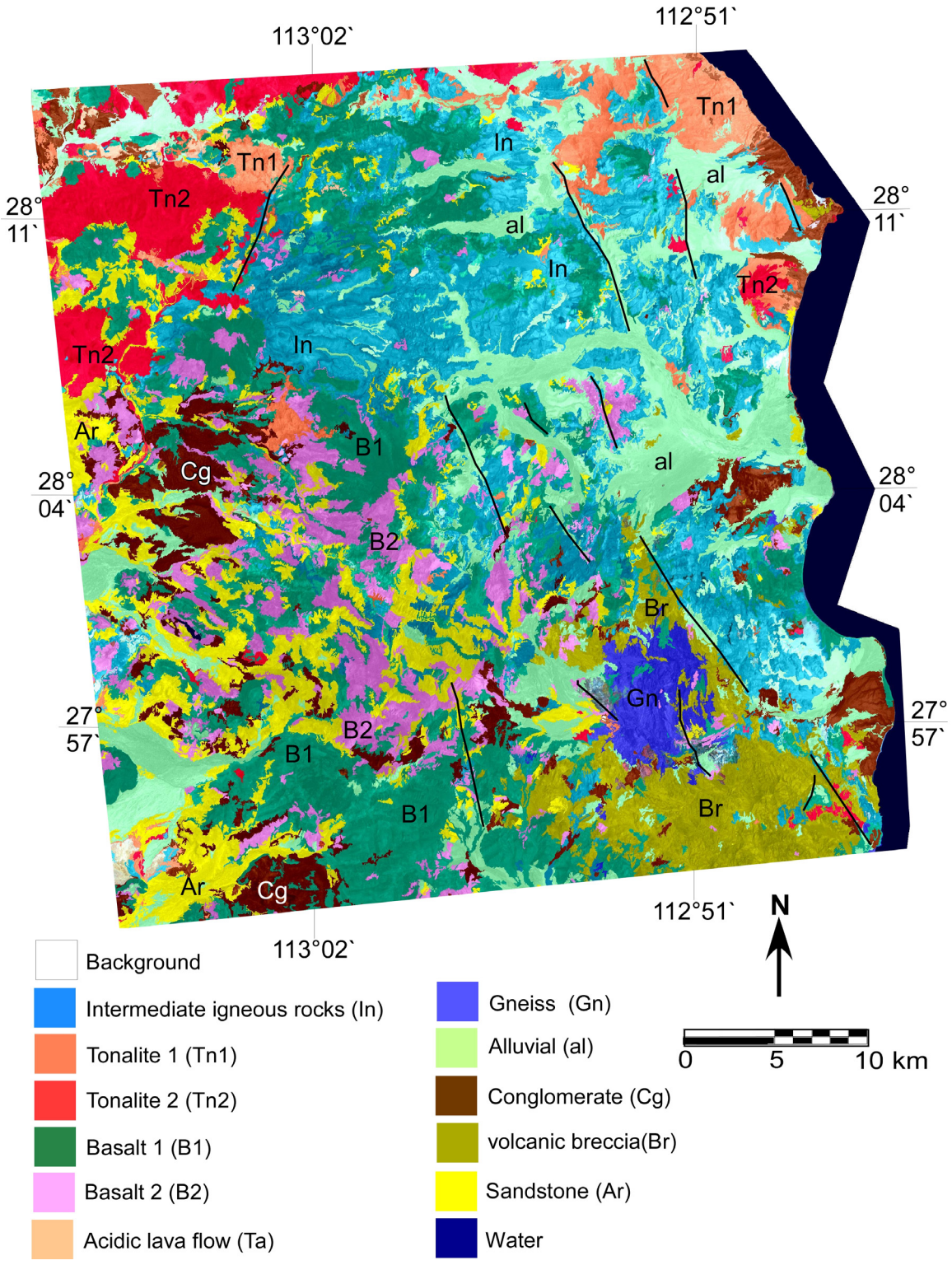

Figure 3.6. Block 8 object-oriented classification geological map.

space images, which were further used to define the degree of separabilities between the different rock units (El-Sobky, 1999). The input bands were assigned different weights, so the layers that usually exhibit high separation between classes in their feature space were assigned higher weights than those with low separations. Quality assurance is a very important step after any classification process in to allow a degree of confidence to be attached to the results and also to confirm that the analysis objectives have been realized (Richards 1993). In this study, three main types of accuracy assessments has been selected to quantify the degree of classification accuracy, which are 1) accuracy assessment by classification stability; 2) accuracy assessment by best classification results; and 3) accuracy assessment by error matrix based on test areas.

First, accuracy assessment by classification stability is used only for the fuzzy logic classification algorithm, which relies on the membership degree between the classified objects. In other words, it is used to show the difference between the degree of membership of the best and second-best classification of an object that has been assigned to specific classes. Table 3.4 and Table 3.5 show the classification stabilities for the classes defined in Blocks 4 and 8 respectively. These statistical results have been calculated for image objects in the entire blocks. The differences of the best and second best classification membetship values for each class are defined by the mean in these tables, it is clearly obvious that the higher the values of the mean, the higher the classification stability of the specific class. So for Block 4, tonalite, basalt 2, limestone and water show the highest mean values and reflect good classification stabilities of

Table 3.4. Accuracy Assessment by Classification Stability of Block 4.

Class	Objects	Mean	StdDev	Min.	Max.
Ta	267	0.061	0.063	2.056E-005	0.52
Tn1	613	0.093	0.159	0.00018	1
Tn2	614	0.092	0.099	4.410E-006	0.86
B1	1642	0.052	0.056	4.410E-006	0.86
B2	846	0.109	0.219	4.148E-005	1
Gn1	351	0.062	0.116	7.253E-005	1
Gn2	397	0.085	0.134	0.00016	1
St	101	0.028	0.031	9.292E-005	0.18
al	1661	0.061	0.198	0.00010	1
Cg	116	0.065	0.124	0.00055	1
Cz	59	0.082	0.085	0.00369	0.57
Ar	248	0.045	0.076	0.00059	0.64
Water	54	0.198	0.165	0.00742	0.68

Table 3.5. Accuracy Assessment by Classification Stability of Block 8.

Class	Objects	Mean	StdDev	Min.	Max.
In	1429	0.215	0.253	7.534E-005	1
Tn1	296	0.098	0.103	0.00011	1
Tn2	327	0.100	0.081	0.00014	0.57
B1	1128	0.067	0.094	0.00021	1
B2	526	0.175	0.271	0.00015	1
Ta	23	0.070	0.055	0.00126	0.17
Gn	80	0.218	0.251	0.00071	1
al	854	0.077	0.114	0.00017	1
Cg	399	0.067	0.127	2.872E-005	1
Br	374	0.103	0.094	8.219E-005	1
Ar	539	0.037	0.038	2.241E005	0.34
Water	31	0.95	0.171	0.0273	1

these classes over the other classes for this block. On the contrary, gneiss, intermediate igneous rocks, tonalite 2, volcanic breccia and water exhibited the highest mean values and hence good classification stabilities for Block 8. For the rest of the classes in both blocks, the low values of their means indicate that there is no big difference between the best and the second-best classification membership values for each class.

Second, accuracy assessment by best classification results is described based on the values of the highest membership values of an object for each class. In other words, the high mean values indicate that most or even all the class objects have been classified on the basis of higher membership values, as indicated in Tables 3.6 and 3.7, which prove that all class objects have been significantly assigned to the right class.

Finally, concerning the accuracy assessment by error matrix, ground truth data extracted from the available geologic maps were used as a mask in eCognition. The error matrix is basically the relation between the classified objects versus the true data. Table 3.8 and Table 3.9 show the error matrix final results for Block 4 and Block 8, where two types of accuracies, user and producer, are calculated for each classified rock unit. The producer accuracy refers to the percentage of each class that has been correctly classified, where the user accuracy refers to the percentage of the classified area that correctly belongs to this class. Numerically speaking, the producer accuracy of sandstone class in Block 4 was 80% and the user accuracy of the same class was 89.5%; this means that 80% of the sandstone has been correctly classified and 89.5% of this sandstone area is correctly defined as sandstone. On the other hand, the overall accuracy

Table 3.6. Accuracy Assessment of the Classified Image by the Best Classification Result of Block 4.

Class	Objects	Mean	StdDev	Min.	Max.
Ta	267	0.936	0.074	0.524	1
Tn1	613	0.954	0.061	0.528	1
Tn2	614	0.943	0.078	0.502	1
B1	1642	0.958	0.047	0.500	1
B2	846	0.940	0.067	0.605	1
Gn1	351	0.958	0.064	0.523	1
Gn2	397	0.935	0.077	0.565	1
St	101	0.955	0.048	0.680	1
al	1661	0.937	0.076	0.512	1
Cg	116	0.913	0.098	0.542	1
Cz	59	0.854	0.103	0.570	1
Ar	248	0.953	0.063	0.552	1
Water	54	0.939	0.112	0.592	1

Table 3.7. Accuracy Assessment of the Classified Image by the Best Classification Result of Block 8.

Class	Objects	Mean	StdDev	Min.	Max.
In	1429	0.883	0.106	0.502	1
Tn1	296	0.911	0.095	0.519	1
Tn2	327	0.956	0.067	0.577	1
B1	1128	0.940	0.073	0.505	1
B2	526	0.904	0.114	0.511	1
Ta	23	0.903	0.094	0.657	1
Gn	80	0,913	0.108	0.513	1
al	854	0.933	0.077	0.502	1
Cg	339	0.929	0.087	0.533	1
Br	374	0.925	0.079	0.543	1
Ar	539	0.948	0.053	0.591	1
Water	31	0.974	0.077	0.575	1

Table 3.8. Error Matrix by Test Areas for Block 4.

Classification Data		Ta	Tn1	Tn2	B1	B2	Gn1	Gn2	St	al	Cg	Cz	Ar	Water	Total
	Ta	**72**	7	10	0	0	0	0	0	0	0	0	0	0	78
	Tn1	10	**229**	20	0	0	0	0	0	0	0	0	0	0	259
	Tn2	0	40	**201**	0	0	0	0	0	0	0	0	0	0	221
	B1	0	0	0	**389**	15	0	0	0	0	0	0	0	0	404
	B2	0	0	0	45	**268**	0	0	0	0	0	0	0	0	283
	Gn1	0	0	0	0	0	**134**	30	0	0	0	0	0	0	164
	Gn2	0	0	0	12	5	30	**124**	0	0	0	0	0	0	171
	St	0	0	0	0	0	0	0	**32**	0	0	0	0	0	32
	al	0	0	0	0	0	0	0	0	**415**	0	0	17	0	432
	Cg	0	0	0	0	0	0	0	0	0	**23**	0	0	0	23
	Cz	0	0	0	0	0	0	0	0	1	0	**7**	0	0	8
	Ar	0	0	0	0	0	0	0	0	8	0	0	**68**	0	76
	Water	0	0	0	0	0	0	0	0	0	0	0	0	**16**	16
	Total	82	276	241	446	318	164	154	32	424	23	7	85	16	2207

	Land cover types												
	Ta	**Tn1**	**Tn2**	**B1**	**B2**	**Gn1**	**Gn2**	**St**	**al**	**Cg**	**Cz**	**Ar**	**Water**
Producer's accuracy (%)	87.8	83	83.4	87.2	84.3	81.7	80.5	100	97.9	100	100	80	100
User's accuracy (%)	92.3	88.4	91	96.2	94.7	81.7	72.5	100	96.1	100	87.5	89.5	100
Overall accuracy (%)	**89.6** %												

Table 3.9. Error Matrix by Test Areas for Block 8.

Classification Data		Reference Data												
		In	**Tn1**	**Tn2**	**B1**	**B2**	**Ta**	**Gn**	**al**	**Cg**	**Br**	**Ar**	**Water**	**Total**
	In	**241**	20	9	0	0	11	0	0	0	0	0	0	281
	Tn1	18	**82**	22	0	0	0	0	0	0	0	0	0	122
	Tn2	17	23	**166**	0	0	0	0	0	0	0	0	0	202
	B1	0	0	0	**336**	66	0	4	0	0	0	0	0	406
	B2	0	0	0	70	**169**	0	0	0	0	0	0	0	239
	Ta	2	0	0	0	0	**8**	0	0	0	0	0	0	10
	Gn	0	0	0	6	7	0	**38**	0	0	0	0	0	51
	al	0	0	0	0	0	0	0	**207**	0	0	22	0	229
	Cg	0	0	0	0	0	0	2	1	**89**	2	0	0	94
	Br	0	0	0	0	0	0	6	0	2	**96**	0	0	104
	Ar	0	0	0	0	0	0	0	23	2	0	**108**	0	133
	Water	0	0	0	0	0	0	0	0	0	0	0	**16**	16
	Total	278	125	197	406	242	19	50	231	93	98	130	16	**1887**

	Land cover types											
	In	**Tn1**	**Tn2**	**B1**	**B2**	**Ta**	**Gn**	**al**	**Cg**	**Br**	**Ar**	**Water**
Producer's accuracy (%)	85.8	67.2	82.2	82.8	70.7	80	74.5	90.4	94.7	93.3	81.2	100
User's accuracy (%)	86.7	65.6	84.3	82.8	69.8	42.1	76	90	96	98	83.1	100
Overall accuracy (%)	**82.5** %											

for each classified block is also calculated. So, for Block 4, the overall classification accuracy was 89.6%, where as it was 82.5% for Block 8. More analysis of the error matrix tables reveals that the number of misclassified objects is defined. For example, in Block 4, 15 objects of basalt 1 were misclassified as basalt 2, where as in Block 8 and for the same rock units, 66 objects of basalt 1 were misclassified as basalt 2. Actually this example shows that in block 8 classified objects of basalt1 get confused with basalt 2 more than in Block 4. However, we found that in order to overcome and decrease this number of misclassified objects and hence increase the overall accuracy of the classification, we can go back and do two things. First, we can increase the number of defined objects for the nearest neighbor classifier, which may enhance the relationship function of the two units. Second, we can increase the weight of the input layers to show a tendency towards more reparability behavior of these units in the future space images.

III.5. Summary and conclusions

In this paper, we presented the object-oriented classification technique using a vector-stacked method as an unconventional classification approach to classify the eastern part of the Baja California peninsula. Our primary goal was to generate continuous and high resolution geologic maps for the entire area between the Baja peninsular divide and the western coastal line of the Gulf of California. This area has been divided into twenty-two blocks. A combination of optical and terrain data sets was successfully integrated and used after precise coregistration of all inputs (0.2 RMSE). We used eCognition software V.4.0 to implement the segmentation process based on

image objects rather than on a single pixel. All the optical data were preprocessed both radiometrically and geometrically and then the Pansharp automatic algorithm was used to improve the ETM+ bands resolution through a fusion process with the panchromatic band, a process that ended with 15-m spatial resolution images. Two blocks were selected to show the classification end results, Block 4 and Block 8. Thirteen surfacial lithological classes were recognized in Block 4, where only twelve classes were identified in Block 8. Three main types of accuracy assessments were used to quantify and hence evaluate the classification results. The results of the three methods were completely satisfactory and confirmed the power of the object-oriented classification as a very efficient unconventional classification approach.

CHAPTER IV

QUANTIFYING THE FORCING FACTORS RESPONSIBLE FOR THE TECTONO-GEOMORPHOLOGICAL EVOLUTION OF THE NEOGENE RIFT BASINS, BAJA CALIFORNIA

The Gulf of California and its surrounding land areas provide a classic example of recently rifted continental lithosphere, where back-arc stretching of a continental volcanic arc has culminated in the ongoing seafloor spreading that characterizes the present-day axis of the gulf. The recent tectonic history of eastern Baja California, which includes most of the land area eastward of the main drainage divide that extends north-south along the length of the peninsula, has been dominated by oblique rifting that began at about 5 Ma. Thus, extensional tectonics, bedrock lithology, long-term climatic changes, and evolving surface processes have controlled the tectono-geomorphological evolution of the eastern part of the peninsula since 12 Ma. No previous studies, however, examined the effect of these combined factors on the current tectono-geomorphological characteristics of eastern Baja California.

In an attempt to assess the factors that affected the geomorphologic development along the eastern side of Baja California, thirty-four drainage basins were extracted from a 15-m-resolution absolute digital elevation model (DEM). Thirty morphometric parameters were extracted; these parameters were then reduced using principal component analysis (PCA). The first five principal components have accounted for

80.77% variance and are used as the input variables for cluster analysis. Four major groups of basins are defined by interpreting the hierarchical tree.

Stream-length gradient indices were measured, using a Hack profile, for the main stream in each of these basins. Bedrock lithologies and alluvium were plotted along the stream profiles to identify any relationship between lithology, structure, and stream gradient. The extracted stream length gradient indices highlight the differential rock uplift that has occurred along fault escarpments bounding the basins. Further, our results indicated that drainage basins in the eastern rift province of Baja California could be classified according to the dominant geomorphologic controlling factors (i.e., fault-controlled, lithology-controlled, or hybrid basins).

Using slope-area analysis, steepness and concavity indices were extracted for bedrock channels within the thirty-four drainage basins. A reference concavity of 0.37 was used to allow a direct comparison of steepness indices for the basins. The results were highly correlated with stream length-gradient indices for each basin. Nine basins exhibiting steepness index values greater than 0.07 indicated a strong tectonic signature and possible higher uplift rates in these basins.

IV.1. Introduction

The Baja California peninsula is kinematically linked to the Gulf of California rift system. Although this area has been studied extensively from the tectonic point of view, there is limited understanding of the relationships between progressive surface deformation and its effects on sedimentation, drainage-network and geomorphologic

evolution, especially during the last few million years of deformation. An understanding of recent surface deformation will provide insight into the styles, rates, and processes of ongoing tectonic activity in this region.

The eastern part of the Baja California peninsula has evolved through time in response to multiple episodes that exhibited complex changes in tectonic driving forces. complicated fault networks, rotating crustal blocks and continuous mountain ranges were formed during the past ~ 25 million years as a result of the long-term convergent movements of the pacific plates relative to the North American plate (Powell *et al.*, 1993; DeMets, 1995; Dickinson, 1996; Atwater and Stock, 1998). For about the last 15 million years, divergent motion occurred between the two plates and the crustal deformations culminating in the oblique rifting and extension (Stock and Hodges, 1989; Dickinson, 1996; Atwater and Stock, 1998; Axen and Fletcher, 1998). As a result of these transtensional movements, regional subsidence occurred, and Miocene-to-Pleistocene fault-bounded sedimentary basins evolved (Bartholomew, 1968; Quinn and Cronin, 1984; Kerr, 1982; Winker, 1987; Winker and Kidwell, 1996). The primary mechanisms for the formation of these sedimentary basins are the lithospheric extension, which creates rift basins and passive continental margins, and lithospheric contraction, which creates back-arc basins.

Geomorphometric indices of the drainage network are valuable tools in revealing the evaluation of active tectonics because they usually provide significant and sufficient criteria to define the topographic adjustment that occurred as a result of rapid or slow rates of prevailing tectonic activities. The links between tectonically generated

topography and surficial drainage networks have been investigated in a number of tectonic settings (e.g., compressional orogens and their associated foreland basins: Tucker and Slingerland, 1996; Schlunegger *et al.*, 1998; Kühni and Pfiffner, 2001; Schlunegger and Hinderer, 2001; intracontinental strike-slip deformation zones: Replumaz *et al.*, 2001), although intracontinental rift systems and their associated rift-flank uplifts have probably been investigated more extensively than any other setting (e.g., Braun and Beaumont, 1989; Frostick and Reid, 1989; Gilchrist and Summerfield, 1990; Summerfield, 1991; Foster and Gleadow, 1992; Ten Brink and Stern, 1992; Gawthorpe and Hurst, 1993; Arvidson *et al.*, 1994; Seidl *et al.*, 1996; Gawthorpe and Leeder, 2000; Doglioni *et al.*, 2003). Most tectono-geomorphologic studies of intracontinental rift systems have focused on long-wavelength topographic variations that are most likely related to the deformation and rheological evolution of the continental lithosphere during and after rifting. Far less research, however, has focused more on local structural features (e.g., individual half-graben elements and transfer fault zones) and the topographic and drainage patterns that are associated with these features. Even less is known about how local tectono-geomorphology is related to the longer-wavelength topographic variations. Few integrated studies have investigated all scales of geomorphologic and drainage evolution as they relate to various scales of tectonic deformation and tectonically generated topography (cf. Arvidson *et al.*, 1994).

The relationship between tectonics and both initiation and evolution of basin drainages has been the focus of many workers (cf. Antonie *et al.*, 2000; Benito *et al.*, 2000; Bogaart and van Balen, 2000; Colombo *et al.*, 2000; Krzyszkowski *et al.*, 2000;

Kusky and El-Baz, 2000; Latrubesse and Rancy, 2000; Maddy *et al.*, 2000; Stokes and Mather, 2000; Tebbens and Veldkamp, 2000; Veldkamp and Van Dijke, 2000; Clift *et al.*, 2001; Hsieh and Knuepfer, 2001; Maddy *et al.*, 2001; Monecke *et al.*, 2001; Moore and Larkin, 2001; Stouthamer and Berendsen, 2000; Harkins *et al.*, 2002), Since the exposed lithology, tectonics, and prevailing climate are the three major forcing factors controlling the morphotectonics of this territory (Figure 4.1), as elsewhere, our efforts in this paper has been increasingly focused to understand the link between drainage basins geomorphometric indices and the tectonic activities and to define the dominant forcing factors that are most probably responsible for basins tectono-geomorphometric developments.

This paper examines the sensitivity of the morphometric indices to reveal the possible ancient and recent tectonic activities along the eastern coast of the Baja California peninsula. Also it provides a test of the usefulness of multivariate analysis as a preliminarily step to reduce the geomorphometric parameters into a number of PCs which are then used in the cluster analysis process to group the basins by the degree of similarity between them. This paper is organized as follows. In Section 3, we give the necessary background in geomorphometric parameters extraction, their meanings, and their sensitivities to the drainage-basin behaviors. Multivariate statistical analysis will be introduced as a valuable method for both data reduction and classification. Stream

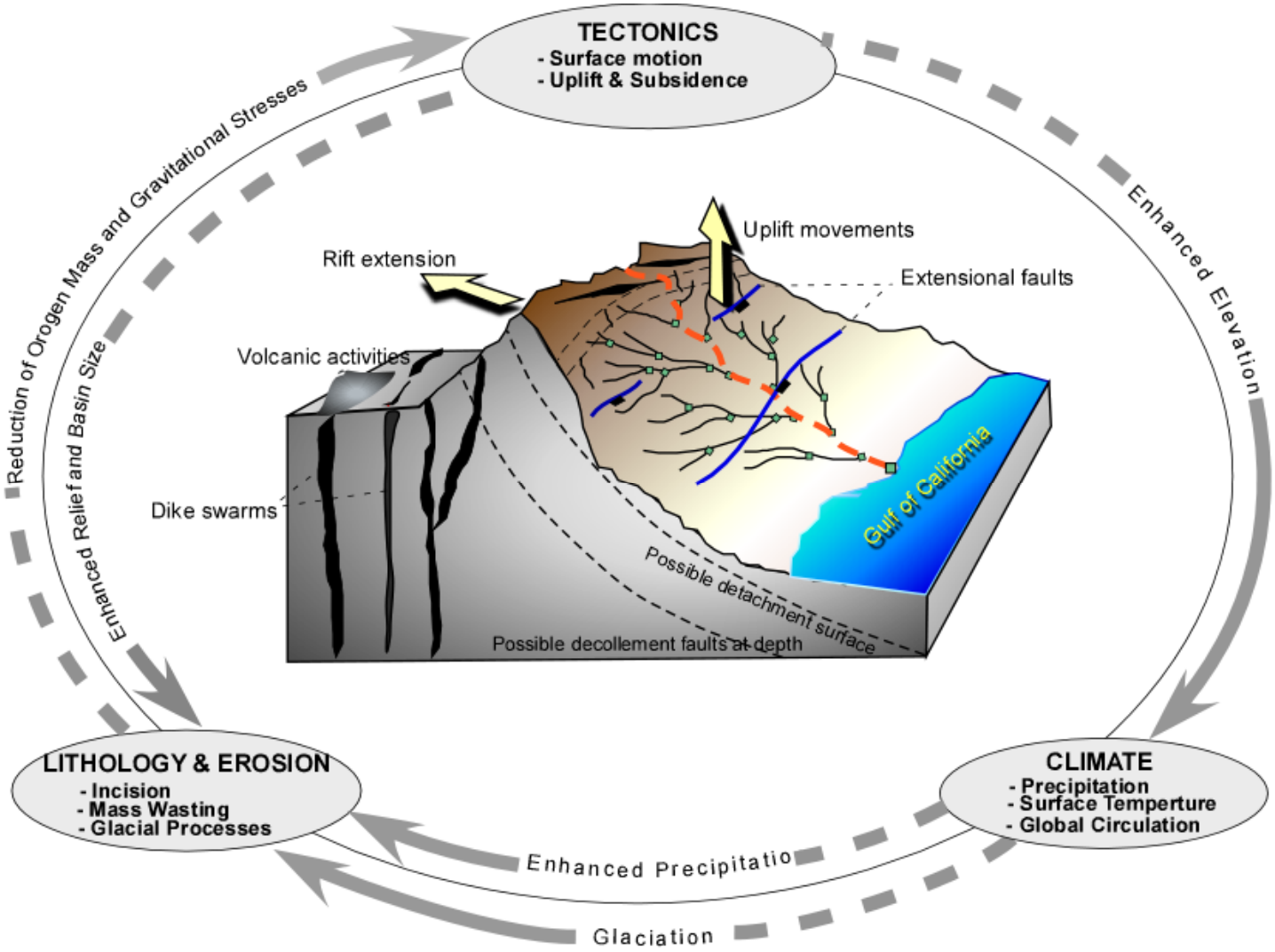

Figure 4.1. The fundamental controls on the relief structure of Baja mountain belts, which are tectonically controlled by rock uplift, climatic condition, bedrock erodability and river incision.

profile analysis is introduced to examin both stream length-gradient index and area-slope analysis. Finally, in Section 4 presents results and discussion, followed by the summary and conclusions in Section 5.

IV.2. Study area and regional tectonics

The Baja California peninsula is considered to be one of the most important locations to study rift tectonics. The Baja California peninsula is 800 miles long, which make it one of the longest peninsulas in the world. The peninsula is also very narrow, averaging less than 70 miles in width with the narrowest part only 26 miles wide. The focus of our study is the central domain, between lat ~ 24^0 N and lat ~ 29^0 N, which is almost two-thirds of the Gulf Extensional Province, a region of normal and strike-slip faults and basins that surrounds the Gulf of California at its western side (Umhoefer et. al., 1994; Zanchi 1994) (Figure 4.2). The western edge of the Gulf Extensional Province is the main gulf escarpment. In this area, the Neogene tectonic history of eastern Baja California (includes most of the land area eastward of the main, north-south oriented, drainage divide that extends along the length of the peninsula) has been controlled by oblique rifting. The Baja California peninsula is considered a direct product of rifting processes that began at ~12 Ma and has separated the peninsula of Baja California from mainland Mexico. The rifting process took place in two major stages; Stage I (~ 12 to ~ 6 Ma) is the orthogonal rifting (also known as a protogulf stage), where the Gulf of California started to form as a result of regional strain partitioning (Gastil *et al.*, 1975; Hausback, 1984; Stock and Hodges, 1989; Smith, 1991;

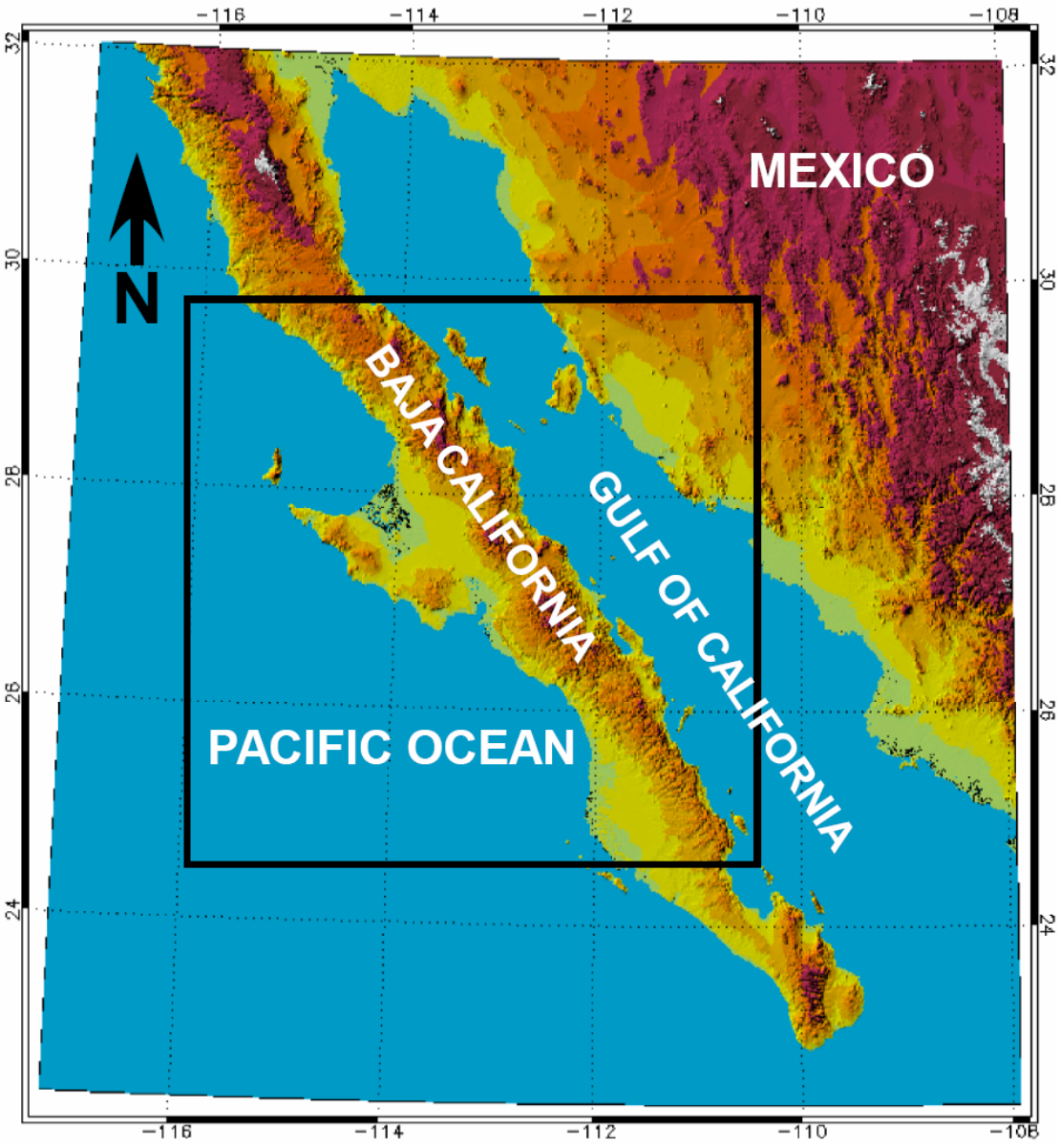

Figure 4.2. Shaded relief map illustrates the location of the study area.

Umhoefer *et al.*, 2002). Stage II, which overprinted stage I, started between ~ 8 and ~ 6 Ma. In Stage II, the San Andreas fault system and the shifted plate boundary linked to form a modern oblique-divergent plate boundary (Karig and Jensky, 1972; Stock and Hodges, 1989), followed by the initiation of the strike-slip faults and pull-apart basins in the deep-seated Gulf of California and ending with the Baja California peninsula as a separate microplate (McClay and Ellis, 1987; Lonsdale, 1989; Humphreys and Weldon, 1991; Lyle and Ness, 1991; Atwater and Stock, 1998; Umhoefer *et al.*, 2002).

IV.3. Material and methods

IV.3.1. Drainage basins geomorphometrics

Many studies have shown that where the distribution and nature of active structures are not well known, analysis of topography, digital elevation models (DEMs) usually provide important first-order insights about the rates and spatial distribution of any possible tectonic activities, because topography represents the net product of the interaction among tectonic, climate and surficial processes (e.g., Ahnert, 1970; Smith and Bretherton, 1972; Dunne, 1980; Willgoose *et al.*, 1991a, b; Dietrich *et al.*, 1993; Ohmori, 1993; Granger *et al.*, 1996; Hurtrez and Lucazeau, 1999; Kirby and Whipple, 2001; Finlayson *et al.*, 2002; Montgomery and Brandon, 2002; Kirby *et al.*, 2003). Such analysis is usually carried out on drainage basins, which are spatial units containing integrated aerial and linear pathways for sediment movement. A drainage basin is defined as the logical unit within which to model the subaerial geomorphological evolution of landscape to reveal the interaction between the prevailing major

geomorphic forcing factors (Tucker and Bras, 2000). Thus, drainage developments in different tectonic regimes have been the focus of many authors for a long time (cf. Davis, 1899; Chorley, 1969; Smith and Bretherton, 1972; Schumm, 1977; Dunne, 1980; Chorley *et al.*, 1984; Bull and McFadden 1977, Rockwell *et al.*, 1984; Keller, 1986; Wells *et al.*, 1988; Willgoose *et al.*, 1991a, b; Dietrich *et al.*, 1993; Keller and Pinter, 1996, 2002; Tucker and Bras, 2000; Wilson and Gallant, 2000; Silva *et al.*, 2003; Martin and Church, 2004). The crucial step in this study is the drainage-basin extraction, which, depends on the resolution of the DEM. The effect of DEM resolution on measuring different geomorphic properties has been examined by many works (e.g. Strahler, 1952; Hack, 1973; Bull, 1977; Hare and Gardner, 1985; Cox, 1994; Wolock and Price, 1994; Zhang and Montgomery, 1994; Goa, 1997; Walker and Willgoose, 1999; Gelabert *et al.*, 2005). In this study, the high resolution of the ASTER DEM (15m) allows detailed extraction of the Neogene drainage basins and provides precise stream morphometrics. A continuous depressionless 15-m DEM, which has been patched using the techniques introduced by El-Sobky and Dorobek (2005) was used to define the Neogene rift basins. The D-8 algorithm (Jenson and Dominque, 1988; Costa-Cabral and Burges, 1994) and D-Infinity algorithm (Tarboton, 1997) we used provide highly automated procedures for basin extraction. Using these algorithms, the identified network channels are fully connected, convergent and unidirectional down-slope. Also, the implementation of the D-Infinity algorithm was found to be efficient and powerful, where it can assign reasonable flow directions even in very complex and ambiguous situations without user intervention. On the other hand, we used the “imposed gradients” algorithm that was

introduced by Garbrecht and Martz (1997) to resolve flow directions in flats, which eliminated virtually all parallel flow. Figure 3c illustrates all the extracted Neogene rift basins along the eastern margin of Baja California, where only thirty-four drainage basins were selected to extract the morphometric indices. These basins are bounded by the Baja peninsular divide (BPD) to the west and their main streams draining into the Gulf of California. So the morphometric parameters of these basins are basically used to reveal the long-term tectonic activities triggered first by the back arc deformation and culminated by later rifting processes. I followed Strahler's system (Strahler 1952) for the orders of the extracted streams, which are still considered as the simplest, and certainly the most widely accepted method today.

IV.3.2. Multivariate analysis

IV.3.2.1. Principal component analysis (PCA)

The extracted geometrical variables are considered as the tab record for each basin history. These variables should reveal the uniqueness of each basin in terms of their tecto-geomorphological behaviors, especially in the Neogene periods. Some of these variables are correlated to each other to some extent; others are dependent on each other, and so on. Before classifying the drainage basins into certain groups, exploring the relationship between drainage basins variables is very important. To reduce the geometrical variables and remove any redundancy in the measured variables, which usually relates to the degree of correlation between some of these variables, a reliable multivariate statistical technique must be used. The multivariate statistical technique

serves as a tool for screening of such large numbers of interrelated variables for their underlying dimensions (Ebisemiju, 1979).

Multivariate analysis has been used efficiently in the past decades in many fields of study (e.g., in hydrogeology: Güler *et al.*, 2002; Lambrakis *et al.*, 2004; Love *et al.*, 2004; Wright *et al.*, 1984; Bargos *et al.*, 1990; Norris and Georges, 1993; Wright *et al.*, 1993; in geomorphology: Mather and Doorn-Kamp, 1970; Mark, 1975; Pavoni *et al.*, 1997; Griffith, 2002; Bishop *et al.*, 2005; Smith *et al.*, 2005; in sedimentology: Qu Wenchuan, 2001; Yongming *et al.*, 2006; in geochemical assessments: Cushing *et al.* 1980, Prat *et al.* 1984, Sabater *et al.*, 1989, 1991; Del Giorgio *et al.*, 1991; Melloul and Collin, 1992; Bandy and Pardo; 1994, in environmental measurements: Cushing *et al.*, 1980; Sabater *et al.*, 1989; Melloul and Collin, 1992; van Tongeren *et al.*, 1992; Pardo, 1994; Green and Montagna, 1996; Miranda *et al.*, 1996; Pienitz *et al.*, 1997*a*, *b*; Diaz *et al.*, 2002).

In this study we used principal component analysis (PCA), which is one of the most widely used multivariate techniques. Principal components analysis, the term first introduced by Thurstone (1931), is a statistical technique applied to a number of variables to discover the degree of relative independence of these variables to one another and to identify new, meaningful, underlying variables. Also PCA is used as a tool in attempts to reduce a large set of variables to a more meaningful and in most cases smaller set of variables. Principal component analysis (PCA) usually takes place through a number of mathematical procedures that transform a number of, in most cases, correlated variables into a smaller number of uncorrelated variables called principal

components. The first principal component (usual from PC1 to PC3) accounts for as much of the variability in the data as possible, and then each succeeding component accounts for as much of the remaining variability as possible. The most important character of PCA is that generated components are thought to be representative of the underlying processes that have created the correlations among variables. Although many researchers accept these techniques and strongly recommend them for both identification of groups of interrelated variables and reduction of number of variables, others have criticized multivariate analyses for rarely giving results that go beyond common knowledge (e.g., Karr and Martin 1981, Fore *et al.* 1996, Stewart-Oaten 1996). The correlation matrix is used in this analysis because all variables are quantitative and with different units (Saporta, 1990; Lebart *et al.*, 1995).

However, PCA is sensitive to the magnitude of correlations; robust comparisons must be made to ensure the quality of the analysis. PCA is known to be scale dependent (i.e., the variability of the data can be dominated by the variables in the more sensitive units), sensitive to outliers and missing data, and subject to poor correlations between poorly distributed variables. As a result data transformations are highly recommended before running of these analyses (see Austin and Greig-Smith, 1968; Hruby, 1987; Jackson, 1993; Norris and Georges, 1993; Palmer, 1993). These transformations had a large impact on our PCA results.

Normal score transformation is used as a transformation tool to ensure a normal distribution, or “Gaussianization” (Monbet and Prevosto, 2000) of the all measured geomorphic variables before PCA transformation. Normal score transformtion is a

graphical transform that normalizes any distribution, regardless of its shape. The NST computations were done using the geostatistical Toolbox software v. 1.30. In practice, the normal score transform proceeds in three steps as summarized by Goovaerts and Jacquez (2004):

1. The N original data $z(\boldsymbol{u}_\alpha)$ (i.e. SMR data) are first ranked in ascending order. Since the normal score transform must be monotonic, ties in z-values must be broken, which has been done randomly.

2. The sample cumulative frequency of the datum $z(\boldsymbol{u}_\alpha)$ with rank k is then computed as

$$pk^* = k/N - 0.5/N \quad (1)$$

3. The normal score transform of the z-datum with rank k is matched to the quantile of the standard normal cdf:

$$y(\boldsymbol{u}_\alpha) = \varphi(z(\boldsymbol{u}_\alpha)) = G\text{-}1[F(z(\boldsymbol{u}_\alpha))] = G\text{-}1[pk^*] \quad (2)$$

IV.3.2.2. Cluster analysis

The term cluster analysis was first introduced by Tryon (1939), where he introduced a number of methods and algorithms for grouping objects (e.g. individuals, quadrats, species etc.) of similar kind into respective categories. In other words, cluster analysis is defined as an exploratory data analysis tool which aims at sorting different objects or cases into groups or clusters in a way that the degree of similarity between two objects is maximal if they belong to the same cluster and minimal otherwise (Davis, 1973). For a good introduction of cluster analysis, see Hartigan (1975), Gordon (1981), Murtagh (1985), McLachlan and Basford (1988), and Kaufman and Rousseeuw (1990).

Cluster analysis has proven useful in many aspects of geology, for example, in studies of carbonate facies and paleoclimatic changes (Smosna and Warshauer, 1979; Sheps, 2004; Goddu *et al*., 2003), in geochemistry and environmental monitoring (Grande et. al., 2000, 2003b; Zwolsman *et al.*, 1993, 1997), and in geomorphology and soil classification (Moore and Russell, 1967; Campbell *et al.*, 1970; Arkley ,1971, 1976; Aldenderfer and Blashfield, 1984; Webster and Oliver, 1990; Young and Hammer, 2000).

Cluster results can change dramatically with the choice of the clustering method, the distance measured, and the number of clusters. Moreover, depending on the selected validity measure, different answers result for the optimal number of clusters. Despite the changing cluster results, each partition can still be informative and valuable. The results can give an interesting insight into the multivariate data structure even if the validity measure does not suggest the optimum for the chosen cluster number. It is thus desirable to perform cluster analysis in an exploratory context, by changing the cluster parameters and visually inspecting the results (Templ, 2003). SPSS Software V. 14.0.2 has been selected to conduct cluster analysis, where we selected the hierarchical clustering approach, which allows users to select a definition of distance, then select a linking method for forming clusters, then determine how many clusters best suit the data. Considering establishment of the matrix distance, we chose Euclidean distance because it is the most common distance to measure inter-cluster distances, especially when merging nearest clusters into broader groups. In a very simple sense, Euclidean distance is computed as follows: If a given pair of cases is plotted on two variables, which form

the x and y axes, the Euclidean distance is the square root of the sum of the square of the x difference plus the square of the y distance. Then we used a between-group distance technique to generate the "dendrograms," are also called "hierarchical tree diagrams or plots," which are simply a sequence of clustering partitions.

IV.3.3. Drainage basin's main stream profile analysis

In a tectonically active region, the main stream profile analysis of drainage basins has strong potential to help reveal the fundamental controls on the relief structure of mountain belts. The stream profile geometry has been well and intensively studied to identify spatial patterns of rock uplift, to infer erosional processes, and to identify the interaction between the tectonic activity and prevailing fluvial processes (e.g., Seeber and Gornitz, 1983; Ouchi, 1985; Harvey and Wells, 1987; Merritts and Vincent, 1989; Cox, 1994; Kafri and Heimann, 1994; Howard, 1994; Wende, 1995; Burbank *et al.*, 1996; Bonnet *et al.*, 1998; Ginat *et al.*, 1998; Fisher and Souch, 1998; Hurtrez *et al.*, 1999; Holbrook and Schumm, 1999; Humphrey and Konrad, 2000; Mather, 2000; Stokes and Mather, 2000; Snyder *et al.*, 2000; Cox *et al.*, 2001; Hsieh and Knuepfer, 2001; Sun *et al.*, 2001; Ben-David *et al.*, 2002; Ginat *et al.*, 2002; Stokes and Mather, 2003; Duvall et. al., 2004). In active tectonic basins, the signal of rock uplift is usually transmitted through the bedrock channel, where fluvial incision controls landscape erosion by controlling the relief structure of drainage basins (Whipple and Tucker, 1999). This fact has led to numerous studies that demonstrate that analysis of the drainage basin main stream profile, either from the morphological point of view (e.g.

stream length-gradient index) or from the bedrock-incision point of view (slope-area analysis) is critical and at the same time a powerful tool to explore rates and patterns of active deformation. The integration between the ASTER DEM and SRTM DEM (El-Sobky and Dorobek, 2005) provides a highly accurate and precise DEM with a 15-m resolution, which will accurately capture the essential channel geomorphometric character to conduct the present study.

IV.3.3.1. Stream length-gradient index

The stream length-gradient index (SL) is one of the earliest-used geomorphic indices Hack, 1973). The SL index has been used as an indicator of the geomorphic evolution of active tectonic regimes because it usually expresses the connection between sensitivity to rock resistance, climatic change and tectonic processes to some extent with the production of a certain landscape in an active tectonic setting (Verrios and Kokkalas, 2004). The stream length-gradient index is defined as:

$$SL = (\Delta H/\Delta L)\, L \qquad (3)$$

where SL is the stream length gradient index, $\Delta H/\Delta L$ is the stream gradient at a specific site in the channel (ΔH is the change in elevation of the reach and ΔL is the length of the reach) and L is the total channel length from the point of interest where the index is being calculated upstream to the highest point on the channel (Hack, 1973; Merritts and Vincent, 1989; Keller and Pinter, 2001). The SL index is roughly related to the stream power but is particularly sensitive to changes in slope and lithology; this sensitivity allows evaluation of the relationship between possible tectonic activity and rock

resistance. In other words, the values of the SL index are high in areas where the rocks are significantly resistant or where active deformation is present (Zygouri and Kokkalas, 2004; Zovoili and Koukouvelas, 2004). Therefore, any anomalously high SL values or fluctuation of the SL values in rock of uniform resistance is a possible indicator of active tectonics (Bull and McFadden, 1977; Keller, 1986; Keller and Pinter, 1996; Azor and Keller, 1999). In our study, we used stream length-gradient (SL) indices, which normalize the channel slope to basin size, to provide a means to quantitatively compare channel slope between basins.

IV.3.3.2. Slope area analysis

The relation between the main stream slope and the area of drainage basins is widely used to assess the balance between the rock uplift and channel incision in any tectonically active regimes (Snyder *et al.*, 2000; Kirby and Whipple, 2001; Kirby *et al.*, 2003; Duvall *et al.*, 2004; Kobor and Roering, 2004). This tectonic balance is demonstrated by using the stream power (also known as shear stress) model (Howard and Kerby, 1983), which express the relation between bedrock channel incisions as a power law function of unit stream power. In other words, this relation is expressed in terms of drainage area (A) and local channel slope (S) as follows:

$$S = K_s A^{-\Theta} \qquad (4)$$

with k_s often referred to as the steepness index, and the exponent Θ as the concavity index, which can be measured directly by regression of slope and area data. This relation has been applied at different tectonic settings (e. g., Howard and Kerby, 1983; Seidl and

Dietrich, 1992; Sklar and Dietrich, 1998; Whipple and Tucker, 1999; Stock and Montgomery, 1999; Snyder *et al.*, 2000; Whipple *et al.*, 2000a; Kirby and Whipple, 2001; Montgomery, 2001; Schorghofer and Rothman, 2001; Roe *et al.*, 2002; Dietrich *et al.*, 2003; Kobor and Roering, 2004). The equation above is applied as a first-order exploratory tool to reveal possible active tectonics in unexplored settings with the assumption that minimal changes in slope-area data may reflect variable sediment supply, localized debris flow erosion, the frequency of storm events, or orographic effects (Kobor and Roering, 2004). The results of the power-law regression analysis produce a highly scattered cloud of points that needs to be smoothed (Tarboton *et al.*, 1991; Montgomery and Foufoula-Georgiou, 1993; Tucker and Bras, 1998; Snyder *et al.*, 2000, Duvall *et al.*, 2004). A Matlab code (Appendix 1) used in our study simply averaged slopes in logarithmic bins of the drainage area to remove the scattered clouds and end with a more interpretable and smooth figure ready for computation of local slopes.

Rock-type changes along the mainstream profile reflect possible competency changes that are vital to evaluate the bedrock incision rates (Hack, 1957; Stock and Montgomery, 1999; Whipple *et al.*, 2000a, 2000b; Sklar and Dietrich, 2001; Duvall *et al.*, 2004). Matching the drainage basin main stream profile with the object-oriented classification image using the technique introduced by El-Sobky and Dorobek (2006), provides good insight into the possibility of any competency changes caused by down-slope bedrock variation.

IV.4. Results and discussion

IV.4.1. Tectono-geomorphometrics and multivariate analysis

The merging of the ASTER DEM with the manipulated (geostatistically patched, El-Sobky and Dorobek, 2005, 2006) SRTM DEM provided a highly accurate, spike-free DEM. The generated DEM (15m) was used successfully to extract the drainage basins for the entire Baja California peninsula (Figure 4.3) using the D-8 algorithm (explained earlier in detail). However, only thirty-four drainage basins were selected, using the most common morphometric parameters, for investigating their sensitivities to any possible variations along two-thirds of the eastern part of the peninsula. These basins were selected by their main-stream profiles, starting from the peninsular divide as an input and reaching the Gulf of California western coast (eastern coast of Baja) as their reach points. So these basins and their main stream profiles record any possible variation that may be related to tectonic, climatic or lithologic, or combinations of these geomorphic forces that might have happened in the course of their ages. These records of variations are best estimated from the basin's morphometric parameters. Thirty parameters or variables of drainage-basin morphometry were selected to conduct our study (Table 4.1). Our first aim in this part of study was to classify the thirty-four drainage basins into certain groups, in which basins belonging to the same group reflect similarity and dissimilarity when compared to the other groups. Implementing this approach using these thirty morphometric parameters is impractical without using statistical power as an aid to guide the classification. The reason, basically, is that these parameters have different units and these units are expected to

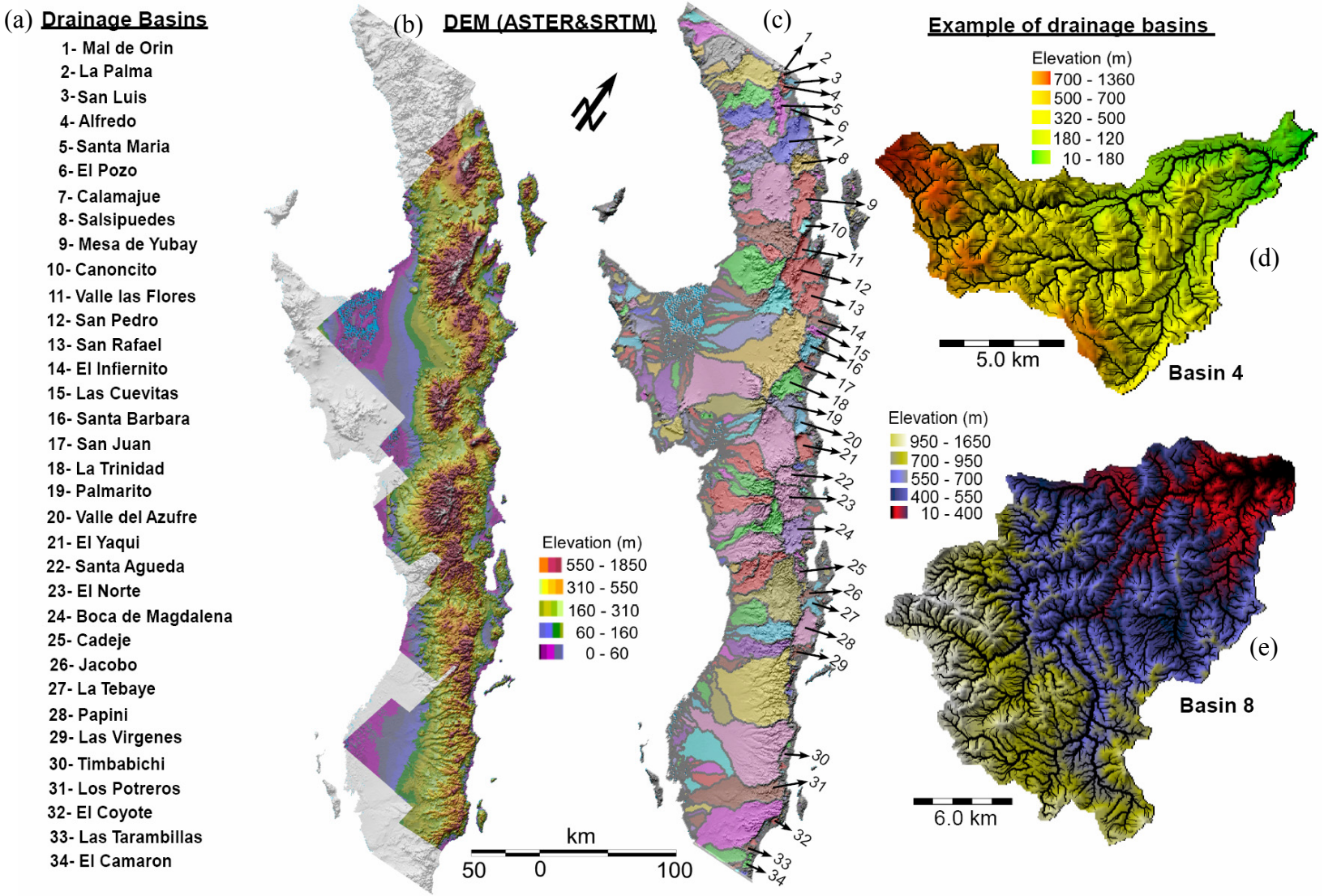

Figure 4.3. (a) The thirty-four extracted drainage basins form the 15-m DEM as illustrated in (b). (c) Locations of the selected basins. (d & e) Two examples for the extracted drainage basins.

Table 4.1. Morphometric Parameters (A is Area; DD is Drainage Density; TNS is Total Stream No.; EF is Elongation Factor; SO is Strahler Order; LCD is Longest Channel Length; TCL is Total Channel Length; HA is Hypsometric Area; HI is Hypsometric Integral; ME is Max. Elevation; MeE is Mean Elevation; ASLS is Ave. Straight-Line Slope; AACS is Ave. Along-Channel Slope; BR is Basin Relief; OE is Outlet Elevation).

Basins	A	DD	TSN	EF	SO	LCL	TCL	HA	HI	ME	MeE	ASLS	AACS	BR	OE
B1	54.31	13.57	3775	0.41	6	23.67	736.95	55.73	0.54	1160	627.69	0.05	0.04	1.12	43
B2	47.96	13.67	3070	0.64	6	19.77	655.53	49.20	0.41	1342	557.62	0.03	0.02	1.33	18
B3	86.48	13.46	6143	0.67	7	21.30	1163.57	88.69	0.19	831	156.82	0.00	0.00	0.83	5
B4	122.53	13.54	7790	0.50	7	28.47	1658.86	125.60	0.45	1360	431.10	0.01	0.01	1.35	10
B5	451.60	13.61	29200	0.48	8	54.82	6144.05	462.08	0.35	1427	579.14	0.01	0.01	1.43	7
B6	75.54	13.52	4989	0.63	7	21.20	1021.46	77.34	0.25	833	211.22	0.01	0.01	0.83	5
B7	903.66	13.44	59757	0.57	8	71.95	12143.15	923.25	0.46	1645	479.21	0.01	0.01	1.64	4
B8	398.12	13.48	25102	0.64	8	49.01	5365.65	398.14	0.52	1655	649.61	0.02	0.01	1.65	10
B9	895.58	13.65	57912	0.56	9	76.42	12228.00	895.79	0.48	1637	454.47	0.02	0.01	1.64	2
B10	99.24	13.63	6384	0.56	6	25.58	1352.51	99.24	0.36	1641	592.63	0.05	0.03	1.63	17
B11	237.40	13.51	12759	0.58	7	32.67	3208.27	237.40	0.40	1580	533.11	0.01	0.01	1.58	4
B12	995.20	13.35	62821	0.71	9	77.11	13285.74	995.31	0.26	1666	433.87	0.01	0.00	1.66	3
B13	558.52	13.42	36599	0.67	8	54.26	7496.37	558.47	0.26	1265	334.96	0.01	0.00	1.26	1
B14	186.30	13.30	11626	0.50	7	38.97	2477.66	186.32	0.36	940	336.96	0.02	0.01	0.93	8
B15	153.57	13.32	9128	0.46	7	35.88	2045.85	153.56	0.38	920	410.75	0.03	0.02	0.91	14
B16	348.24	13.35	20845	0.53	8	41.50	4650.50	348.26	0.38	1129	432.75	0.01	0.01	1.13	2
B17	109.84	13.30	7479	0.47	7	26.38	1460.76	109.84	0.29	1249	356.98	0.02	0.01	1.25	5
B18	609.47	13.35	37126	0.66	8	54.61	8136.74	609.45	0.27	1397	378.11	0.01	0.01	1.39	4
B19	442.72	13.44	26545	0.40	8	61.74	5951.66	442.71	0.38	1385	417.83	0.01	0.01	1.38	3
B20	253.00	13.50	15533	0.60	7	31.89	3414.60	253.01	0.20	1922	377.69	0.02	0.01	1.92	3
B21	373.67	13.37	24228	0.43	8	54.19	4995.93	373.67	0.34	1916	461.81	0.02	0.01	1.91	5
B22	401.07	13.37	25017	0.45	8	53.15	5361.84	400.99	0.29	1600	462.64	0.01	0.01	1.60	4
B23	749.36	13.36	46244	0.62	9	78.80	10012.73	749.44	0.32	1715	549.57	0.01	0.01	1.71	3
B24	670.44	13.30	43862	0.73	8	53.46	8916.18	670.49	0.21	1289	270.28	0.00	0.00	1.28	7
B25	141.61	13.45	8144	0.53	7	29.11	1905.17	141.60	0.39	966	379.05	0.02	0.01	0.97	5
B26	152.67	13.23	10425	0.40	7	36.34	2019.45	152.67	0.35	902	222.54	0.01	0.01	0.90	6
B27	191.42	13.21	13822	0.52	7	32.54	2528.38	191.43	0.18	911	167.67	0.01	0.01	0.91	8
B28	587.17	13.25	41434	0.88	8	41.26	7782.06	587.19	0.13	1609	213.91	0.00	0.00	1.61	3
B29	114.22	13.24	8147	0.59	7	24.64	1512.57	114.23	0.48	1036	295.75	0.01	0.01	1.03	6
B30	84.05	13.17	5701	0.66	7	18.76	1107.02	84.04	0.24	849	202.52	0.01	0.01	0.85	1
B31	1544.26	13.20	113313	0.34	8	132.38	20377.34	1544.03	0.22	961	216.61	0.00	0.00	0.96	2
B32	55.12	13.07	3508	0.70	6	19.00	720.53	55.12	0.47	1046	281.87	0.01	0.01	1.05	8
B33	84.42	13.18	6008	0.42	7	26.28	1112.41	84.42	0.46	552	253.78	0.01	0.01	0.54	14
B34	69.56	13.20	4812	0.72	7	18.06	918.37	69.56	0.48	545	260.38	0.03	0.02	0.53	16

Table 4.1. Continued.

Basins	Si	BL	TFL	FD	AS	RD	RS	RSi	BiR	SF	FF	DT	RR	RHO	ASLR
B1	1.37	20.2	15.3	0.28	57.5	881	0.04	1.44	4.9	69.51	0.13	943.25	0.06	0.74	3.62
B2	1.21	12.2	11.7	0.24	31	1106	0.08	1.27	4.6	64.01	0.32	874.86	0.11	0.82	3.78
B3	1.30	15.6	27	0.31	33.3	594	0.03	1.51	4.3	71.04	0.36	955.85	0.05	0.86	3.68
B4	1.25	25	32.4	0.26	60	838	0.03	1.44	4.6	63.58	0.20	860.70	0.05	0.83	3.80
B5	1.25	50.1	105.3	0.23	36	1197	0.04	1.49	3.7	64.66	0.18	879.70	0.03	0.49	1.80
B6	1.29	15.6	11.7	0.15	40	522	0.03	1.28	4	66.04	0.31	892.98	0.05	0.39	1.56
B7	1.28	60	136.8	0.15	42.5	1225	0.02	1.37	4.7	66.13	0.25	888.61	0.03	0.77	3.64
B8	1.31	35	87.75	0.22	71	1326	0.03	1.54	4.4	63.05	0.32	849.78	0.05	0.75	3.28
B9	1.36	60.5	113.4	0.13	59.4	1236	0.02	1.73	4.3	64.66	0.24	882.90	0.03	0.76	3.25
B10	1.48	20.2	27	0.27	62	1490	0.07	1.79	4	64.33	0.24	876.67	0.08	1.01	4.04
B11	1.17	30	48.15	0.20	34	988	0.03	1.31	5.7	53.75	0.26	726.33	0.05	0.65	3.68
B12	1.35	50	156.6	0.16	47	1051	0.02	1.77	4.8	63.12	0.40	842.70	0.03	0.68	3.26
B13	1.36	40	99	0.18	46	1101	0.02	1.60	4	65.53	0.35	879.53	0.03	0.89	3.57
B14	1.28	30.8	30.6	0.16	44	762	0.02	1.37	4.4	62.40	0.20	829.94	0.03	0.97	4.25
B15	1.48	30.3	25.2	0.16	46	807	0.02	0.02	4.7	59.44	0.17	791.87	0.03	0.77	3.63
B16	1.67	40	72.9	0.21	43	1053	0.03	2.04	4.5	59.86	0.22	799.34	0.03	0.78	3.53
B17	1.25	25	9	0.08	40	1095	0.04	1.27	4.2	68.09	0.18	905.52	0.05	0.85	3.55
B18	1.61	42	91.35	0.15	43	994	0.02	1.59	4.5	60.92	0.35	813.26	0.03	0.82	3.70
B19	1.78	60.1	30.6	0.07	57	1224	0.02	1.61	4.4	59.96	0.12	806.04	0.02	0.77	3.39
B20	1.40	30.1	39.6	0.16	52	1836	0.06	1.45	4.2	61.40	0.28	828.64	0.06	0.86	3.63
B21	1.56	50.25	55.8	0.15	53	1815	0.04	1.76	4.3	64.84	0.15	866.87	0.04	0.74	3.20
B22	1.33	50.1	62.1	0.15	54	1399	0.03	1.35	4.2	62.38	0.16	833.90	0.03	0.81	3.40
B23	1.28	50	132.3	0.18	58	1210	0.02	1.82	4.5	61.71	0.30	824.57	0.03	0.80	3.60
B24	1.60	40	103.5	0.15	40	800	0.02	1.55	4.6	65.42	0.42	870.06	0.03	0.80	3.70
B25	1.25	25.2	53.1	0.37	50	820	0.03	1.31	4.5	57.51	0.22	773.75	0.04	0.89	4.00
B26	1.33	35	1602	10.49	37	676	0.02	1.39	4.7	68.28	0.12	903.19	0.03	0.73	3.45
B27	1.32	30.1	14.4	0.08	41	584	0.02	1.43	5.2	72.21	0.21	953.74	0.03	0.77	4.00
B28	1.29	30.9	47.7	0.08	31	778	0.02	1.45	4.8	70.57	0.61	935.23	0.05	0.76	3.66
B29	1.21	20.5	25.2	0.22	40	523	0.03	1.27	4.6	71.33	0.27	944.60	0.05	0.72	3.30
B30	1.28	15.6	32.4	0.39	54	277	0.02	1.27	4.4	67.83	0.35	893.44	0.05	0.72	3.18
B31	1.47	130	70.8	0.05	46	676	0.01	1.48	5.2	73.38	0.09	968.25	0.01	0.35	1.84
B32	1.30	12	12.6	0.23	31	697	0.04	1.50	5	63.64	0.38	831.97	0.09	0.74	3.68
B33	1.51	24.9	25.2	0.30	47	440	0.02	1.48	4.3	71.17	0.14	937.81	0.02	0.79	3.40
B34	1.59	13	16.2	0.23	32	482	0.03	1.43	4.3	69.18	0.41	913.42	0.04	0.79	3.40

Note: Si is Sinuosity; BL is Basin Length; TFL is Total Fracture Length; FD is Fracture Density; AS is Asymmetry Factor; RD is Reach Drop, RS is Reach Slope; RSi is Reach Sinuosity; BiR is Bifurcation Ratio; SF is Stream Frequency; FF is Form Factor; DT is Drainage Texture; RR is Relief Ratio; RHO is RHO Coefficient; ASLR is Ave. Stream-Length Ratio.

have different effects on the classification process. For example, the drainage-basin area ranges from ~ 47 to 1544 km^2 while the hypsometric integral ranges from 0.13 to 0.54. Without transforming the data, drainage area as a parameter would completely mask the hypsometric integral in the classification process. The morphometric parameters were transformed using NST to ensure normality in their distribution as well as to remove any bias from the differences in units (Table 4.2). Figure 4.4 shows the transformations of the drainage basin area, as an example, using the normal score transform. We applied the PCA with VARIMAX normalized rotation, which is an orthogonal rotation that can maximize the variances of the component loadings across variables for each component and minimize the number of variables that have high loadings on each component to simplify the interpretation process. Component loadings > 0.71 are typically regarded as excellent and < 0.32 very poor (Nowak, 1998; Garcia *et al.*, 2004). In this study, all principal factors extracted from the variables were retained with Eigen values > 1.0, as suggested by the Kaiser criterion (Kaiser, 1960).

The parametric PCA results are shown in Figure 4.5, where the thirty intercorrelated morphometric parameters were reduced into a smaller set of five orthogonal (completely uncorrelated) variables called PCs, which accounted for 80.77% of the total variance in the data set (Table 4.3 and 4.4) . These five PCs are extracted in decreasing order of variance, such that the first few principal components (PCs) explain most of the variation in the data set (Figure 4.5). The contribution of each morphometric variable to the new PC is called a load (Table 4.5). Typically, the new PC loads can be interpreted to indicate structure in the data set. The sign of variable loads (negative or

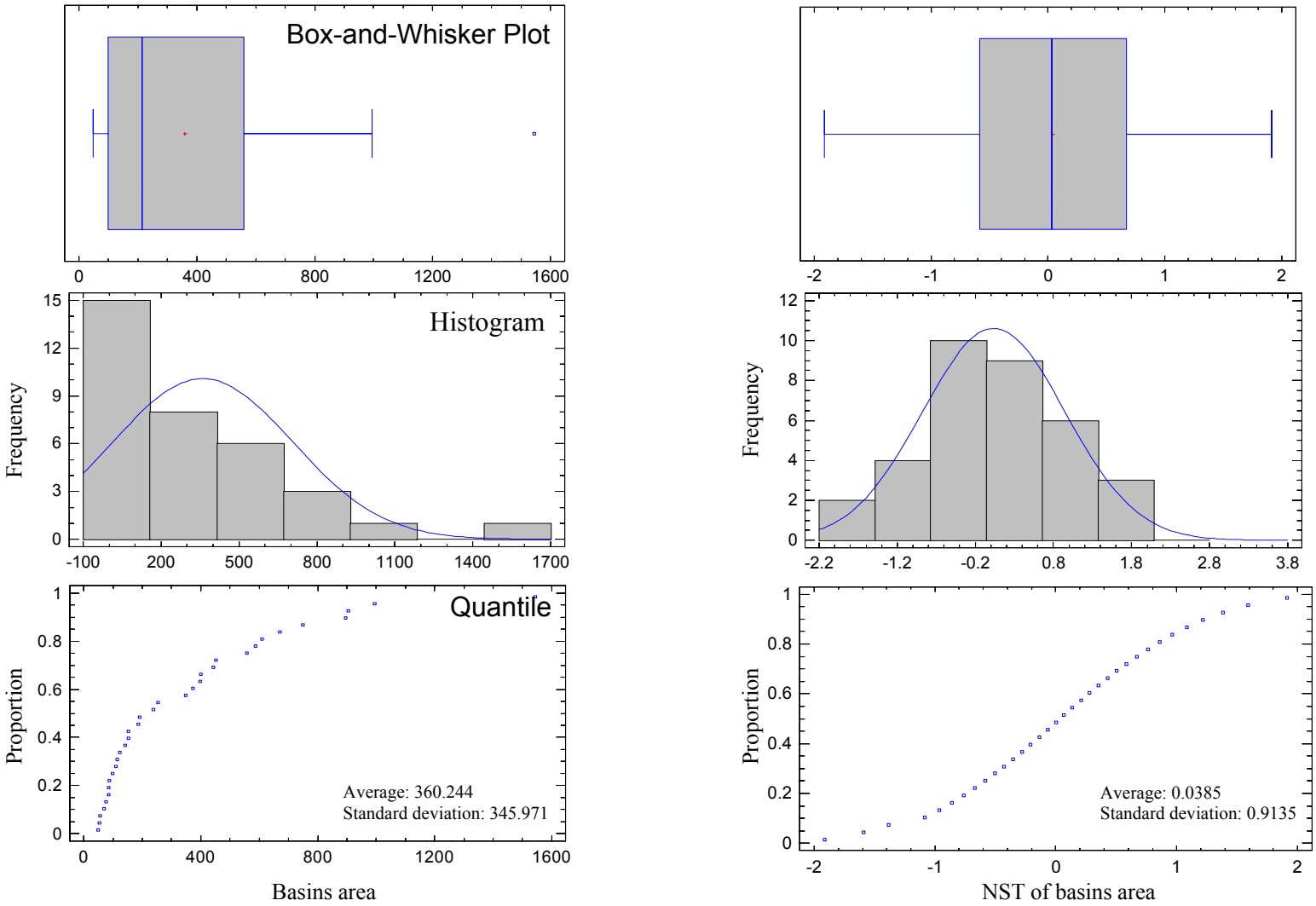

Figure 4.4. The drainage basin area parameter transformation using Normal Score Transform (NST) as an example for the transformation that has been done to all measured morphometric parameters.

Table 4.2. NST Morphometric Parameters (A is Area; DD is Drainage Density; TNS is Total Stream No.; EF is Elongation Factor; SO is Strahler Order; LCD is Longest Channel Length; TCL is Total Channel Length; HA is Hypsometric Area; HI is Hypsometric Integral; ME is Max. Elevation; MeE is Mean Elevation; ASLS is Ave. Straight-Line Slope; AACS is Ave. Along-Channel Slope; BR is Basin Relief; OE is Outlet Elevation).

Basins	A	DD	TSN	EF	SO	LCL	TCL	HA	HI	ME	MeE	ASLS	AACS	BR	OE
B1	-1.59	1.07	-1.37	-1.22	-1.92	-0.76	-1.38	-1.38	1.92	-0.14	1.59	1.92	1.92	-0.21	1.92
B2	-1.92	1.90	-1.90	0.43	-1.59	-1.08	-1.92	-1.92	0.51	0.14	1.08	1.08	1.38	0.14	1.59
B3	-0.67	0.48	-0.74	0.86	-0.86	-0.86	-0.67	-0.67	-1.38	-1.22	-1.92	-1.59	-1.59	-1.22	-0.14
B4	-0.35	0.95	-0.48	-0.51	-1.08	-0.35	-0.35	-0.35	0.59	0.21	0.28	0.14	0.21	0.21	0.76
B5	0.59	1.20	0.56	-0.59	1.22	0.86	0.59	0.59	-0.14	0.43	1.22	0.28	0.35	0.43	0.35
B6	-0.97	0.84	-1.07	0.35	-0.97	-0.97	-0.97	-0.97	-0.76	-1.08	-1.22	-0.28	-0.14	-1.08	-0.21
B7	1.38	0.25	1.37	0.00	0.86	1.08	1.22	1.38	0.76	0.97	0.76	-0.35	-0.28	0.97	-0.43
B8	0.35	0.56	0.40	0.51	0.97	0.35	0.43	0.35	1.59	1.08	1.92	0.59	0.59	1.08	0.67
B9	1.22	1.58	1.20	-0.07	1.59	1.22	1.38	1.22	1.22	0.76	0.51	0.67	0.76	0.86	-1.22
B10	-0.59	1.37	-0.65	-0.14	-1.38	-0.59	-0.59	-0.59	0.07	0.86	1.38	1.59	1.59	0.76	1.38
B11	0.07	0.74	-0.04	0.07	-0.51	-0.07	0.07	0.07	0.43	0.51	0.86	-0.21	0.14	0.51	-0.51
B12	1.59	-0.25	1.58	1.08	1.38	1.38	1.59	1.59	-0.67	1.22	0.43	-0.97	-0.97	1.22	-0.67
B13	0.67	0.18	0.65	0.76	0.67	0.67	0.67	0.67	-0.59	0.00	-0.28	-1.08	-1.08	0.00	-1.59
B14	-0.07	-0.40	-0.11	-0.43	-0.28	0.14	-0.07	-0.07	0.00	-0.59	-0.21	0.43	0.51	-0.59	0.43
B15	-0.14	-0.33	-0.25	-0.76	-0.21	0.00	-0.14	-0.14	0.14	-0.67	0.14	0.97	1.22	-0.76	0.86
B16	0.21	-0.11	0.18	-0.28	0.59	0.28	0.21	0.21	0.28	-0.21	0.35	0.07	-0.21	-0.14	-1.38
B17	-0.51	-0.56	-0.56	-0.67	-0.07	-0.43	-0.51	-0.51	-0.43	-0.07	-0.14	0.86	0.86	-0.07	-0.07
B18	0.86	-0.18	0.74	0.67	0.51	0.76	0.86	0.86	-0.51	0.35	0.00	-0.67	-0.86	0.35	-0.28
B19	0.51	0.33	0.48	-1.59	0.35	0.97	0.51	0.51	0.21	0.28	0.21	0.00	-0.51	0.28	-0.76
B20	0.14	0.65	0.11	0.21	0.14	-0.21	0.14	0.14	-1.22	1.92	-0.07	0.76	0.43	1.92	-0.59
B21	0.28	0.11	0.25	-0.97	0.21	0.59	0.28	0.28	-0.21	1.59	0.59	0.51	0.28	1.59	0.00
B22	0.43	0.04	0.33	-0.86	0.28	0.43	0.35	0.43	-0.35	0.59	0.67	-0.07	0.07	0.59	-0.35
B23	1.08	-0.04	1.07	0.28	1.92	1.59	1.08	1.08	-0.28	1.38	0.97	-0.86	-0.76	1.38	-0.97
B24	0.97	-0.48	0.95	1.59	0.43	0.51	0.97	0.97	-1.08	0.07	-0.51	-1.38	-1.38	0.07	0.28
B25	-0.28	0.40	-0.40	-0.21	0.00	-0.28	-0.28	-0.28	0.35	-0.43	0.07	0.35	0.67	-0.43	0.07
B26	-0.21	-0.84	-0.18	-1.38	-0.14	0.07	-0.21	-0.21	-0.07	-0.86	-0.86	-0.51	-0.59	-0.86	0.21
B27	0.00	-0.95	0.04	-0.35	-0.35	-0.14	0.00	0.00	-1.59	-0.76	-1.59	-0.76	-0.67	-0.67	0.59
B28	0.76	-0.65	0.84	1.92	0.76	0.21	0.76	0.76	-1.92	0.67	-1.08	-1.22	-1.22	0.67	-0.86
B29	-0.43	-0.74	-0.33	0.14	-0.59	-0.67	-0.43	-0.43	1.38	-0.35	-0.35	-0.59	-0.43	-0.35	0.14
B30	-0.86	-1.58	-0.95	0.59	0.07	-1.38	-0.86	-0.86	-0.86	-0.97	-1.38	-0.43	-0.35	-0.97	-1.92
B31	1.92	-1.20	1.90	-1.92	1.08	1.92	1.92	1.92	-0.97	-0.51	-0.97	-1.92	-1.92	-0.51	-1.08
B32	-1.38	-1.90	-1.58	0.97	-1.22	-1.22	-1.59	-1.59	0.86	-0.28	-0.43	-0.14	0.00	-0.28	0.51
B33	-0.76	-1.37	-0.84	-1.08	-0.43	-0.51	-0.76	-0.76	0.67	-1.38	-0.76	0.21	-0.07	-1.38	0.97
B34	-1.08	-1.07	-1.20	1.38	-0.67	-1.59	-1.08	-1.08	1.08	-1.92	-0.59	1.38	1.08	-1.59	1.22

Table 4.2. Continued.

Basins	Si	BL	TFL	FD	AS	RD	RS	RSi	BiR	SF	FF	DT	RR	RHO	ASLR
B1	0.35	-0.76	-0.97	0.97	0.97	-0	0.965	-0.07	1.08	0.86	-1.22	1.08	1.08	-0.59	0.14
B2	-1.59	-1.59	-1.59	0.67	-1.59	0.506	1.915	-1.22	0.35	-0.21	0.43	-0.07	1.92	0.59	0.97
B3	-0.21	-1.08	-0.35	1.22	-0.97	-0.762	0.428	0.43	-0.76	1.08	0.86	1.59	0.67	0.97	0.67
B4	-0.97	-0.35	-0.14	0.76	1.38	-0.069	0.587	-0.14	0.28	-0.35	-0.51	-0.28	0.86	0.76	1.08
B5	-0.86	0.97	0.97	0.59	-0.76	0.587	0.859	0.28	-1.92	-0.07	-0.59	0.14	-0.76	-1.38	-1.59
B6	-0.43	-0.97	-1.38	-0.43	-0.59	-1.083	0.28	-0.97	-1.22	0.28	0.35	0.35	0.76	-1.59	-1.92
B7	-0.76	1.22	1.38	-0.67	-0.21	0.859	-0.353	-0.51	0.67	0.35	0.00	0.28	-0.97	0.00	0.35
B8	-0.14	0.21	0.59	0.21	1.92	1.083	0.506	0.51	-0.21	-0.51	0.51	-0.35	0.28	-0.43	-0.76
B9	0.28	1.59	1.08	-0.97	1.22	0.965	-1.382	0.97	-0.67	0.00	-0.07	0.21	-1.08	-0.35	-0.97
B10	0.67	-0.67	-0.43	0.86	1.59	1.382	1.593	1.38	-1.59	-0.14	-0.14	0.00	1.38	1.92	1.59
B11	-1.92	-0.21	0.14	0.07	-0.86	0.069	0.672	-0.86	1.92	-1.92	0.07	-1.92	0.59	-1.22	0.51
B12	0.14	0.76	1.59	-0.28	0.28	0.209	-1.593	1.22	0.97	-0.43	1.08	-0.43	-0.14	-1.08	-0.86
B13	0.21	0.51	0.76	0.00	0.14	0.428	-0.28	0.76	-1.38	0.21	0.76	0.07	-0.43	1.38	0.00
B14	-0.51	0.07	-0.28	-0.14	0.00	-0.428	-0.428	-0.59	-0.28	-0.59	-0.43	-0.67	-0.51	1.59	1.92
B15	0.59	0.00	-0.51	-0.21	0.07	-0.209	-0.138	-1.92	0.76	-1.38	-0.76	-1.38	-0.67	-0.07	0.28
B16	1.59	0.35	0.51	0.14	-0.14	0.28	-0.069	1.92	0.07	-1.22	-0.28	-1.22	-0.86	0.07	-0.14
B17	-1.08	-0.43	-1.92	-1.08	-0.35	0.353	1.083	-1.08	-0.97	0.51	-0.67	0.59	0.35	0.86	-0.07
B18	1.38	0.59	0.67	-0.76	-0.07	0.138	-0.762	0.67	0.00	-0.97	0.67	-0.97	-0.21	0.67	0.86
B19	1.92	1.38	-0.21	-1.59	0.86	0.762	-0.587	0.86	-0.14	-1.08	-1.59	-1.08	-1.38	-0.14	-0.59
B20	0.43	-0.07	0.00	-0.35	0.51	1.915	1.382	0.07	-0.86	-0.86	0.21	-0.76	1.22	1.08	0.21
B21	0.86	1.08	0.28	-0.86	0.59	1.593	0.762	1.08	-0.35	0.07	-0.97	-0.21	0.00	-0.51	-1.08
B22	0.00	0.86	0.35	-0.51	0.67	1.219	-0	-0.67	-1.08	-0.67	-0.86	-0.51	-0.35	0.51	-0.35
B23	-0.67	0.67	1.22	-0.07	1.08	0.672	-0.209	1.59	0.14	-0.76	0.28	-0.86	-0.07	0.35	0.07
B24	1.22	0.43	0.86	-0.59	-0.43	-0.28	-1.083	0.59	0.43	0.14	1.59	-0.14	-0.28	0.43	0.76
B25	-1.22	-0.28	0.21	1.38	0.43	-0.138	0.353	-0.76	0.21	-1.59	-0.21	-1.59	0.07	1.22	1.38
B26	0.07	0.28	1.92	1.92	-0.67	-0.672	-0.859	-0.43	0.59	0.59	-1.38	0.51	-1.22	-0.76	-0.21
B27	-0.07	-0.14	-1.08	-1.38	-0.28	-0.859	-0.965	-0.35	1.59	1.59	-0.35	1.38	-0.59	-0.21	1.22
B28	-0.35	0.14	0.07	-1.22	-1.38	-0.353	-0.672	0.00	0.86	0.97	1.92	0.86	0.51	-0.28	0.43
B29	-1.38	-0.59	-0.59	0.28	-0.51	-0.965	0.209	-1.38	0.51	1.38	0.14	1.22	0.43	-0.97	-0.67
B30	-0.59	-0.86	-0.07	1.59	0.76	-1.915	-0.506	-1.59	-0.07	0.43	0.59	0.43	0.97	-0.86	-1.22
B31	0.51	1.92	0.43	-1.92	0.21	-0.587	-1.915	0.21	1.38	1.92	-1.92	1.92	-1.92	-1.92	-1.38
B32	-0.28	-1.92	-1.22	0.35	-1.92	-0.506	1.219	0.35	1.22	-0.28	0.97	-0.59	1.59	-0.67	0.59
B33	0.76	-0.51	-0.67	1.08	0.35	-1.593	-1.219	0.14	-0.43	1.22	-1.08	0.97	-1.59	0.21	-0.28
B34	1.08	-1.22	-0.76	0.51	-1.08	-1.219	0.138	-0.21	-0.51	0.76	1.38	0.76	0.21	0.28	-0.43

Note: Si is Sinuosity; BL is Basin Length; TFL is Total Fracture Length; FD is Fracture Density; AS is Asymmetry Factor; RD is Reach Drop, RS is Reach Slope; RSi is Reach Sinuosity; BiR is Bifurcation Ratio; SF is Stream Frequency; FF is Form Factor; DT is Drainage Texture; RR is Relief Ratio; RHO is RHO Coefficient; ASLR is Ave. Stream-Length Ratio.

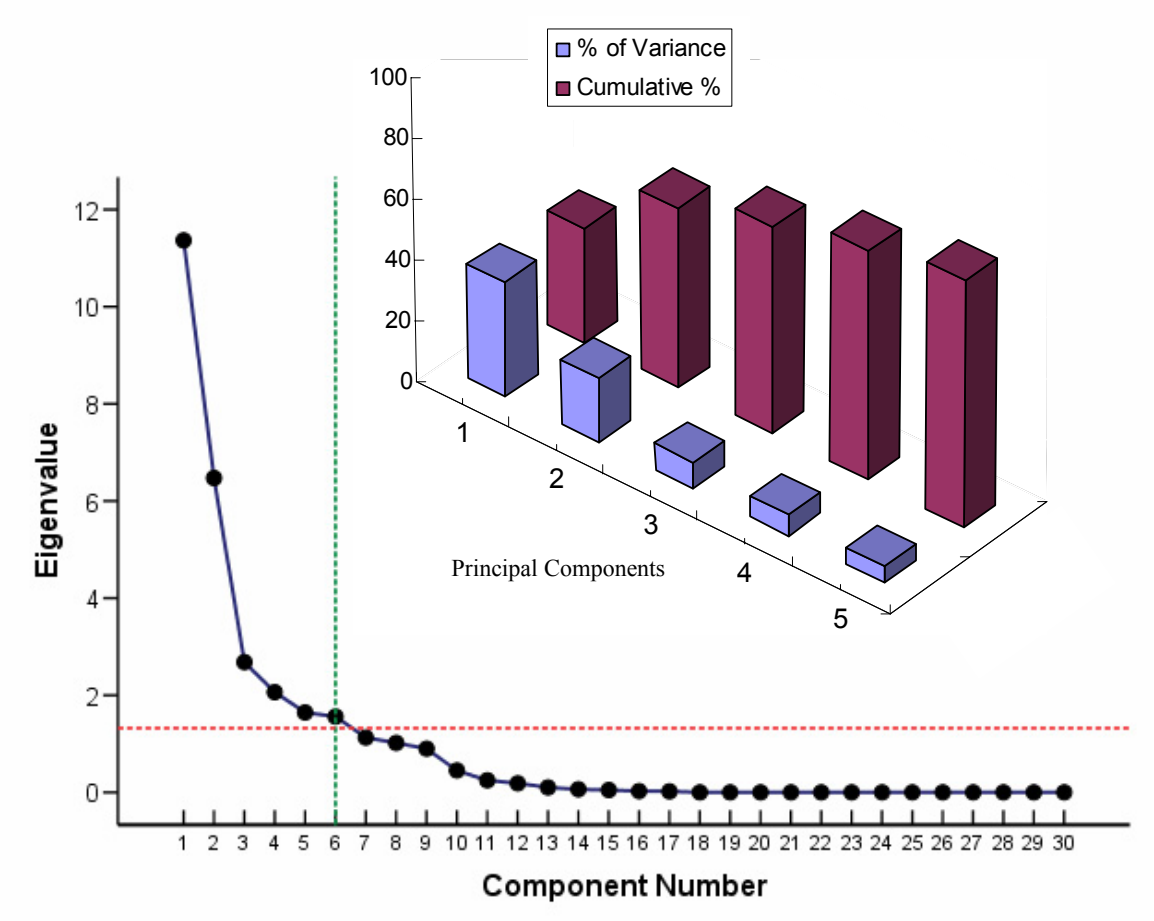

Figure 4.5. Scree plot of the thirty extracted PCs. The first five PCs which account for 80.77% of the total variance, have been selected. The Inset shows the variance and the cumulative variance of the selected first five PCs.

Table 4.3. Variance and Cumulative Variance of the Five Selected Principal Components.

% of Variance	Cumulative %
37.89	37.89
21.57	59.46
8.94	68.40
6.88	75.28
5.49	80.77

Table 4.4. The Variable Communalities for the Morphometric Parameters PCA.

Communalities

NO.	Variables	Initial	Extraction
1	Area	1	0.973
2	Drainage density	1	0.662
3	Total stream NO.	1	0.973
4	Elongation Factor	1	0.886
5	Strahler Order	1	0.886
6	Longest Channel Length	1	0.972
7	Total Channel Length	1	0.973
8	Hypsometric Area	1	0.973
9	Hypsometric Integral	1	0.626
10	Maximum Elevation	1	0.939
11	Mean Elevation	1	0.970
12	Ave. Straight-Line Slope	1	0.920
13	Ave. Along-Channel Slope	1	0.937
14	Basin Relief	1	0.952
15	Outlet Elevation	1	0.609
16	Sinuosity	1	0.817
17	Basin Length	1	0.973
18	Total Fracture Length	1	0.661
19	Fracture Density	1	0.327
20	Asymmetry Factor	1	0.332
21	Reach Drop	1	0.885
22	Reach Slope	1	0.877
23	Reach Sinuosity	1	0.843
24	Bifurcation Ratio	1	0.309
25	Stream Frequency	1	0.739
26	Form Factor	1	0.886
27	Drainage Texture	1	0.693
28	Relief Ratio	1	0.920
29	RHO Coefficient	1	0.817
30	Ave. Stream Length Ratio	1	0.903

Table 4.5. Variable Loads for the Rotated (VARIOMAX) Factors for the Morphometric Parameters PCA.

NO.	Variables (NST)	PC1	PC2	PC3	PC4	PC5
1	**Area**	0.985	0.012	0.032	-0.027	0.027
2	**Drainage density**	-0.206	0.724	-0.024	-0.259	0.164
3	**Total stream NO.**	0.985	0.019	0.019	-0.029	0.030
4	**Elongation Factor**	-0.218	0.275	0.808	0.055	-0.327
5	**Strahler Order**	0.885	0.105	-0.026	0.160	-0.257
6	**Longest Channel Length**	0.951	0.153	-0.135	-0.026	0.161
7	**Total Channel Length**	0.985	0.018	0.030	-0.022	0.022
8	**Hypsometric Area**	0.985	0.012	0.032	-0.027	0.027
9	**Hypsometric Integral**	-0.304	0.400	-0.430	0.404	-0.157
10	**Maximum Elevation**	0.557	0.776	-0.001	-0.165	0.003
11	**Mean Elevation**	0.222	0.902	-0.285	0.133	-0.095
12	**Ave. Straight-Line Slope**	-0.618	0.444	-0.383	0.371	-0.238
13	**Ave. Along-Channel Slope**	-0.639	0.533	-0.384	0.209	-0.231
14	**Basin Relief**	0.552	0.794	0.010	-0.127	-0.017
15	**Outlet Elevation**	-0.534	0.251	-0.223	0.349	0.298
16	**Sinuosity**	0.306	-0.440	0.249	0.684	-0.025
17	**Basin Length**	0.954	-0.033	-0.241	0.022	0.063
18	**Total Fracture Length**	0.772	0.058	0.142	0.193	-0.057
19	**Fracture Density**	-0.478	-0.041	0.111	0.279	-0.083
20	**Asymmetry Factor**	0.441	0.138	-0.069	0.252	-0.223
21	**Reach Drop**	0.362	0.837	-0.136	0.028	0.185
22	**Reach Slope**	-0.647	0.607	-0.133	-0.178	0.204
23	**Reach Sinuosity**	0.669	0.175	0.260	0.530	0.125
24	**Bifurcation Ratio**	0.356	0.081	0.119	-0.284	0.284
25	**Stream Frequency**	-0.138	-0.811	-0.191	0.002	0.161
26	**Form Factor**	-0.218	0.275	0.808	0.055	-0.327
27	**Drainage Texture**	-0.179	-0.773	-0.178	-0.038	0.173
28	**Relief Ratio**	-0.632	0.473	0.359	-0.390	-0.127
29	**RHO Coefficient**	-0.405	0.236	0.361	0.466	0.500
30	**Ave. Stream Length Ratio**	-0.259	0.388	0.376	0.150	0.722

positive) indicates gradients in morphometric variables. PC1 accounted for 37.89% of the total variance; had high positive loadings by drainage-basin area, total stream number, Strahler order, longest channel length, total channel length, hypsometric area and basin length; and had high negative loadings by average straight-line slope, average along-channel slope, reach slope, and relief ratio (Table 4.5, Figure 4.6a). PC1 could be interpreted as the length area component. PC2 accounted for 21.57% of the total variance and it had high positive loadings by mean elevation and reach drop, and high negative loadings by stream frequency and drainage texture (Table 4.5, Figure 4.6a). PC2 is interpreted as the elevation component. PC3 accounted for 8.94% of the total variance and it had high positive loadings by elongation factor and form factor, and moderate to low negative loadings by hypsometric integral, average straight-line slope, and average along-channel slope (Table 4.5, Figure 4.6b). PC3 is interpreted as a factor component. PC4 accounted for 6.88% of the total variance; it had moderate positive loadings by sinuosity and reach sinuosity (Table 4.5, Figure 4.6c). PC4 is interpreted as the sinuosity component. Finally, PC5 accounts for 5.49% of the total variance and had positive loading by average stream length ratio and RHO coefficient (Table 4.5, Figure 4.6d). From the PCs loading values, parameters related to area and lengths clearly played the major role and accounted for the maximum variance followed by the elevation parameters.

A cluster analysis (CA) was applied using the selected five PCs as input with Euclidian distances as the criterion for forming clusters of drainage basins. This approach is regarded as very efficient, although it tends to create small clusters. Often it

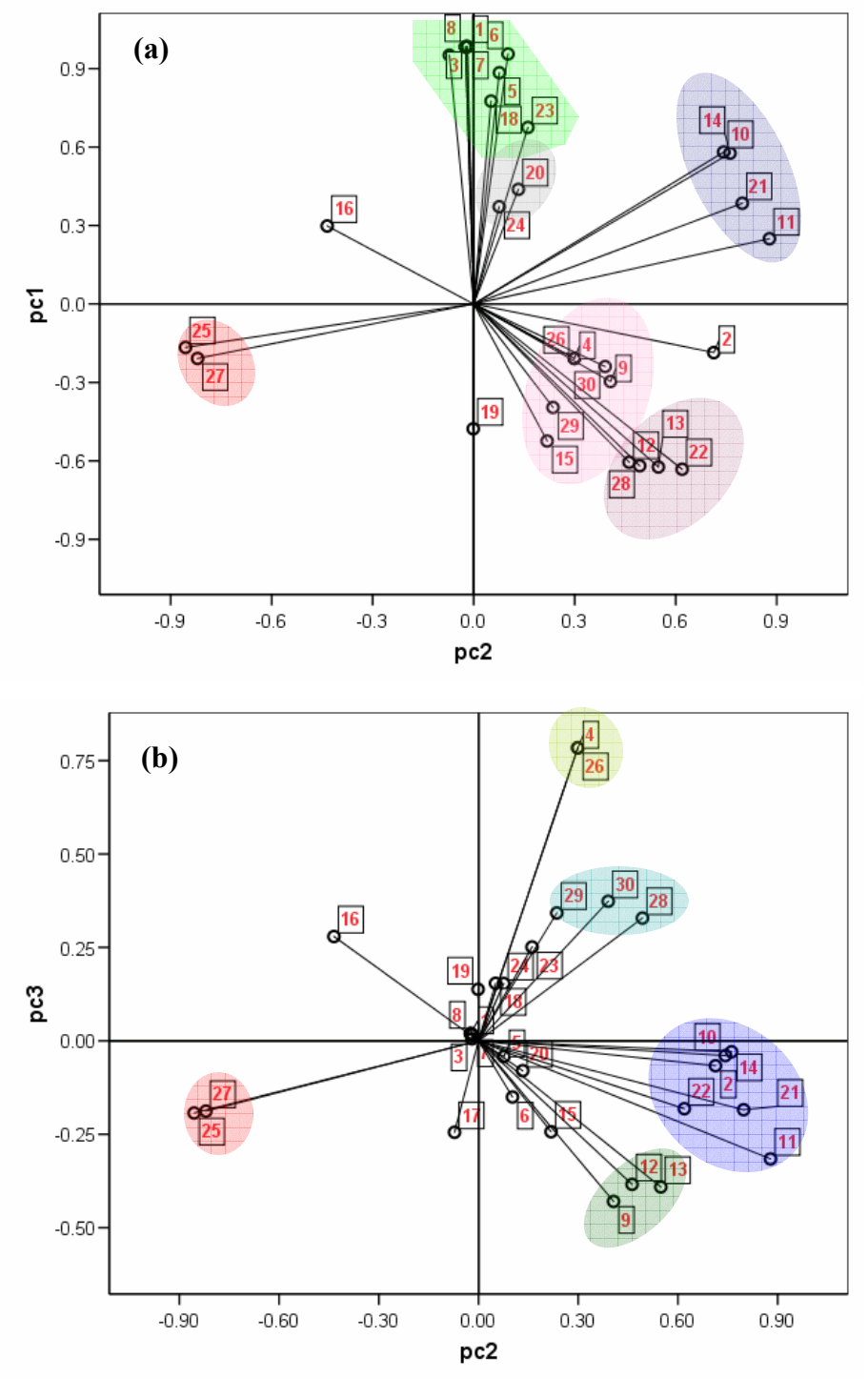

Figure 4.6. Principal components analysis of geomorphometric variables. (a) Variable loading scores for PC1 versus PC2. (b) Variable loading scores for PC2 versus PC3. (c) Variable loading scores for PC2 versus PC4. (d) Variable loading scores for PC2 versus PC5. Variables are shown in Table 4.5.

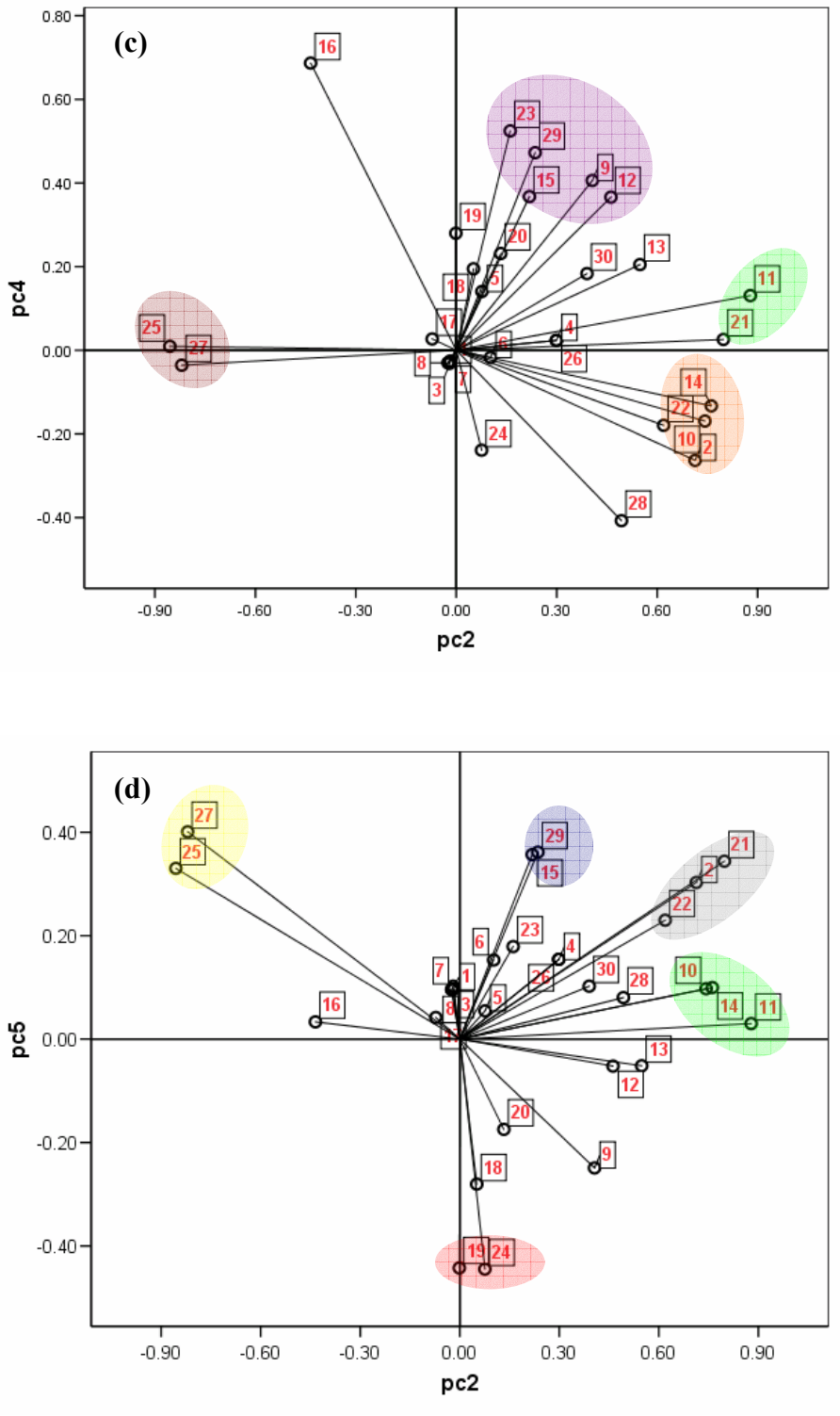

Figure 4.6. (Continued)

may appear desirable to perform cluster analysis with all geomorphometric parameters. However, the addition of only one or two irrelevant parameters can have dramatic consequences in identifying the clusters. Gordon (1999) pointed out that the inclusion of only one irrelevant variable may be enough to hide the real clustering in the data. That is why we used the first five PCs to perform this task of analysis.

Figure 4.7 displays about 9 subclusters which are connected to form four main clusters or groups at distance ~ 7 similarity units as a reference distance that reflects the degree of correlation between different basins. Group 1 is the biggest group of basins (14 basins) in the dendrogram; these basins were at least 30% similar (if we convert the degree of correlation distance into similarity distance). Group 2 comprised seven basins with a degree of similarity ~ 25%. Group 3 comprised 5 basins that have a degree of similarity almost equal to Group 1. Finally Group 4 composed of eight basins with the same degree of similarity as Group 1 and Group3. Validating the clustering results is very important to understand the relationship between the drainage basins in each group; usually, visual inspection provides a good clue. The detailed analysis of the main stream profiles of all drainage basins in the four identified groups is used as a tool to explain the clustering behavior of these basins.

IV.4.2. Response characteristics of main stream analysis

The stream length-gradient index (SL) was measured for the selected thirty-four drainage basins. Figure 4.8 illustrates the measurements procedures, where the SL index is measured at every gradient change along the profile down dip and then the average SL is calculated to be the representative value for each basin. Figure 4.9 shows the Hack

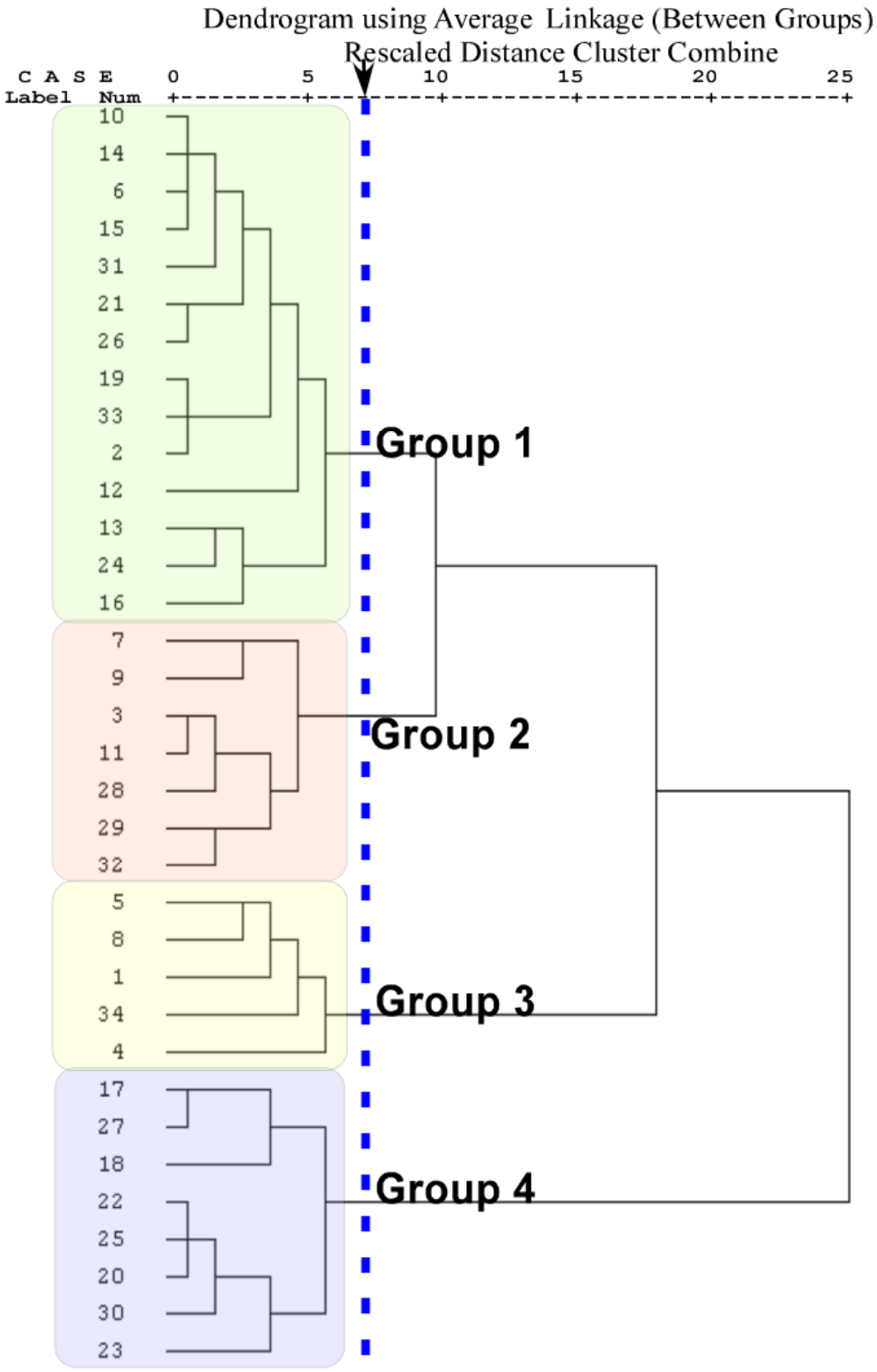

Figure 4.7. Hierarchical dendrogram for 34 drainage basins obtained by the Euclidian distances hierarchical clustering method (the distances reflect the degree of correlation between different basins).

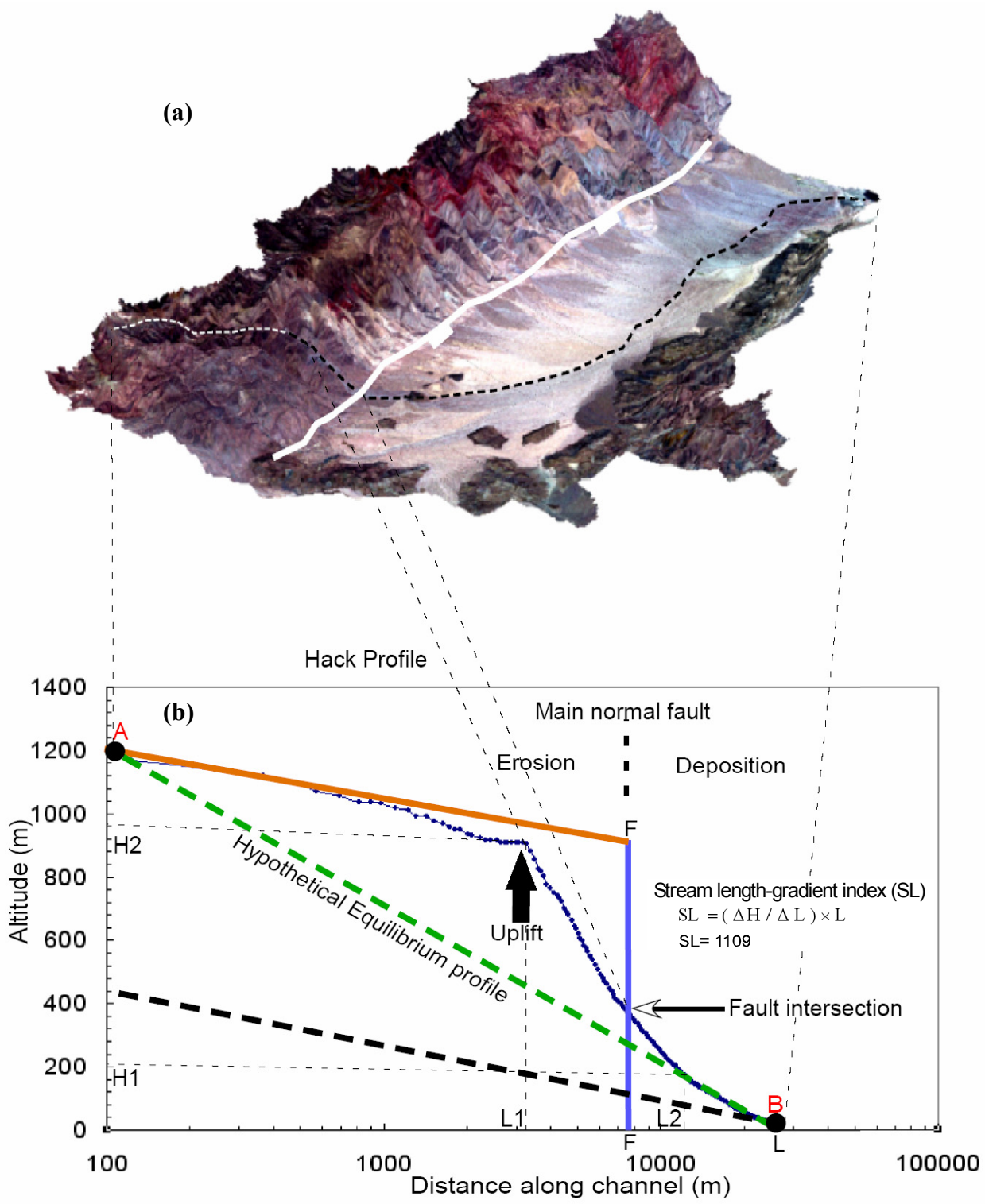

Figure 4.8. (a) 3-D image formed by draping the ETM+ scene of the Valle Las Flores drainage basin over the 15-m DEM. (b) Semilog plot of the main stream profile and the calculation of stream length-gradient index.

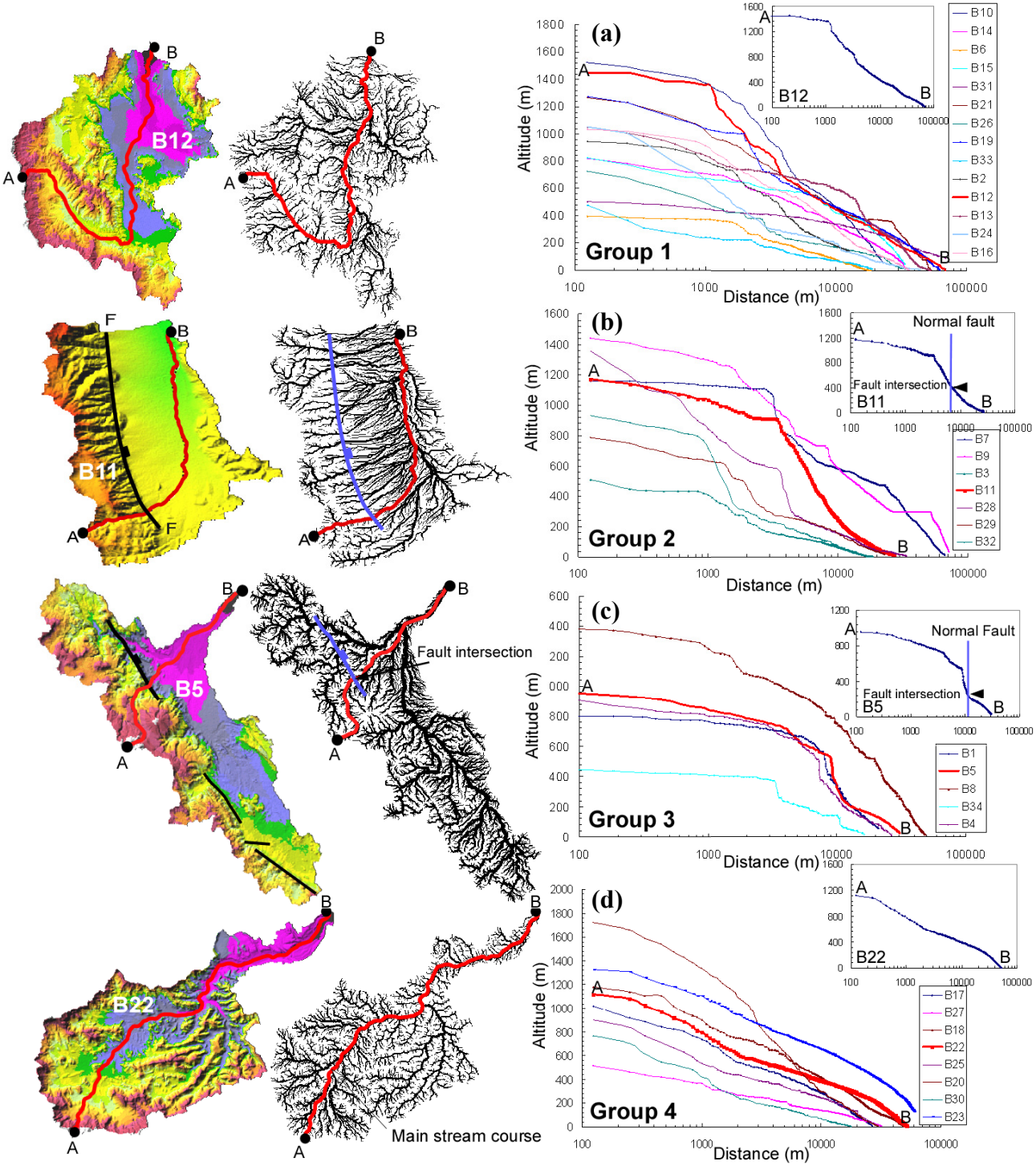

Figure 4.9. (a) Hack profiles for Group 1 basins (e.g., San Pedro basin). (b) Hack profiles for Group 2 basins (e.g., Valle Las Flores basin). (c) Hack profiles for Group 3 basins (e.g., Santa Maria basin). (d) Hack profiles for Group 4 basins (e.g., Santa Agueda basin).

profile plots for each group of basins, and Figure 4.10 illustrates the SL values for the thirty-four basins plotted as a bar diagram. The SL indices provide a very good insight for visual interpretation of the cluster analysis results, where the four main basin groups are defined. Group one, composed of 14 basins show moderate values of SL indices ranging from 550 for Basin 16 to 800 for Basin 33. In this group, Basins 2, 12, 19, 21 and 33 have slightly higher SL value than the average for this group. These five basins are located in the overlap area (Figure 4.10) between Group 1 and Group 3; their Hack profiles show a sudden gradient change down dip, which is known as a knickpoint. The knickpoints are usually interpreted either as signs of uplift movement along the bounding normal fault surfaces, or indicators of lithological variations, or combinations of differential amounts of rock uplift and eroding various rock types in these basins. Because Group 1 basins have no bounding fault scarps along their mainstream profiles, lithological variations along the mainstream profiles of these basins must be the main factor responsible for these knickpoints (e.g., Basin 12, Figure 4.11) and must control their location. Group 2 (composed of seven basins) and Group 3 (composed of five basins) show the highest SL index values within the four groups, indicating steeper relative slopes after the knickpoints along their stream long profiles. In these groups, the knickpoints are clearly matched with the presence of bounding normal fault surfaces (Figure 4.12 and 4.13), which strongly indicates differential amounts of rock uplift movement along the normal bounding fault foot wall blocks. This tectonic activity is further supported by examining the morphology of the foot wall fronts, which are characterized by steep, imbricated triangular talus facets and steep dipping faults as

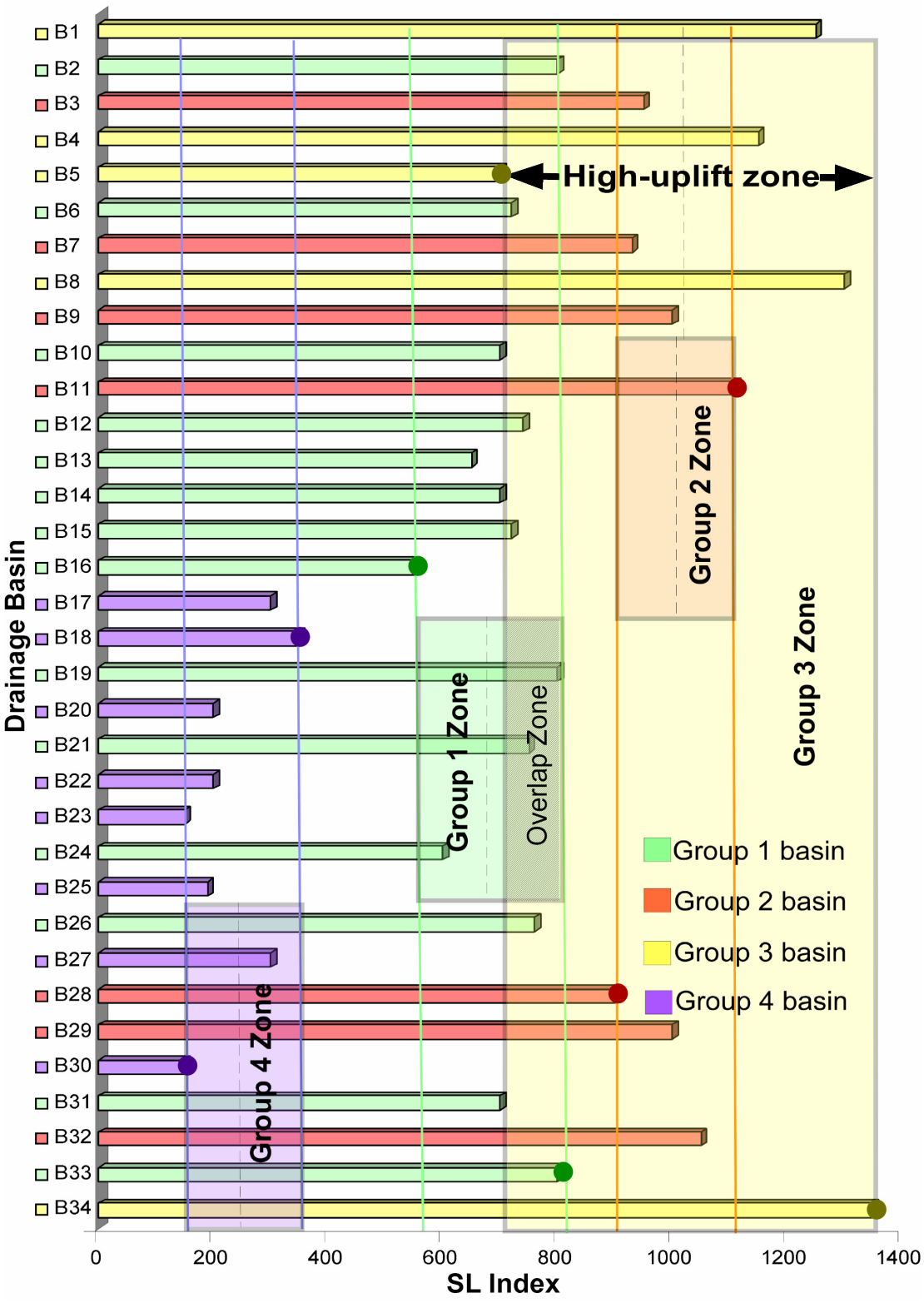

Figure 4.10. Stream length-gradient values for the thirty-four drainage basins.

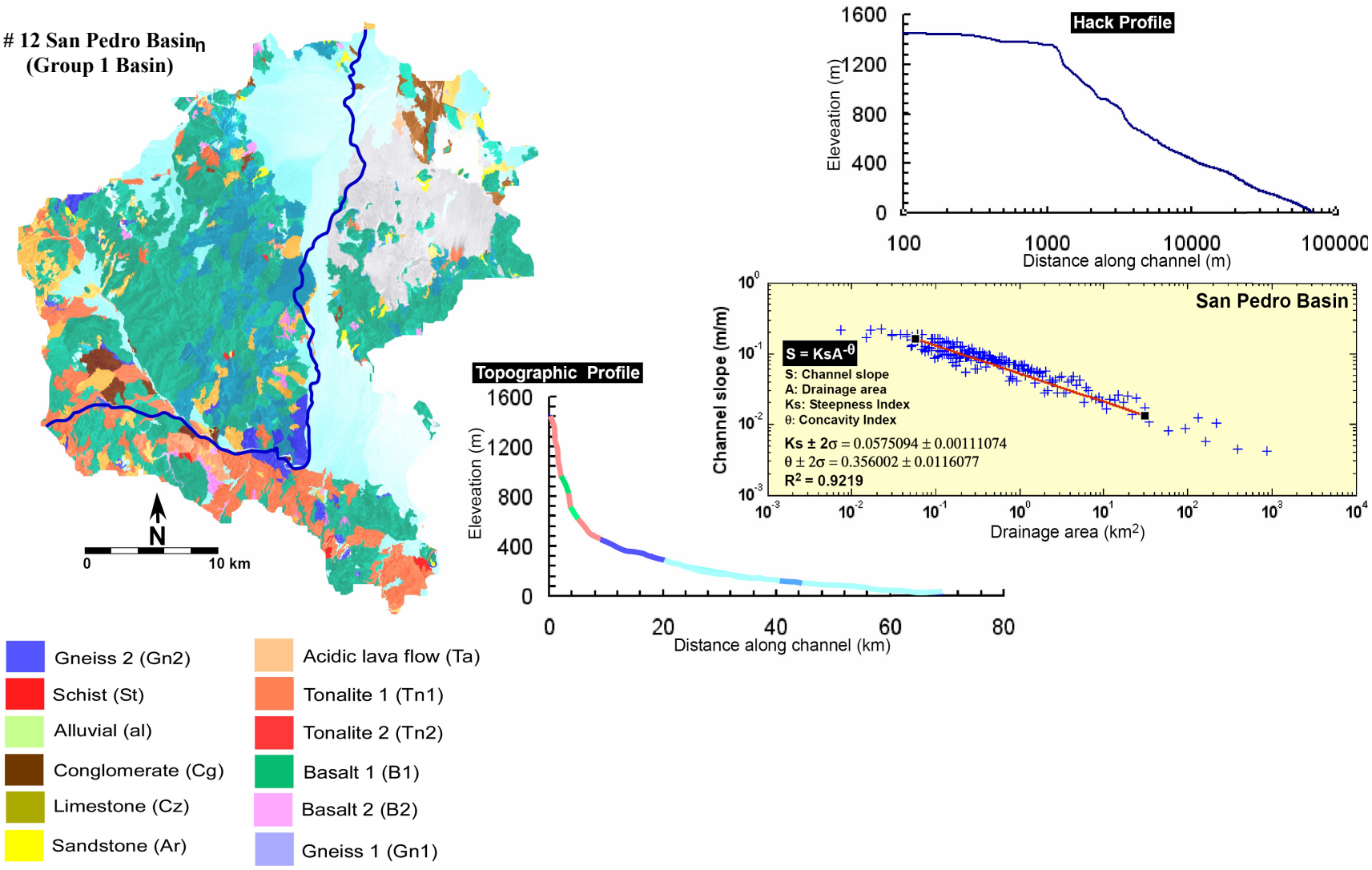

Figure 4.11. The relation between Hack profile, slope-area plot, and mainstream topographic profile in San Pedro basin. Note the knickpoint in the Hack profile and its relation to the lithological variations along the main stream topographic profile and the low k_s value. Red line in the slope-area plot is best-fit regression to the mainstream along the slope.

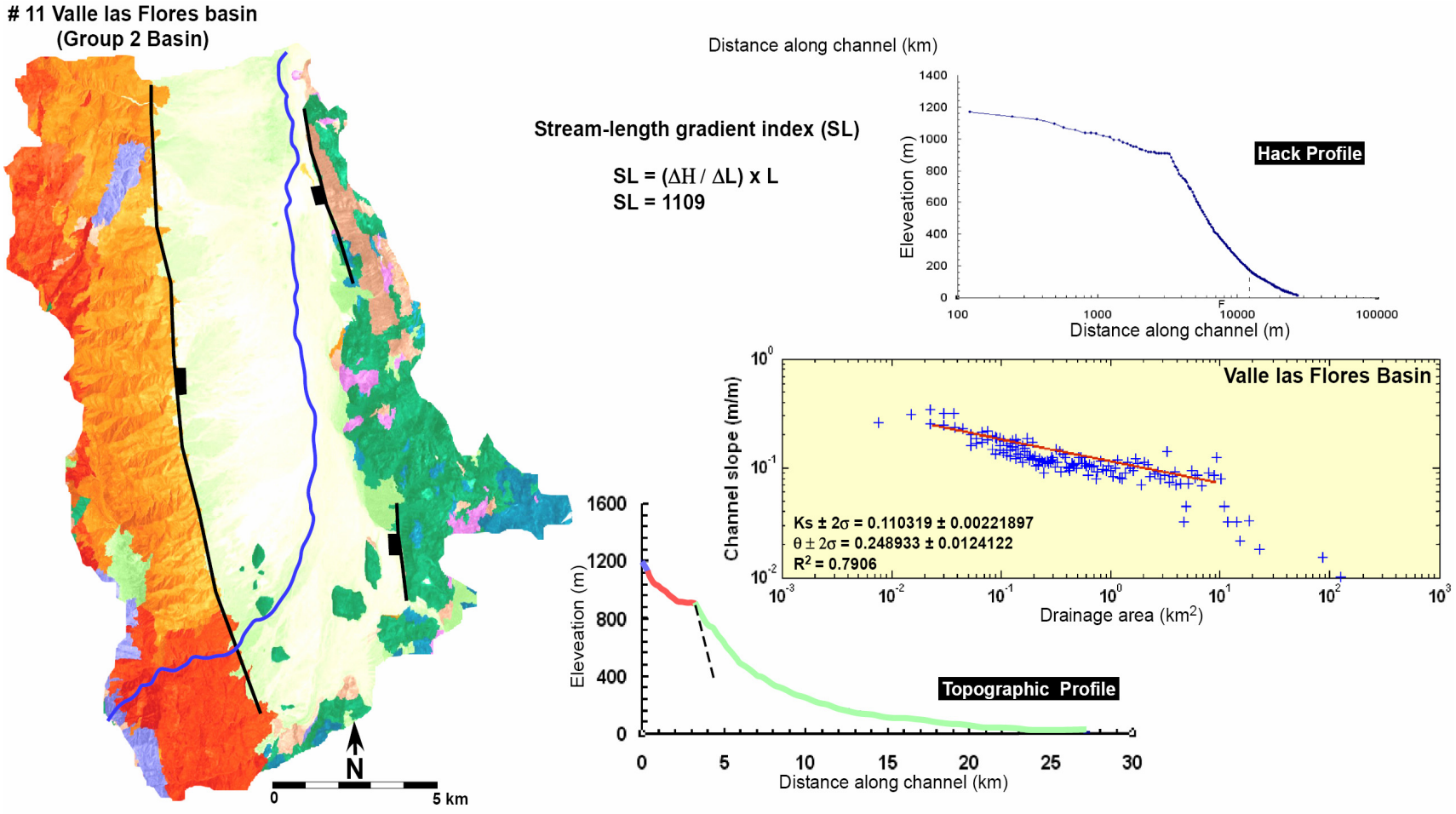

Figure 4.12. Hack profile, slope-area analysis, and mainstream topographic profile in Valle las Flores basin. Note the good match between the knickpoint in the Hack profile and the main pounding fault intersection.

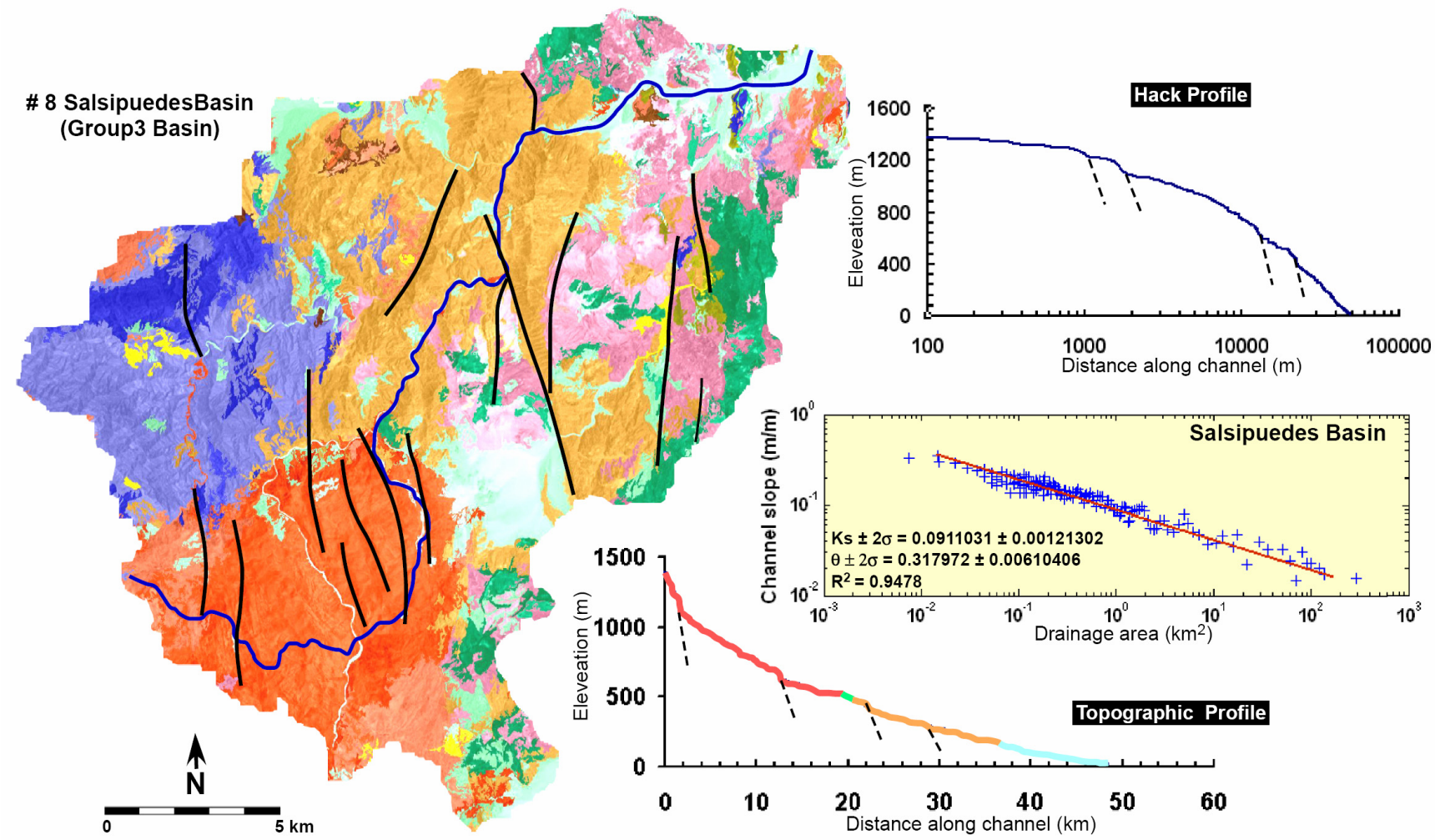

Figure 4.13. Hack profile, slope-area analysis, and main stream topographic profile in Salsipuedes basin.

indicated by the presence of a long and straight east-facing topographic scarp (best seen in Basin 11, Figure 4.12). Group 2 and 3 basins are highly correlated; both could be recognized as one group as indicated by the similarity in their Hack profiles, where Group 2 SL values are completely located within the zone of Group 3 (Figure 4.10). On the other hand, Group 4 basins show the lowest SL (min. 150 and max. 350) values with smooth, gently sloping profiles that show no signs of any possible knickpoints or any sudden slope changes (e.g., Basin 22, Figure 4.14). The clear gap between the maximum SL values of Group 4 (Basin 18) and the low SL values of Group 1 (Basin 16) indicate that Group 1 basins are tectonically more stable and geomorphologically more mature.

Because the main processes degrading the fault scarp are river incision, slope-area analysis of the main stream profile is used to calculate both channel concavity index (Θ) and channel steepness index (k_s) and quantitatively compare the four groups. Figure 15 shows the calculated concavity index and steepness index for the thirty-four drainage basins calculated by power-law regression analysis of stream slope against drainage area (see Figures 4.11, 4.12, 4.13 and 4.14). Using the least-squares/best-fit for the bedrock channel in the steeper part in the regression domain, the slope of this line represents the concavity indix (Θ), and the y-axis intercept is the steepness index (k_s). The measured concavity index values (Table 4.6) range from 0.24 to 0.56, which are typical values compared with most of the previous works (e.g., Willgoose *et al.*, 1990; Tarboton *et al.*, 1991; Slingerland *et al.*, 1998; Snyder *et al.*, 2000). The average concavity was 0.37 for the thirty-four drainage basins; that value represents mixed bedrock incisions of intrusive, extrusive and sedimentary rocks. The higher concavity values were observed

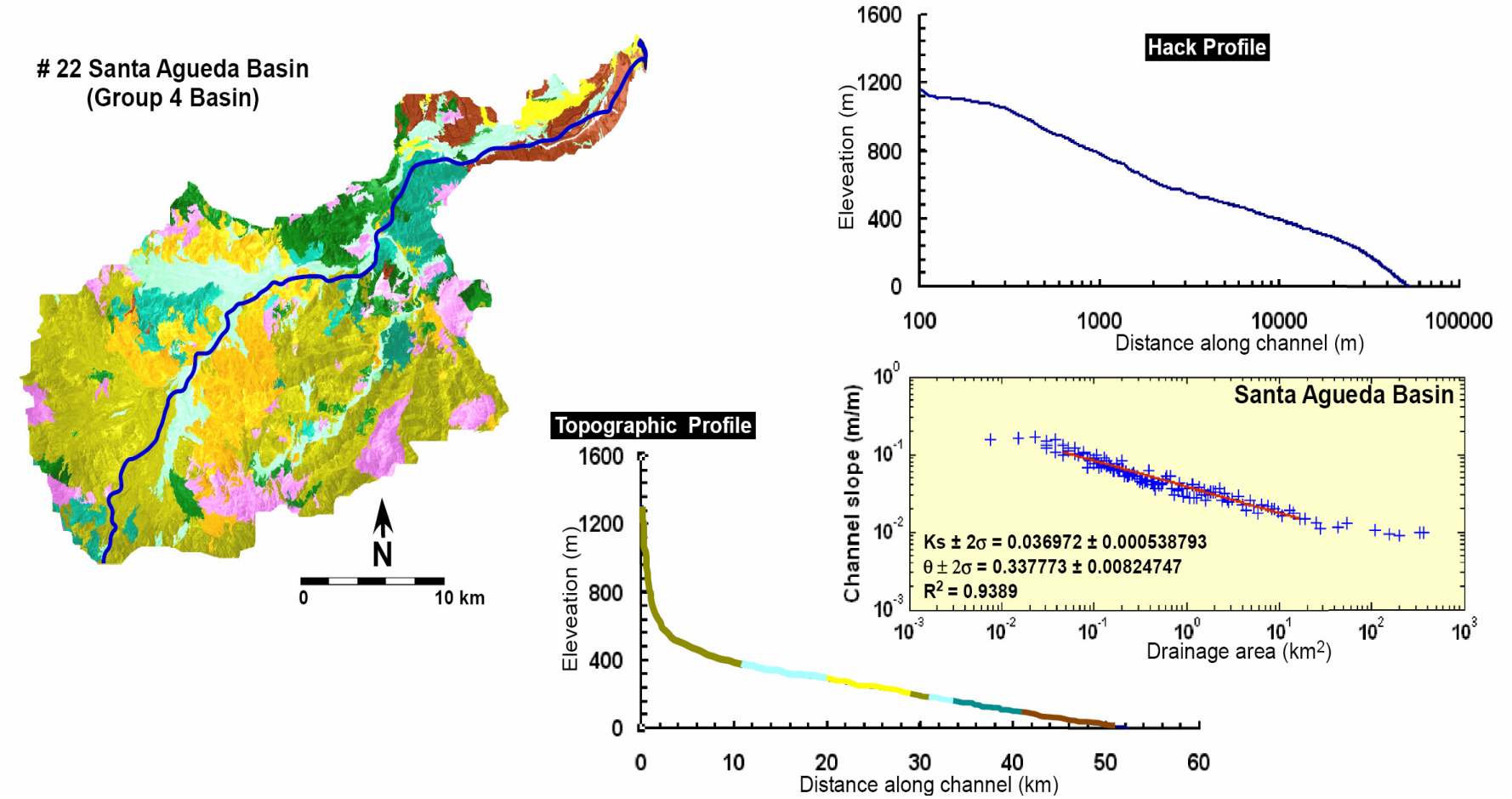

Figure 4.14. Hack profile, slope-area plot, and main stream topographic profile in Santa Agueda basin.

Table 4.6.Topographic Characteristics of Mainstream Profiles in Baja Extensional Province.

Basins	Principal Channel	R2	$k_s \pm 2\sigma$	$\Theta \pm 2\sigma$	k_s at (Θ=0.4)	k_s at (Θ=0.37)
1	Mal de Orin	0.87	0.087 ± 0.005	0.244 ± 0.026	0.060	0.067
2	La Palma	0.88	0.088 ± 0.008	0.286 ± 0.038	0.052	0.058
3	San Luis	0.90	0.089 ± 0.004	0.511 ± 0.030	0.107	0.113
4	Alfredo	0.72	0.083 ± 0.003	0.287 ± 0.023	0.056	0.060
5	Santa Maria	0.88	0.077 ± 0.001	0.294 ± 0.015	0.069	0.071
6	El Pozo	0.85	0.043 ± 0.002	0.468 ± 0.041	0.045	0.047
7	Calamajue	0.96	0.081 ± 0.001	0.348 ± 0.012	0.077	0.080
8	Salsipuedes	0.95	0.091 ± 0.001	0.317 ± 0.006	0.071	0.080
9	Mesa de Yubay	0.92	0.091 ± 0.001	0.289 ± 0.007	0.060	0.068
10	Canoncito	0.88	0.084 ± 0.002	0.239 ± 0.013	0.054	0.059
11	Valle las Flores	0.79	0.110 ± 0.002	0.248 ± 0.012	0.099	0.100
12	San Pedro	0.92	0.057 ± 0.001	0.356 ± 0.011	0.051	0.055
13	San Rafael	0.88	0.053 ± 0.001	0.378 ± 0.016	0.053	0.054
14	El Infiernito	0.72	0.055 ± 0.002	0.334 ± 0.023	0.047	0.049
15	Las Cuevitas	0.62	0.035 ± 0.000	0.260 ± 0.016	0.032	0.033
16	Santa Barbara	0.95	0.071 ± 0.001	0.328 ± 0.013	0.053	0.060
17	San Juan	0.95	0.034 ± 0.0008	0.321 ± 0.014	0.033	0.034
18	La Trinidad	0.82	0.028 ± 0.0007	0.392 ± 0.012	0.029	0.030
19	Palmarito	0.90	0.055 ± 0.0009	0.386 ± 0.009	0.057	0.058
20	Valle del Azufre	0.94	0.353 ± 0.0006	0.307 ± 0.011	0.033	0.034
21	El Yaqui	0.70	0.050 ± 0.0012	0.262 ± 0.015	0.044	0.045
22	Santa Agueda	0.94	0.036 ± 0.0005	0.337 ± 0.008	0.035	0.035
23	El Norte	0.88	0.026 ± 0.0006	0.490 ± 0.014	0.029	0.030
24	Boca de Magdalena	0.95	0.043 ± 0.0007	0.464 ± 0.009	0.046	0.048
25	Cadeje	0.89	0.072 ± 0.0021	0.524 ± 0.022	0.077	0.080
26	Jacobo	0.95	0.033 ± 0.0007	0.411 ± 0.011	0.034	0.035
27	La Tebaye	0.78	0.022 ± 0.0007	0.318 ± 0.021	0.020	0.021
28	Papini	0.94	0.080 ± 0.0016	0.410 ± 0.012	0.082	0.085
29	Las Virgenes	0.64	0.081 ± 0.0038	0.420 ± 0.003	0.081	0.083
30	Timbabichi	0.75	0.038 ± 0.0016	0.417 ± 0.030	0.039	0.041
31	Los Potreros	0.67	0.028 ± 0.0011	0.454 ± 0.017	0.039	0.040
32	El Coyote	0.88	0.075 ± 0.0031	0.560 ± 0.023	0.086	0.090
33	Las Tarambillas	0.73	0.046 ± 0.0024	0.445 ± 0.037	0.049	0.050
34	El Camaron	0.71	0.075 ± 0.0033	0.330 ± 0.025	0.065	0.069

in basins where the stream profiles are mostly dominated by sedimentary rocks (Whipple, 2004). We also observed that the calculated concavity values varied with the geometrical orientation of the main steam profile to the bounding normal faults (especially for Group basins 2 and 3). The stream profiles perpendicular to the escarpment strike show relatively low concavity values, which are mostly attributed to the adjustment of the channel gradient to possible uplift movements, especially in steady-state conditions (Kirby and Whipple, 2001). The steepness index (k_s), which depends on both uplift rate and erodibility of the bedrock, was also measured (Kirby and Whipple, 2001; Finlayson *et al.*, 2002; Duvall *et al.*, 2004; Kobor and Roering, 2004). The erodilibilty term contains both lithological and climatic effects. Concerning climate, we assume that although long-term climate may have changed along the peninsula over the last several million years, precipitation amounts are likely to be changed in a similar way along the entire length of the peninsula, regardless of the long-term climatic trend. This suggests that climatic variation can be largely ruled out as an explanation for the geomorphologic variability between basins (El-Sobky and Dorobek, 2005). The observed rock units along the main stream profiles of the drainage basins also showed a limited effect in terms of erodability variation as indicated by the concavity index values. Homogeneous substrate properties are required to derive meaningful comparisons of k_s with rock uplift, which is confirmed by the reverse correlation between Θ and k_s (Sklar and Dietrich, 1998; Kobor and Roering, 2004). Steepness index is calculated using $\Theta = 0.4$ (Snyder *et al.*, 2004) to facilitate direct comparison among the drainage basins. The measured k_s at reference $\Theta = 0.4$ (Figure 4.15) clearly

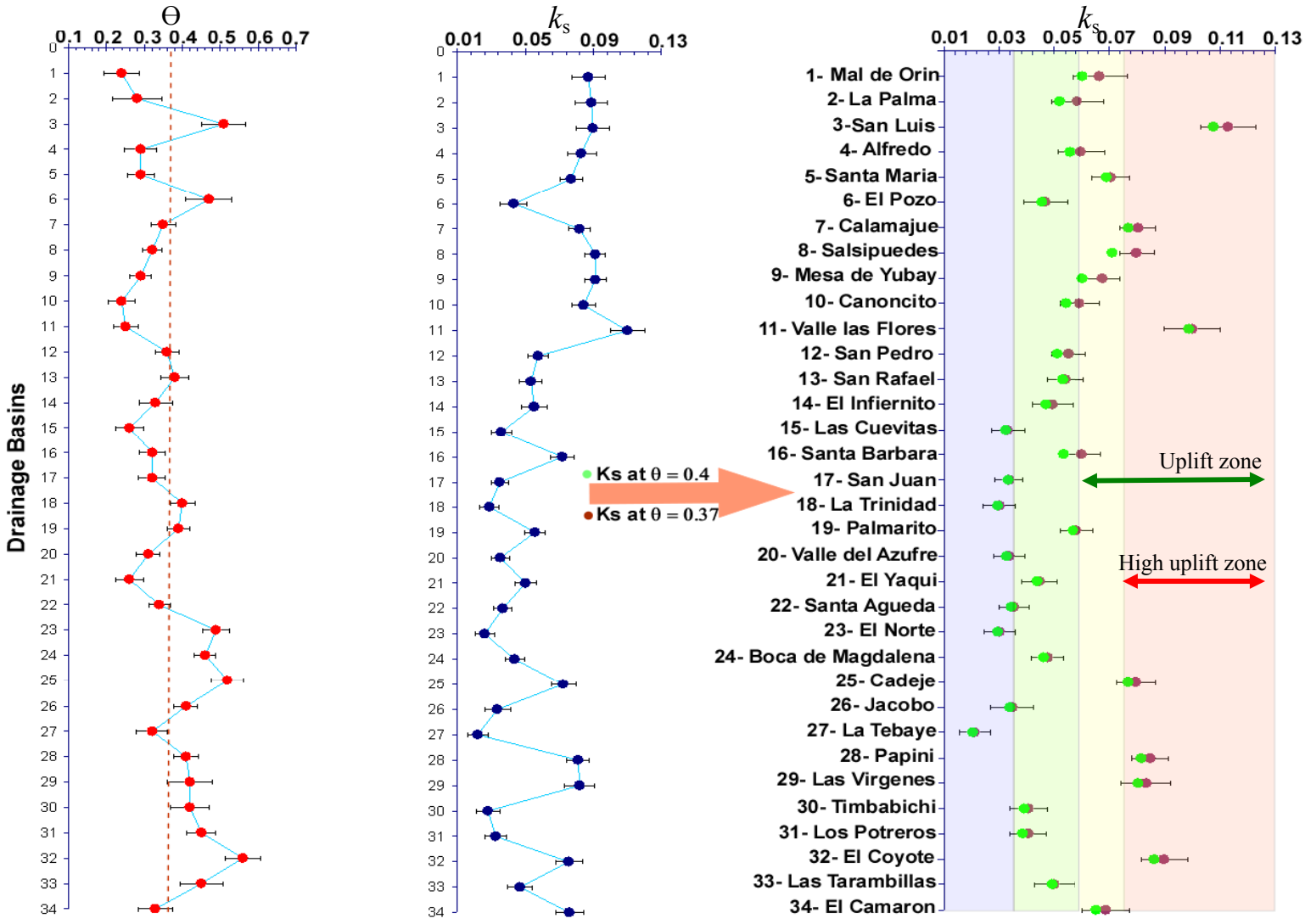

Figure 4.15. Concavity indices (Θ) and steepness indices (k_s) for the thirty-four basins. The final zones were defined from the values of k_s calculated at average value of Θ = 0.37. The nine basins were located inside the defined high uplift zone.

differentiates between Group 1 and Group 4 basins; however, the measured k_s at reference $\Theta = 0.37$ (actual measured concavity index average) clearly puts a boundary between Group 2 and Group 3 basins. In Group 4 basins, steepness indices are consistently low (average $k_s = 0.02$) with a minimal variation that does not follow any lithological variations or differential uplift rate. On the other hand, the steepness index values of Groups 2 and 3 are high enough to be correlated with a differential uplift rate. Nine basins have $k_s > 0.07$, indicating possibilities of higher differential uplift that could be recognized as boundaries of high uplift zones (Figure 4.15).

IV.4.3. Implications of regional tectonics to drainage basins classification results

Based on the assumptions that rule out the climatic effect in this area and that lithological input on the main stream morphological gradients is limited, then, the tectonic activity is the main forcing factor that is most probably responsible for sculpturing of the extensional provenance of Baja California. However, the distribution of the nine drainage basins that exhibited a clear evidence of uplift movements from the examination of their stream gradient indices as well as from their higher steepness indices are sporadic, which suggests local tectonic activity in these locations. The possible tectonic activities in the study area are either the Plio-Quaternary volcanism which is responsible for uplift of the marine Pleistocene terraces on the extensional coastal provinces (Schmidt, 1975; Demant, 1975; Ortlieb, 1980), or the activity associated with rifting of the Gulf of California from the mainland Mexico along the Gulf of California transform-rift. The Baja California peninsula has experienced

relatively slow and uniform uplift movements in the Quaternary, where it has been uplifted at a mean rate of 100 ±50 mm/10^3y over the last million years, and then this rate seemed to continue in some places and to decrease in other places through this period (Ashby *et al.*, 1987; Ortlieb, 1991; Ledesma-Vazquez and Johnson, 2001). The vertical movements that were recorded along the normal bounding faults were either related to a dip-slip, which is only responsible for a few meters of displacements, or to major fracture zones that show a large strike-slip component that produces stronger and wider vertical motions (Ortlieb, 1991). The second deformation supports our interpretation, where most of the normal bounding faults in the nine basins showed a clear strike-slip component; these are clearly recorded and recognized from the along-strike displacements in the downdip streams in the hanging wall fault blocks (e.g. Basin 5, Figure 4.9c). Additionally, in the central eastern part of Baja California the fault chronology showed that two main extensional movements were responsible for the activation of the NNW-SSE fault plane, NE-SW to ENE-WSW extensional movement followed by E-W to ESE-WNW extension. The latter movement had a stronger strike-slip component than the former one which is most probably related to the clockwise rotation of the horizontal to subhorizontal stress rotation (Angelier, 1981). However, Umhoefer and Stone (1996) related the kinematic behavior of the faults in the central extensional province of Baja California to their orientation relative to the direction of bulk extensional strain, where they defined two main fault groups. The first group is the north-striking faults, which are characterized by dip-slip movements, and the second group is the NE-striking faults that are characterized by dextral-normal to dextral strike-

slip. Zanchi (1994) related the N-S normal faults to the accommodation of the strain produced by motion along strike-slip faults. However, other workers identified active faults and related such activity directly to the rotation of the peninsular block towards the northwest (Nava-Sánchez, 2001). Figure 4.16 shows the location of the basins that may have the most observable tectonic activities. The major normal bounding faults of these basins are almost striking NE with a clear evidence of strike-slip movements as explained earlier. There is clear coincident matching between the locations of these basins and the locations of the en echelon transform faults that link the spreading center seated in the deep basins of the Gulf of California. This probably indicates that the plate boundary geometrical structure is controlling the uplift movements along the eastern coast of Baja California, where the movements along the transform faults may trigger the vertical uplift movements along the major fracture zones that have a pronounced strike-slip component. Ortlieb's (1991) findings supported our interpretation, where he recorded such connection between the rift structure and the uplift movements of the Pleistocene marine units that are relatively close to the deep fault systems of the gulf at many locations. We think that the bounding faults that are located in the zones that are most probably suffering from incremental extensional movements along a set of parallel strike-slip faults are becoming increasingly active. Concerning the seismotectonic activities of the study area, the distribution of the recent earthquakes and their focal mechanism "beach balls" (Figure 4.16) proved that the processes of incremental extensional movements, which are responsible for establishing the plate boundary (Humphrey and Weldon, 1991) are still active and continue to the present. Not only

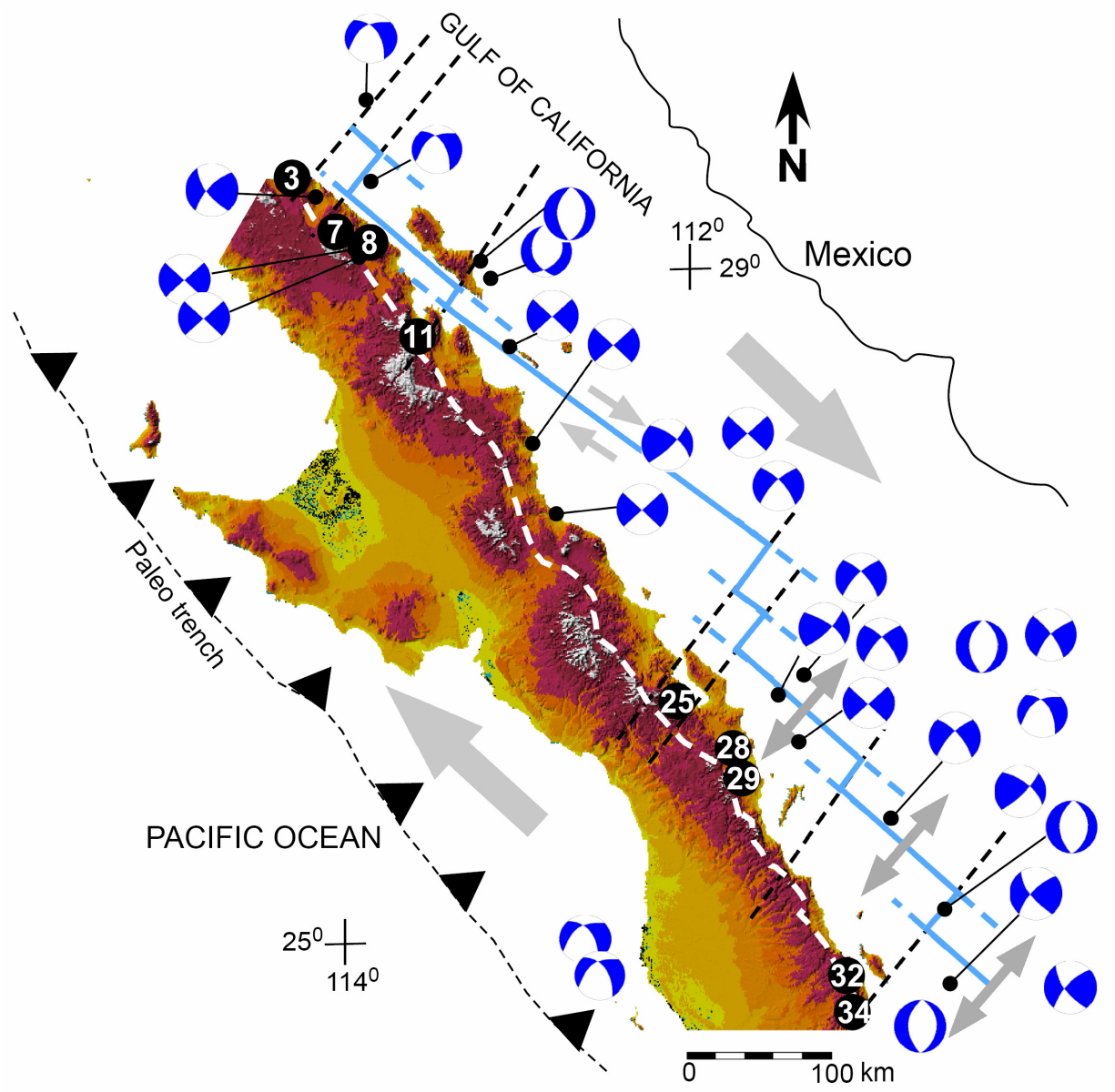

Figure 4.16. Shaded relief map of the study area shows the locations of the nine basins that may have the most observable tectonic activities. See Figure 3(a) for keyed basin names. The major tectonic framework of the Gulf of California is illustrated. Recent seismotectonic activities represented by the locations of the earthquakes, the focal mechanisms, correlate highly with the basin locations. Heavy dashed white lines show the positions of the major drainage divides.

that, but also the location of the focal points are constrained by the geometry of the transform faults either in the deep-seated gulf (Goff *et al.*, 1987) or at the coastal extensional provinces that are very close to the extensional ridge axis (e.g., Basins 3, 7 and 8, Figure 4.16).

Another insight of the present study is that it has revealed the character of the peninsular divide; i.e., whether is it structurally or volcanically controlled. Along the central domain of the extensional province, the extracted thirty-four basins, which are bounded by the peninsular divide, indicated that the divide is actually structurally as well as volcanically controlled. We found that almost all the basins of Group 2 and 3 were bounded by the structurally controlled divide, where the bounding normal faults are the main structural component of the divide. We believe that some of these faults are basement-involved faults as indicated by the abrupt termination of these faults along strike with the termination of the volcanic escarpment (e.g., Basin 11, Figure 4.17). On the other hand, Group 1 and 4 basins are controlled by a volcanically constructed divide (Figure 4.18). These observations further support the results of both cluster analysis and inices extracted from the main stream profile for these basins.

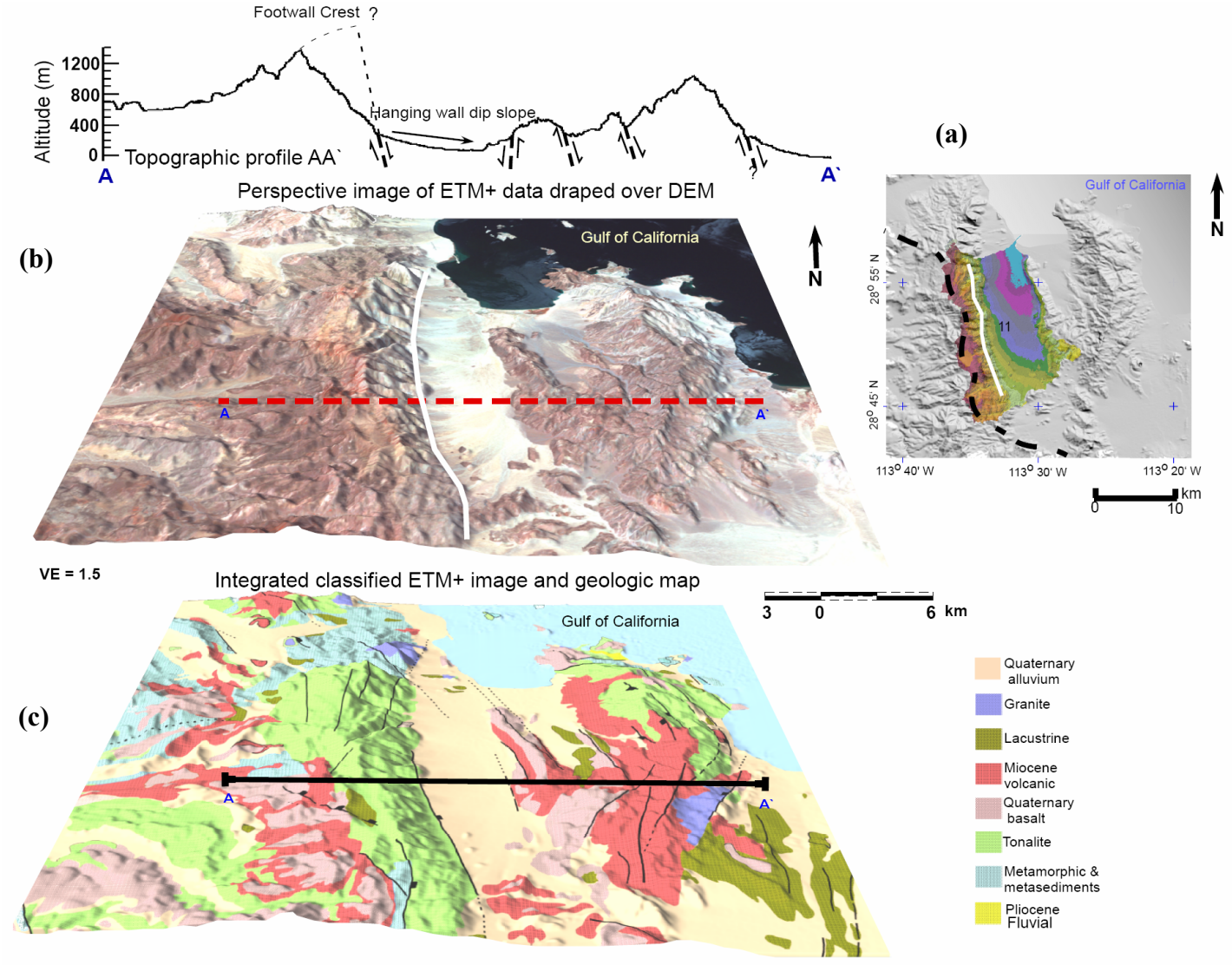

Figure 4.17. (a) Location of Valle las Flores basin. (b) Prospective 3-D image showing the AA′ profile, which shows the relation between the hanging wall dip slope and eroded-back footwall crest. (C) 3-D image of the integrated classified geological map.

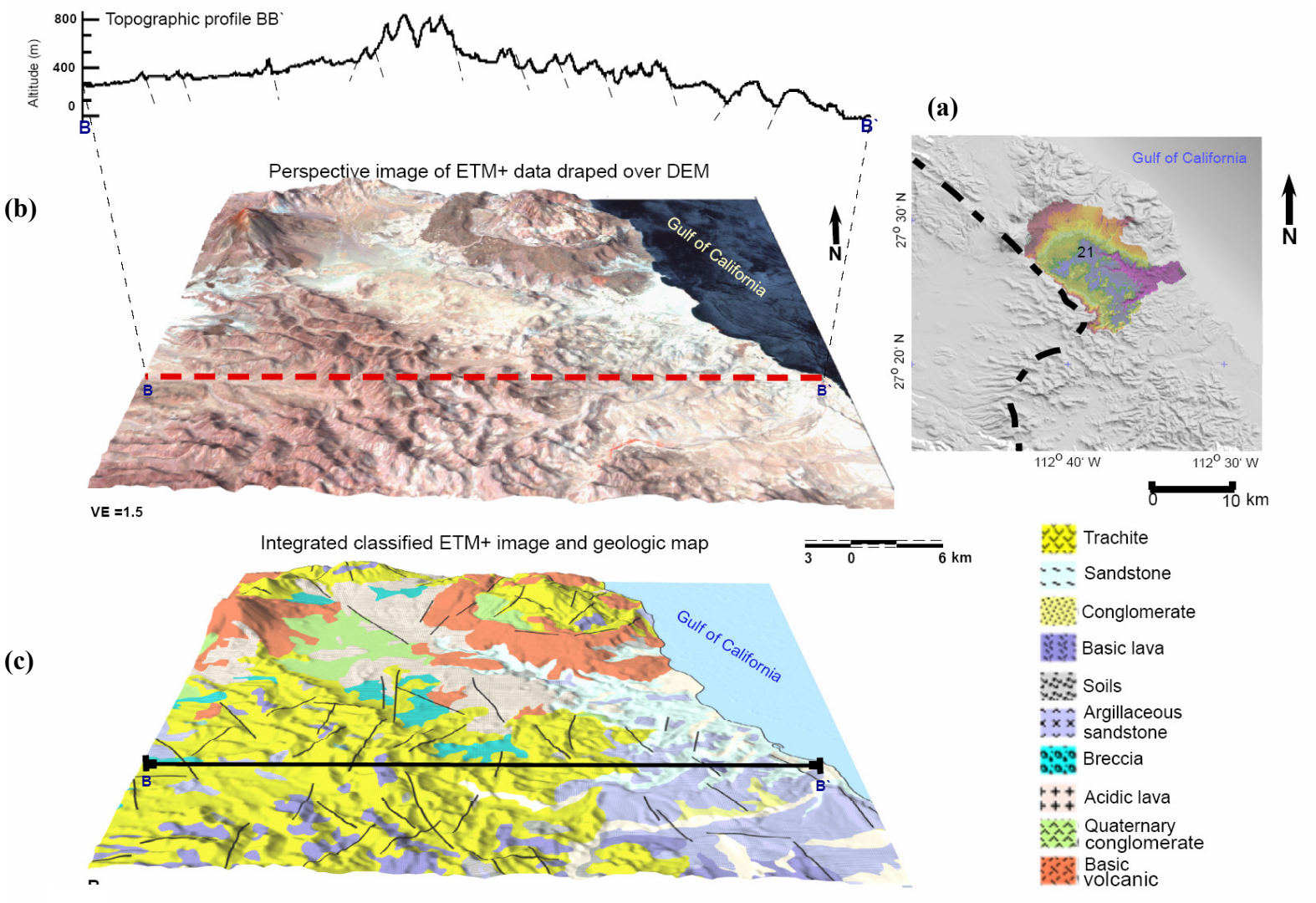

Figure 4.18. (a) Location of El Yaqui basin. (b) Prospective 3-D image showing the AA′ profile, which shows that this basin (see Figure 4.3 (c) for location) is bounded by a volcanically controlled peninsular divide (i.e., no extensional bounding faults). (C) 3-D image of the intergrated classified geological map.

IV.5. Summary and conclusions

A patched 15-m resolution DEM was used to extract the major Neogene drainage basins along the central tectonic domain of the Baja California extensional rift province. Both D-8 and D-Infinity algorithms were used to extract the drainage basins that are mostly bounded by the peninsular divide in the west side and draining to the Gulf of California. Of these basins, thirty-four were selected to examine the interaction between the prevailing geomorphic forcing factors. Thirty geomorphometric parameters were extracted for each drainage basin. These parameters were then reduced into five orthogonal uncorrelated PCs that explained 80.77% of the total variance, using VARIMAX normalized rotation of principal component analysis. PC1 was interpreted as a length-area sensitive component, PC2 as an elevation sensitive component, PC3 as a factor component, and PC4 as a sinuosity-sensitive component. The Euclidian criterion distance of cluster analysis was used to classify the thirty-four drainage basins into similar or correlated groups using the five PCs. Four major groups were clearly recognized from the hierarchical dendrogram, which was constructed using an average linkage method. Stream length-gradient indices and slope-area analysis of the main stream profiles of the thirty-four drainage basins were then used to examine the results of the multivariate analysis. Stream length-gradient index results proved the reliability of the classification results where Group 2 and 3 basins show higher SL indices than Groups 1 and 4. Five basins showed unexpectedly high SL values, which were interpreted as a result of the erodibility changes resulting from lithological variation along their mainstream profile. For Groups 2 and 3, the most recognized knickpoints in

the Hack profiles matched the intersection with the bounding normal faults. This result indicats that there is a strong possibility of differential uplift movements along the extensional bounding footwall blocks of Group 2 and 3 basins. Our result was further supported by the slope-area analysis of the main stream profile, where the measured steepness index (k_s) values were high enough to strongly support the presence of differential tectonic uplift movements along the extensional bounding faults of Group 2 and 3 basins. Nine basins showed remarkably high k_s values with their extensional bounding faults striking NNW to NW. The location of these basins was correlated with the major tectonic framework and seismotectonic activities of both the Baja California peninsula and the Gulf of California, where a clear correlation is observed. Also the location of the recent earthquakes, the focal mechanisms show that activity is still possible along the extensional bounding faults as a result of possible incremental movements along the strike-slip faults of the Gulf.

CHAPTER V

GENERAL SUMMARY

In an attempt to understand the relationship between topography, climate, tectonics and lithology of the extensional provinces of two-thirds of the Baja California peninsula, we started by introducing a technique for resolving a problem that commonly arises when working with DEM, namely, how to fill various artifacts with elevation values that are statistically robust and geologically meaningful. In this part of study, we used a number of geostatsitical techniques (e.g., ordinary kriging, cokriging, ACE) to patch the DEM of the SRTM with meaningful values that honor the geology in the area of study. First we used ordinary kriging, which fails to account for natural geological and topographical variations that are commonly obscured by smoothing. We then used the ACE algorithm to provide an optimal non-parametric transformation of the eight bands in ETM+ data. Using the results of the ACE algorithm, cokriging generated geologically realistic maps with minimal smoothing effect. We found that the performance and effectiveness of the cokriging method is completely controlled by the degree of correlation between the secondary variables (i.e., the eight thematic mapper bands) and the elevation. To examine the accuracy of the introduced technique, RMSE was calculated using twenty-four ground control points for validation of the estimated elevation values within data gaps that we artificially introduced into the SRTM DEM. The RMSE had an average value of 7.22-m at the corrected locations, which is a reflection of the robustness of our technique. The corrected SRTM DEM was used in the

algorithm of automated stereo-correlation to generate the ASTER DEM, which successfully produced very good results. The proposed technique produced an artifact-free DEM that has 15-m spatial resolution and comparable to the USGS 1-arc second DEM.

In the second part of study, we used the privilage of the previously introduced technique to generate continuous and high resolution geologic maps for the study area between the Baja peninsular divide and the western coastal line of the Gulf of California, which is divided into twenty-two blocks. We used multisiurce data in eCognition software V.4.0 to implement the segmentation process based on image objects rather than on a single pixel. This approach successfully resolved any classification problems that might have arisen from using single-source data. In eCognition, classification is based on thresholds and a fuzzy classification system, which are in turn based on membership functions. We examined the accuracy of the classified images using this technique, where the accuracy assessment by error matrix resulted in and average of 86% overall accuracy, indicating that this approach can be highly recommended over most conventional classification techniques.

In the third part of study, thirty-four drainage basins were extracted from a 15-m-resolution absolute digital elevation model (DEM) using both D-8 and D-Infinity algorithms. These basins are mostly bounded by the peninsular divide in the west side and drain to the Gulf of California. Thirty morphometric parameters were extracted for each basin. The VARIMAX normalized rotation of principal component analysis was used to reduce these parameters into five PCs that explained 80.77% of the total

variance. A Euclidian criterion distance of cluster analysis was used to classify the thirty-four drainage basins into similar or correlated groups using the five PCs, where four major groups were identified. We relied on the response characteristics of main stream analysis to explain the results of clustering. First we started with the stream length-gradients, which were measured at every gradient change along the main-stream profile down dip for the thirty-four basins and then calculated the average SL be the representative value for each basin. Second, we used slope-area analysis of the main stream profile was used to calculate both channel concavity index (Θ) and channel steepness index (k_s). We quantitatively compared the results of both SL indices and the stream-area analysis and the clustering results, where this comparison proved the sensitivity of the morphometric parameter to reveal the uniqueness of Neogene rift drainage basins based on the prevailing geomorphic forcing factors of each basin. Additionally, we correlated the location of these basins with the major tectonic framework and seismotectonic activities of both the Baja California peninsula and the Gulf of California, where a clear correlation was observed.

REFERENCES

Ackermann, F., 1984. Digital image correlation: performance and potential application in photogrammetry. *Photogrammetric Record,* 11(64): 429– 439.

Addink, E.A., and A. Stein, 1999. A comparison of conventional and geostatistical methods to replace clouded pixels in NOAA-AVHRR images. *International Journal of Remote Sensing*, 20(5):961-977.

Ahnert, F., 1970. Functional relationships between denudation, relief, and uplift in large mid-latitude drainage basins, *American Journal of Science*, 268:243-263.

Aldenderfer, M.S., and R.K. Blashfield, 1984. *Cluster Analysis*, Sage University Paper, Quantitative Applications in the Social Sciences, 88 p.

Allen, D.M., 1974. The relationship between variable selection and data augmentation and a method for prediction, *Technometrics*, 16(1):125-127.

Angelier, J., B. Colletta, J. Chorowicz, L. Ortlieb, and C. Rangin, 1981. Fault tectonics of the Baja California peninsula and the opening of the Sea of Cortez, Mexico, *Journal of Structural Geology*, 3:347–357.

Argialas. D., P. Derzekos, 2003. Mapping urban green from IKONOS data by an object-oriented knowledge-base and fuzzy logic, *In Proceeding SPIE: Remote Sensing for Environmental Monitoring, GIS Applications, and Geology II* (Manfred Ehlers, editor), 22-27 September, Aghia Pelagia, Crete Vol. 4886, pp. 96-106.

Argnani, A., M. Bernini, G. M. Di Dio, G. Papani, and S. Rogledi, 1997. Stratigraphic record of the crustal-scale tectonics in the Quaternary of the northern Apennines (Italy), *Il Quaternario*, 10: 597-604.

Arik, Abdullah, 2002. Area influence kriging, *Mathematical Geology*, 34(7):783-796.

Arkley, R.J., 1971. Factor analysis and numerical taxonomy of soils, *Soil Science Society of American Proceeding*, 35:312–315.

Arkley, R.J., 1976. Statistical methods in soil classification research, *Advanced Agronomy*, 28:37–70.

Armstrong, M., 1984, Improving the estimation and modeling of the variogram, *Geostatistics for Natural Resources Characterization* (G. Verly and others, editors), Reidel, Dordrecht, The Netherlands, pp. 1–20.

Arroyo, L., S. Healey, W. Cohen, D. Cocero, and J.A. Manzanera, 2005. Regional fuel mapping using an object-oriented Classification of Quickbird imagery, *In* Proceedings of NARGIS 2005 - applications in tropical spatial science. 4th - 7th July 2005, Charles Darwin University, Darwin, NT, Australia.

Arvidson, R., R. Becker, A. Shanabrook, W. Luo, N. Sturchio, M. Sultan, Z. Lotfy, A.M. Mahmood, and Z. El-Alfy, 1994. Climatic, eustatic, and tectonic controls on

quaternary deposits and landforms, Red Sea coast, Egypt, *Journal of Geophysical Research,* 99:12175-12190.

Ashby, J.R., T.L. Ku, and J.A. Minch, 1987. Uranium series ages of corals from the upper Pleistocene Mulege terrace, Baja California Sur, Mexico, *Geology*, 15:139–141.

Atkinson, P.M., and N.J. Tate, 2000. Spatial scale problems and geostatistical solutions: a review, *Professional Geographer*, 52(4):607-623

Atkinson, P. M., R. Webster, and P. J. Curran, 1992. Cokriging with ground-based radiometry, *Remote Sensing of Environment,* 41:45-60.

Atkinson, P.M., Webster, R. and Curran, P.J. 1994. Cokriging with airborne MSS imagery, *Remote Sensing of Environment*, 50:335-45.

Atwater, T., 1970. Implications of plate tectonics for the Cenozoic tectonics of western North America, *Geological Society of America Bulletin*, 81(12):3513-3536.

Atwater, T., 1989. Plate tectonic history of the northeast Pacific and western North America, *The Eastern Pacific Ocean and Hawaii. Boulder, Colorado*, (E.L. Winterer, et al., editors), *Geologic Society of America*, *Geology of North America*, N:21–72.

Atwater, T., and J. Stock, 1998. Neogene plate tectonic history of southwestern United States: an update, *New Zealand Geophysical Society Joint Annual Conference: Programme and Abstracts*, Geological Society of New Zealand Miscellaneous Publications, 101A, 31.

Austin, M. P., and P. Greig-Smith, 1968. The application of quantitative methods to vegetation survey. II. Some methodological problems of data from rain forests, *Journal of Ecology,* 56:827–844.

Axen, G., 1995. Extensional segmentation of the Main Gulf Escarpment, Mexico and United States, *Geology*, 23:515–518.

Axen, G.J., and J.M. Fletcher, 1998. Late Miocene-Pleistocene extensional faulting, northern Gulf of California, Mexico and Salton Trough, California, *International Geology Review*,40:217-244.

Axen, G.J., M. Grove, D. Stockli, O.M. Lovera, D.A. Rothstein, J.M. Fletcher, K. Farley, and P.L. Abbott, 2000. Thermal evolution of Monte Blanco Dome; low-angle normal faulting during Gulf of California rifting and late Eocene denudation of the eastern Peninsular Ranges, *Tectonics*, 19:197–212.

Ayeni, O. O. 1985. Photogrammetry as a tool for national development, *Photogrammetric Engineering and Remote Sensing*, 51(4): 445-454.

Azor, A , E.A. Keller, 1999. Geomorphic lndlcators of fold growth: South Mountain, Ventura Basin, Southern Caltfornia, *Geological Society America*, Abstracts Programs 31, A-47.

Baatz et al., 2004. *eCognition Professional User Guide 4*, Definiens, Munich, 486 p.

Baatz, M., and A. Schäpe 1999. Object-oriented and multi-scale image analysis in semantic networks, *The 2nd International Symposium: Operationalization of Remote Sensing*, *New Methodologies*, 16-20 August 1999, ITC, NL.

Baatz, M., and A. Schape, 2000. Multiresolution segmentation - an optimization approach for high quality multi-scale image segmentation, *Angewandte Geographische Informationsverarbeitung XII* (J. Strobl et al., editiors), AGIT Symposium, Salzburg, Germany, 2000. pp. 12-23.

Baatz, M., et al. 2003. *eCognition User Guide 3,* Definiens Imaging, Germany, pp. 32-108.

Bailey, T. C., and A. C. Gatrell, 1995. *Interactive Spatial Data Analysis*, John Wiley and Sons, New York, NY.

Bandy, W.L., and M. Pardo, 1994. Statistical examination of the existence and relative motion of the Jalisco and southern Mexico blocks, *Tectonics*, 13:755–768.

Bargos, T., J.Mesanza, A. Basaguren, and E. Orive, 1990. Assessing river water quality by means of multifactoral methods using macroinvertebrates: a comparative study of main water courses of Biscay, *Water Research*, 24:1–10.

Bartholomew, M.J., 1968. Geology of the southern portion of the Fonts Point quadrangle and the southwestern portion of the Seventeen Palms quadrangle, San Diego County, California, M.S. thesis, Los Angeles, University of Southern California, 60 p.

Bemstein R., 1976. Digital image processing of earth observation sensor data, *IBM Journal of Research and Development*, 20(1):40-57.

Ben-David, R., Y. Eyal, E. Zilberman, and D. Bowman, 2002. Fluvial systems response to rift margin tectonics: Makhtesh Ramon area, southern Israel, *Geomorphology*, 45:147–163.

Benediktsson, J. A., P. H. Swain, and O. K. Ersoy, 1990b. Neural network approaches versus statistical methods in classification of multisource remote sensing data, *IEEE Transactions on Geoscience and Remote Sensing,* 28(4):540-552.

Benediktsson, J. A., P. H. Swain, O. K. Ersoy, and D. Hong, 1990a. Classification of very high dimensional data using neural networks, *Proceedings of the International Geoscience and Remote Sensing Symposium,* 20-24 May 1990, the University of Maryland, Maryland, IGARSS'90, (New York: Institute of Electrical and Electronics Engineers), pp. 1269-1272.

Benediktsson, J.A., and P.H. Swain, 1989a. A method of statistical multisource classification with a mechanism to weight the influence of the data sources, *Proceedings* '89 *IGARSS,* July 10-14 Vancouver, B.C., Canada, , pp. 517-520.

Benediktsson, J.A., P.H. Swaini, and O.K. Ersoy, 1990b. Neural network approaches versus statistical methods in classification of multisource remote sensing data, *IEEE Transactions on Geoscience and Remote Sensing,* 28(4):540-551.

Benito, G., M.J. Machado, A. Perez-Gonzalez, and A. Sopena, 1998. Paleoflood hydrology of the Tagus River, *Palaeohydrology and Environmental Change* (G. Benito, V.R. Baker and K.J. Gregory, editors), John Wiley and Sons, NewYork, pp. 317-333.

Bennett, R.A., W. Rodi, and R.E. Reilinger, 1996. GPS constraints on fault slip rates in Southern California and Northern Baja, Mexico, *Journal of Geophyical Reearch*, 101(21):943-960.

Benz, U., P. Hofmann, G. Willhauck, I. Lingenfelder, and M., Heynen, 2004. Multi-resolution, object-oriented fuzzy analysis of remote sensing data for GIS-ready information, *ISPRS Journal of Photogrammetry and Remote Sensing*, 58:239-258.

Bertotti, G., S. Cloetingh, G. Spadini, Y. Podladchickov, and V. Picotti, 1997. Kinematics and dynamics of the fast continental rifting and passive margin formation in the Tyrrhenian Sea (Mediterranean), Abstract with programs – *Geological Society of America*, 29 (6):317.

Bhatti, A.V., D. Mulla, and B. Frazier, 1991. Estimation of soil properties and wheat yields on complex eroded hills using geostatistics and Thematic Mapper images, *Remote Sensing of Environment*, 37:181-91.

Bischof H., W. Schneider, and A.J. Pinz, 1992. Multispectral classification of Landsat images using neural networks, *IEEE Transactions on Geoscience and Remote Sensing*, 30(3):482-490.

Bishop, P., T.B. Hoey, J.D. Jansen, and I.L. Artza, 2005. Knickpoint recession rates and catchment area: the case of uplifted rivers in eastern Scotland, *Earth Surface Processes and Landforms*, 30:767-778.

Blaschke, T., and J. Strobl, 2001. What's wrong with pixels? Some recent developments interfacing remote sensing and GIS. *GIS*, 6:12-17.

Bogaart, P.W., and R.T. van Balen, 2000. Numerical modeling of the response of alluvial rivers to quaternary climate change, *Global and Planetary Change,* 27:147–163.

Bohannon, R.G., and T. Parsons, 1995. Tectonic implications of post–30 Ma Pacific and North American relative plate motions, *Geological Society of America,* 107:937–959.

Bonnet, S., F. Guillocheau, and J.-P. Brun, 1998. Relative uplift measured using river incision: The case of the Armorican basement (France), *Comptes Rendus de l'Academie des Sciences,* Paris, II, 327:245 – 251.

Braun, J., and C. Beaumont, 1989. A physical explanation of the relationship between flank uplifts and the breakup unconformity at rifted continental margins, *Geology*, 17:760-764.

Breiman L., 1996. Bagging predictor, *Mach Learn* 24(2):123-40.

Breiman, L., and J. H. Friedman , 1985. Estimating optimal transformations for multiple regression and correlation*, Journal of Amererican Statisical. Association*, 90(391):580-598.

Brown, D. G., B. C. Pijanowski, et al., 2000. Modeling the relationships between land use and land cover on private lands in the Upper Midwest, USA, *Journal of Environmental Management,* 59(4): 247-263.

Brown, M.P., W.N. Grundy, D. Lin, N. Cristianini, C.W. Sugnet, T.S. Furey, M. Ares Jr., and D. Haussler, 2000. Knowledge-based analysis of microarray gene expression data by using support vector machines, *Proceedings of the National Academy of Sciences USA*, 97:262– 267.

Bull, W. B., 1977. Tectonic geomorphology of the Mojave Desert, U.S. Geol. Surv. Contract Rep. 14-08-001-G-394, Office of Earthquakes, *Volcanoes and Engineering*, Menlo Park, California, p.188.

Bull, W. B., and L. D. McFadden, 1977. Tectonic geomorphology north and south of the Garlock fault, California, *Geomorphology in Arid Regions, Proceeding 8th Annual Geomorphology Symposium* (D. O. Doehring, editor) State Univiversity of New York at Binghamton, pp.115–138.

Burbank, D.W., J. Leland, E. Fielding, R.S. Anderson, N. Brozovic, M.R. Reid, and C. Duncan, 1996. Bedrock incision, rock uplift and threshold hillslopes in the northwestern Himalayas, *Nature*, 379:505–510.

Campbell, A. S., J. A. Adams, and D. T. Howarth, 1970. Some problems encountered in the identification of plumbogummite minerals in soils, *Clay Minerals*, 9:415-23.

Castellarin, A. and G.B. Vai, 1986. South alpine versus Po Plain Apenninic arcs, *The Origin of Arcs* (F.C. Wezel, editor), Elsevier Science Publishers B.V., Amsterdam, pp. 253–280.

Chambers, R.L., and J.M. Yarus, 2001. GEOSTATISTICS: A Powerful Reservoir Modeling Tool, Course #3, E&P Technologies and Workflows, Selection and Applications, *AAPG Annual Meeting* Pre-Convention Short Courses, June 7-9, Denver, CO, 123 p.

Chen, J. M., C. H. Menges, and S. G. Leblanc, 2005. Global mapping of foliage clumping index using multi-angular satellite data, *Remote Sensing of Environment*, 97(4):447-457.

Chica-Olmo, M., and F. Abarca-Hernandez, 2000. Computing geostatistical image texture for remotely sensed data classification, *Computers & Geosciences,* 26:373-383.

Chorley, R. J., 1969. The drainage basin as the fundamental geomorphic unit, *Introduction to Physical Hydrology* (R.J. Chorley, editor), London: Methuen, pp. 37-60.

Chorley, R.J., S.A. Schumm, and D.E. Sugden, 1984. *Geomorphology.* Methuen, London. 605 p.

Chubey, M., S. Franklin, and M. Wulder, 2006. Object-based analysis of Ikonos-2 imagery for extraction of forest inventory parameters, *Photogrammetric Engineering & Remote Sensing*, 72(4):383–394.

Civco, D. L., 1993. Artificial neural networks for land-cover classification and mapping, *International Journal of Geographical Information Systems*, 7:173-186.

Clift, P.D., N. Shimuzuz, G.D. Layne, and J. Blusztajn, 2001. Tracing patterns of erosion and drainage in the Paleogene Himalaya through ion probe Pb isotope analysis of detrital K-feldspars in the Indus Molasse, India, *Earth and Planetary Science Letters*, 188:475-491.

Colella, A., L. De Boer, and S. D. Nio, 1987. Sedimentology of a marine intermontane Pleistocene Gilbert-type fan-delta complex on the Crati Basin, Calabria, southern Italy, *Sedimentology*, 34:721-736.

Colombo O.L., A.G. Evans, M. I. Vigo, J.J. Benjamin, and J.M. Ferrandiz, 2000. Long-baseline (> 1000 km), sub-decimeter kinematic positioning of buoys at sea, with potential application to deep-sea studies, *In Proceedings of the 13th International Technical Meeting of the Satellite Division of the U.S. Institute of Navigation,* 19-22 September, Salt Lake City, Utah, , pp.1476-1484.

Coltorti, M., and P. Pieruccini, 2000. A late lower Pliocene planation surface across the Italian Peninsula: a key tool in neotectonic studies, *Journal of Geodynamics*, 29:323-328.

Contreras, J., and C. Scholz, 2001. Evolution of stratigraphic sequences in multisegmented continental rift basins: Comparison of computer models with the basins of the East African rift system, *American Association of Petroleum Geologists Bulletin*, 85:1565-1581.

Costa-Cabral, M., and S. J. Burges, 1994. Digital elevation model networks (DEMON): A model of flow over hillslopes for computation of contributing and dispersal areas, *Water Resources Research*, 30(6):1681–1692,

Cox, R.T., 1994. Analysis of drainage-basin symmetry as a rapid technique to identify areas of possible quaternary tilt-block tectonics: an example from the Mississippi Embayment, *Geological Society of America Bulletin,* 106:571– 581.

Cox, R.T., R.B. Van Arsdale, and J.B. Harris, 2001. Identification of possible Quaternary deformation in the northeastern Mississippi Embayment using quantitative geometric analysis of drainage basin asymmetry, *Geological Society of America Bulletin,* 113:615– 624.

Cushing, C. E., C. D. Mcintire, J. R. Sedell, G. W. Minshall, K. W. Cummins, R. C. Petersen, and R. I. Vannote, 1980. Comparative study of physical-chemical variables of streams using multivariate analyses, *Archeological Hydrobiology*, 89:343-352.

Damm, A., P. Hostert, S. Schiefer, 2005. Investigating urban railway corridors with geometric high resolution satellite data, *Urban Remote Sensing*, Berlin Adlershof.

Davis, J.C., 1973. *Statistics and Data Analysis in Geology*. John Wiley & Sons, New York, 550 p.

Davis, W. M., 1899. The geographic cycle, *Journal* of *Geography,* 14:481–504.

Del Giorgio, P. A., R. J. Vinocur, R. J. Lombardo, and G. H. Tell, 1991. Progressive changes in the structure and dynamics of the phytoplankton community along a pollution gradient in a lowland river–a multivariate approach, *Hydrobiologia*, 224:129–154.

Demant, A., 1975. Caracteres químicos principales del volcanismo terciario y cuaternario de Baja California Sur. Relaciones con la evolución del margen continental Pacífico de México, UNAM, *Inst. Geological Review*, 75:21-71.

DeMets, C., 1995. A reappraisal of seafloor spreading lineations in the Gulf of California: Implications for the transfer of Baja California to the Pacific plate and estimates of Pacific–North America motion, *Geophysical Research Letters*, 22:3545–3548.

DeMets, C., and T.H. Dixon, 1999. New kinematic models for Pacific-North America motion from 3 Ma to present, I: evidence for steady motion and biases in the NUVEL-1A model, *Geophysical Research Letters,* 13:1921-1924.

Deutsch, C.V., 2002. *Geostatistical Reservoir Modeling*, Oxford University Press, New York, 376 p.

Deutsch, C.V., 2002. Geostatistics, in *Academic Press Encyclopedia of Physical Science and Technology*, Third Edition, 6:697-707.

Deutsch, C.V., and A.G. Journel, 1992. *GSLIB: Geostatistical Software Library and User's Guide*, Oxford University Press, New York, 369 p.

Diaz, T.A., T.L. Bailley, and R.L. Orndorff, 2002. SEM analysis of vertical and lateral variations in desert varnish chemistry from the Lahontan Mountains, Nevada, *Geological Society of America Abstracts with Programs*, May 7-9 Meeting, URL:<gsa.confex.com/gsa/2002RM/finalprogram/abstract_33974.htm>,(Last date accessed: October, 2005).

Dickinson, W. R., 1996. Kinematics of transrotational tectonism in the California Transverse Ranges and its contribution to cumulative slip along the San Andreas transform fault system, *Geological Society of America Special Paper,* 305, 46 p.

Dickinson, W.R., and W.S. Snyder, 1979. Geometry of subducted slabs related to the San Andreas transform, *Journal of Geology*, 87:609–627.

Dietrich W.E., D. Bellugi, A.M. Heimsath, J.J. Roering, L. Sklar, and J.D. Stock, 2003. Geomorphic transport laws for predicting the form evolution of landscapes, *Prediction in Geomorphology* (P.R. Wilcock and R. Iverson, editors), American Geophysical Union, Washington D.C., pp. 103–32.

Dietrich, W. E., C. J. Wilson, D. R. Montgomery, and J. McKean, 1993. Analysis of erosion thresholds, channel networks and landscape morphology using a digital terrain model, *Journal of Geology*, 101:259- 278.

Doglioni C., D. Green, and F. Mongelli, 2005. On the shallow origin of hotspots and the westward drift of the lithosphere, Plates, Plumes, and Paradigms (G.R. Foulger, J.H. Natland, D.C. Presnall and D.L. Anderson, editors), Geological Society of America Special Paper 388, pp. 735-749.

Doglioni, C., E. Carminati, and E. Bonatti, 2003. Rift asymmetry and continental uplift, *Tectonics*, 22:8-13.

Duvall, A., E. Kirby, and D. Burbank, 2004. Tectonic and lithologic controls on bedrock channel profiles and processes in coastal California, *Journal of Geophysical Research*, 109, F03002, doi:10.1029/2003JF000086.

Dunne, T., 1980. Formation and controls of channel networks, *Progress Physical Geography*, 4:211–239.

Dymond, J.R., and Shepherd, J.D., 1999. Correction of the topographic effect in remote sensing, *IEEE Transactions on Geoscience and Remote Sensing*, 37:2618–2620.

Ehlers, M., and R. Welch, 1987. Stereocorrelation of landsat TM images, *Photogrammetric Engineering and Remote Sensing*, 53(9):1231–1237.

El-Sobky, H., and S.L. Dorobek, (in correction) 2007. Geostatistical manipulations of SRTM data to generate high resolution perspective images, Baja California, *Photogrammetric Engineering and Remote Sensing*.

El-Sobky, H., and S.L. Dorobek, 2004. Morphometric classification and multivariate analyses of drainage networks in arid rift basins using remote sensing data, Baja California, Mexico, Eos *Trans. AGU*, 85(47), Abstract.

El-Sobky, H., and S.L., Dorobek, 2005. Quantifying the forcing factors responsible for the tectono-geomorphological evolution of neogene rift basins, Baja California, *Eos Trans.*, AGUFM.H31A1265E, Abstract.

El-Sobky, H.F. and S.L. Dorobek, 2006. Using ETM+ imagery to constrain cokriging interpolation of the shuttle rader digital elevation model, *Geophysical Research Abstracts*, 8, 01755, EGU06-A-01755, Abstract.

El-Sobky, H.F., 1999. *Structural Analysis Using Remote Sensing Techniques and Field Investigation of Siwa Oasis, Western Desert, Egypt*, Master Thesis, Alexandria University, Egypt, 256 p.

Erdas Imagine, 2003. *Erdas Field Guide*, Erdas Inc, Atlanta, Georgia, 672 p.

Finlayson, D., D.R. Montgomery, and B.H. Hallet, 2002. Spatial coincidence of rapid inferred erosion with young metamorphic massifs in the Himalayas, *Geology,* 30:219– 222.

Fisher, T.G., and C. Souch, 1998. Northwest outlet channels of Lake Agassiz, isostatic tilting and a migrating continental drainage divide, Saskatchewan, Canada, *Geomorphology*, 23:57–73.

Flanders, D., M. Hall-Beyer, and J. Pereverzoff, 2003. Preliminary evaluation of eCognition object-based software for cut block delineation and feature extraction, *Canadian Journal of Remote Sensing*, 29(4):441–452.

Fleming, R. J., T. M. Kaneshige, W. E. McGovern, and T. E. Bryan, 1979. The Global Weather Experiment II. The second special observing period, *Bulletin of the American Meteorological Society*, 60:1316-1322.

Fore, L.S., J.R. Karr, and R. Wisemann, 1996. Assessing invertebrates responses to human activities: evaluating alternative approaches, *Journal of North American Benthological Society*, 15:212–231.

Foster, D.A., and A.J.W. Gleadow, 1992. The morphotectonic evolution of rift-margin mountains in central Kenya: Constraints from apatite fission-track thermochronology, *Earth and Planetary Science Letters*, 113:157-171.

Franklin, J., T. Logan, C. E. Woodcock, and A. H. Strahler, 1986. Coniferous forest classification and inventory using Landsat and digital terrain data, *IEEE Transactions on Geoscience and Remote Sensing,* 24:139.

Frostick, L.E., and I. Reid, 1989. Is structure the main control of river drainage and sedimentation in rifts?, *Journal of African Earth Sciences*, 8:165-182.

Gans, P.B., 1997. Large-magnitude Oligo–Miocene extension in southern Sonora: Implications for the tectonic evolution of northwest Mexico, *Tectonics*, 16:388–408.

Garbrecht, J. and L.W. Martz, 1997. TOPAZ Version 1.20: An automated digital landscape analysis tool for topographic evaluation, *drainage identification, watershed segmentation and subcatchment parameterization* - Overview. Rep.# GRL 97-2, Grazinglands Research Laboratory, USDA, Agricultural Research Service, El Reno, Oklahoma, 21 p.

Garcı′a, J.H., W.W. Li, R. Arimoto, R. Okrasinski, J. Greenlee, and J. Walton, et al., 2004. Characterization and implication of potential fugitive dust sources in the Paso del Norte region, *Science of the Total Environment*, 325:95–112.

Gastil, G., J. Minch and R. P. Phillips 1983. The geology and ages of the islands, *Island biogeography in the Sea of Cortez* (T. J. Case and M. L. Cody, ediors), University California Press, Berkeley, pp. 13–25

Gastil, R. G., R. P. Phillips, and E. C. Allison, 1975. Reconnaissance geology of the state of Baja California, *Geological Society of America Memoir*,140:170 p.

Gawthorpe, R.L., and J.M. Hurst, 1993. Transfer zones in extensional basins: their structural style and influence on drainage development and stratigraphy, *Journal Geological Society*, 150:1137-1152.

Gawthorpe, R.L., and M.R. Leeder, 2000. Tectono-sedimentary evolution of active extensional basins, *Basin Research*, 12:195-218.

Gelabert, B., J.J. Fornos, J.E. Pardob, V.M Rossello, F. Segurac, 2005. Structurally controlled drainage basin development in the south of Menorca (western Mediterranean, Spain), *Geomorphology* 65:139–155.

Gilchrist, A.R., and M.A. Summerfield, 1990. Differential denudation and flexural isostasy in formation of rifted-margin upwarps, *Nature,* 346:739-742.

Ginat, H., E. Zilberman, and R. Amit, 2002. Red sedimentary units as indicators of Early Pleistocene tectonic activity in the southern Negev desert, Israel, *Geomorphology,* 45:127–146.

Ginat, H., Y. Enzel, and Y. Avni, 1998. Translocated Plio-Pleistocene drainage systems along the Arava fault of the Dead Sea transform, *Tectonophysics*, 284(1-2):151-160.

Goa, J., 1997. Resolution and Accuracy of terrain representation by grid DEMs at Micro Scale, *International Journal of Geographical Information Science*, 11(2):199-212.

Goddu, S., S. Hu, and E. Appel, 2003. Time series and cluster analysis of a lacustrine section (heqing, yunnan province, china) spanning about last 1 ma, *Geophysical Research Abstracts*, 5: abstract # 06868.

Goff, J. A., E. A. Bergman, S. Solomon, 1987. Earthquake source mechanisms and transform fault tectonics in the Gulf of California, *Journal of Geophysical Research*, 92(10):485-510.

Goovaerts P., and G.M. Jacquez, 2004. Accounting for regional background and population size in the detection of spatial clusters and outliers using geostatistical filtering and spatial neutral models: the case of lung cancer in Long Island, New York. *International Journal of Health Geographics,* 3:1-14

Goovaerts, P., 1997. *Geostatistics for Natural Resources Evaluation*, Oxford University Press, New York, 483 p.

Gordon A.D., 1999. *Classification*, Chapman and Hall/CRC, Boca Raton, Florida, 2nd edition, 272 p.

Gordon, A.D., 1981. Classification: Methods for the Exploratory Analysis of Multivariate Data, Chapman and Hall, London, 193 p.

Grande J.A., J. Borrego, and J.A. Morales, 2000. Study of heavy metal pollution in the Tinto-Odiel estuary in Southwestern Spain using spatial factor analysis, *Environmental*, 39(10):1095-1101.

Grande J.A., J. Borrego, J.A. Morales, and M.L. de la Torre, 2003b. A description of how metal pollution occurs in the Tinto-Odiel rias (Huelva-Spain) through the application of cluster analysis, *Marine Pollution Bulletin* 46(4):475-480.

Granger, D.E., Kirchner, J.W., and Finkel, R.C., 1996. Spatially averaged long-term erosion rates measured from in situ-produced cosmogenic nuclides in alluvial sediment, *Journal of Geology*, 104:249-257.

Green, R. H., and P. A. Montagna, 1996. Implications for monitoring: study designs and interpretation of results, *Canadian Journal of Fisheries and Aquatic Sciences,* 53:2629-2636.

Griffith, D., 2002. Modeling spatial dependence in high spatial resolution hyperspectral datasets, *Journal of Geographical Systems*, 4:43–51

Güler, C., G. Thyne, J.E. McCray, and A.K. Turner, 2002. Evaluation of graphical and multivariate statistical methods for classification of water chemistry data, *Hydrogeology Journal,* 10:455–474.

Haack, B., and M. Bechdol, 2000. Integrating multisensor data and RADAR texture measures for land cover mapping, *Computers and Geosciences* 26(4):411-421.

Haala, N., and C. Brenner, 1999. Virtual city models from laser altimeter and 2D map data, *Photogrammetric Engineering and Remote Sensing,* 65(7):787-795.

Hack, J., 1957. Studies of longitudinal stream profiles in Virginia and Maryland, USGS, *Geological Survey Professional Paper*, 294-B, p. 45-97.

Hahn, M., and Statter, C., 1998. A scene labelling strategy for terrain feature extraction using multisource data, *ISPRS Commission III Symposium on Object Recognition and Scene Classification from Multispectral and Multisensor Pixels,* Vol. 32/3 (T. Schenk and A. Habib, editors), , Seiten, Columbus,Ohio, pp. 435–441.

Hamilton, W.B., 1961. Origin of the Gulf of California, *Geological Society of America Bulletin,* 72:1307-1318.

Hare, P. W., and T. W. Gardner, 1985. Geomorphic indicators of vertical neotectonism along converging plate margins, Nicoya Peninsula, Costa Rica, *Proceedings of the 15th Annual Binghamton Geomorphology Symposium*,*Tectonic Geomorphology* (M. Morisawa and J. T. Hack, editors), 15th September 1984, Allen and Un-win, Boston, pp. 90–104.

Harkins, N.W., D.K. Latta, D.J. Anastasio, F.J. Pazzaglia, 2002. Surficial and bedrock map of the Dixon Mountain 7.50 quadrangle, SW Montana, *Montana Bureau of Mines and Geology,* Open File Report 495, scale 1: 24,000.

Hartigan, J., 1975. *Clustering Algorithms*, John Wiley and Sons, New York, 366 p.

Harvey, A.M., and S.G. Wells, 1987. Response of quaternary fluvial systems to differential epeirogenic uplift, Aguas and Feos river systems, southeast Spain, *Geology,* 15:689-693.

Hausback, B.P., 1984. Cenozoic volcanic and tectonic evolution of Baja California, Mexico, *Geology of the Baja California Peninsula: Bakersfield, California, Pacific Section* (V.A. Frizzell, editor), Society of Economic Paleontologists and Mineralogists, 39:219–236.

Hay, S., C. Tucker, D. Rogers, and M. Packer, 1996. Remotely sensed surrogates of meteorological data for the study of the distribution and abundance of arthropod vectors of disease, *Annals of Tropical Medicine and Parasitology,* 90(1):1-19.

Hepner, G. F., T. Logan, N. Ritter, and N. Bryant, 1990. Artificial neural network classification using a minimal training set: comparison to conventional supervised classification, *Photogrammetric Engineering and Remote Sensing*, 56(5):469-473.

Herzfeld, U.C., 1999. Geostatistical interpolation and classification of remote sensing data from ice surfaces, *International Journal of Remote Sensing*, 20(2):307-327.

Hese, S., W. Lucht, C. Schmullius, M. Barnsley, R. Dubayah, D. Knorr, K. Neumann, et al., 2005. Global biomass mapping for an improved understanding of the CO2 balance-the earth observation mission carbon-3D. *Remote Sensing of Environment*, 94:94−104

Ho, T.K., J.J. Hull, and S.N. Srihari, 1994. Decision combination in multiple classifier systems, *IEEE Transactions on Pattern Analysis and Machine Intelligence*, 16**:**66-75.

Hoffer, R. M., and Staff, 1975. *Natural resource mapping in mountainous terrain by computer analysis of ERTS-l satellite data*, *Agricultural Experiment Station Research Bulletin* 919. Purdue University, West Lafayette, Indiana. 124 pp.

Holben, B.N., and C.O. Justice, 1980. The topographic effect on spectral response from nadir-pointing sensors, *Photogrammetric Engineering and Remote Sensing*, 49:1191–1200.

Holbrook, J.M., and S.A. Schumm, 1999. Geomorphic and sedimentary response of rivers to tectonic deformation: A brief review and critique of a tool for recognizing subtle epeirogenic deformation in modern and ancient settings, Special issue on Tectonics of Continental Interiors, *Tectonophysics*, 305:287-306.

Howard, A.D., 1994. A detachment-limited model of drainage basin evolution, *Water Resources Research*, 30:2261–2285.

Howard, A.D., and G. Kerby, 1983. Channel changes in badlands, *Geological Society of America Bulletin*, 94(6):739-752.

Hruby, T., 1987. Using similarity measures in benthic impact assessments, *Environmental Monitoring and Assessment*, 8:163–180.

Hsieh, M. L., P.L.K. Knuepfer, 2001. Middle–late Holocene river terraces in the Erhjen River Basin, southwestern Taiwan: implications of river response to climate change and active tectonic uplift, *Geomorphology*, 38:37–372.

Hugli, H., and W. Frei, 1983. Understanding anisotropic reflectance in mountainous terrain, *Photogrammetric Engineering and Remote Sensing*, 49:671–683.

Humphrey, N.F., and S.K. Konrad, 2000. River incision or diversion in response to bedrock uplift, *Geology*, 28:43–46.

Humphreys, E.D. and R.J. Weldon, 1991. Kinematic constraints on the rifting of Baja California, *The Gulf and Peninsular Province of the Californias, Chapter 12* (J.P. Dauphin and B.R.T. Simoneit, editors), *American Association of Petroleum Geologists Memoir* 47, pp. 217-229.

Hurtrez, J.E., and F. Lucazeau, 1999. Effect of drainage area on hypsometry from an analysis of small-scale drainage basins in the Siwalik Hills (Central Nepal), *Earth Surface Processes and Landforms*, 24:799–808.

Hurtrez, J.E., F. Lucazeau, J. Lave, and J.P. Avouac, 1999. Investigation of the relationships between basin morphology, tectonic uplift, and denudation from the study of an active fold belt in the Siwalik Hills, central Nepal, *Journal of Geophysical Research*, 104(6):12779–12796.

Isaaks, E.H., and R.M. Srivastava, 1989. *Applied Geostatistics*, Oxford University Press, New York, N.Y., 561 p.

Jackson, G.D., 1993. Growth zones within the statolith microstructure of the deepwater squid Moroteuthis ingens (Cephalopoda: Onychoteuthidae): evidence for a habitat shift?, *Canadian Journal of Fisheries and Aquatic Sciences,* 50:2366–2374.

Jenson, S.K. and J.O. Domingue, 1988. Extracting topographic structure from digital elevation data for geographic information system analysis, *Photogrammetric Engineering and Remote Sensing,* 54(11):1593-1600.

Jones, P. D., T. M. L. Wigley, C. K. Folland, D. E. Parker, J. K. Angell, S. Lebedeff, and J. E. Hansen, 1988. Evidence for global warming in the past decade, *Nature*, 332(790): 61-67.

Journel, A.G., 1993. Geostatistics, roadblocks and challenges (A. Soares, editor), Geostatistics-Troia, Kluwer Academic, Dordrecht, 1:213–224.

Journel, A.J., and C.J. Huijbregts, 1978. *Mining Geostatistics*, Academic Press, New York, N.Y., 600 p.

Kafri, U., and A. Heimann, 1994. Reversal of the palaeodrainage system in the sea of Galilee area as an indicator of the formation timing of the Dead Sea rift valley base level in northern Israel, Palaeogeography, Palaeoclimatology, *Palaeoecology*,109:101–109.

Kaiser, H.F.,1960. The application of electronic computers to factor analysis, *Educational and Psychological Measurement*, 20:141–51.

Kanellopoulos, I. et al., 1993. Integration of neural network and statistical image classification for land cover mapping, *Proceeding IGARSS 93*, 18-21 August 1993, Tokyo, pp. 511-513.

Kanellopoulos, I., A. Varfis, G. G. Wilkinson, and J. Me'gier, 1992. Land-cover discrimination in SPOT HRV imagery using an artificial neural network: a 20 class experiment, *International Journal of Remote Sensing*, 13:917-924.

Kanellopoulos, I., and G. G. Wilkinson, 1997. Strategies and best practice for neural network image classification, *International Journal of Remote Sensing,* 18(4):711-725.

Karig, D.E., and W. Jensky, 1972. The proto-Gulf of California, *Earth and Planetary Science Letters*, 17:169-174.

Karr, J. R., and T. E. Martin, 1981. Random numbers and principal components, Further searches for the unicorn, *The Use of Multivariate Statistics in Studies of Wildlife Habitat* (D. Capen, editor), US For. Serv. Gen Tech. Rep. RM-87, p. 20-24

Kaufman, L., and P. J. Rousseeuw, 1990. *Finding Groups in Data: An Introduction to Cluster Analysis*, John Wiley & Sons, Inc., New York, 368 p.

Keller E., and N. Pinter, 2001. *Active Tectonics, Earthquakes, Uplift and Landscape*, Earth Sciences Series, Prentice-Hall, Englewood Cliffs, New Jersey, 362 p.

Keller, E.A. and N. Pinter, 1996. *Active Tectonics*, Prentice Hall Inc., Englewood Cliffs, New Jersey, 338 p.

Keller, E.A., 1986. Investigation of active tectonics: using of surficial earth processes, *Active Tectonics* (R. E Wallace, editor), National Academic Press, Washington, pp.136-147.

Keller, E.A., and N. Pinter, 2002. *Active Tectonics*, 2nd edition, Prentice Hall, Upper Saddle River. New Jersey, 338 p.

Kerr, J.W., 1982. History and implications of the Nares conict, *Nares Strait and the drift of Greenland, A conict in plate tectonics, Meddr. Grnland* (P.R. Dawes and J.W. Kerr, editors), *Geosciences*, 8:37-49.

Ketting, R. L., and D. A. Landgrebe, 1976. Computer classification of remotely sensed multispectral image data by extraction and classification of homogeneous objects, *IEEE Transactions on Geoscience Electronics*, 14(1):19-26.

Key, J., A. Maslanic, and A. J. Schweiger, 1989. Classification of merged AVHRR and SMMR arctic data with neural networks, *Photogrammetric Engineering and Remote Sensing*, 55:1331-1338.

Kirby, E., and K. Whipple, 2001. Quantifying differential rock-uplift rates via stream profile analysis, *Geology*, 29(5):415-418,

Kirby, E., K.X. Whipple, W. Tang, and C. Zhiliang, 2003. Distribution of active rock uplift along the eastern margin of the Tibetan Plateau: Inferences from bedrock channel longitudinal profiles, *Journal of Geophysical Research – Solid Earth*, 108(B2):2217-2240.

Kobor, J. S. and J.J. Roering, 2004. Systematic variation of bedrock channel gradients in the central Oregon Coast Range: Implications for rock uplift and shallow landsliding, *Geomorphology*, 62:239-256.

Krige, D.G., 1951. A statistical approach to some basic mine evaluation problems on the Witswatersrand, *Journal of the Chemical, Metallurgical and Mining society of South Africa*, 52:119-39.

Krige, D.G., 1966. Two-dimensional weighted moving average trend surface for ore evaluation, *Journal of the South African Institute of Mining and Metallurgy*, 66:13-38.

Krzyszkowski D., B. Przybylski, and J. Badura, 2000. The role of neotectonics and glaciation on terrace formation along the Nysa Klodska River in the Sudeten Mountains (southwestern Poland), *Geomorphology*, 33:149−166.

Kühni, A., and O.A. Pfiffner, 2001. Drainage pattern and tectonic forcing: a model study for the Swiss Alps, *Basin Research*, 13:169-197.

Kunz, D., K. Schilling, and T. Vögtle, 1997. A new approach for satellite image analysis by means of a semantic network, *Semantic Modeling* (W. Förstner and L. Plumer, editors), Birkhäuser, Basel, pp. 20-36.

Kupfersberger, H., and C.V. Deutsch, 1999. Methodology for integrating analogue geologic data in 3-D variogram modeling, *AAPG Bulletin*, 83(8):1262-1278.

Kusky, T.M., and F. El-Baz, 2000. Neotectonics and fluvial geomorphology of the of the Northern Sinai peninsula, *Journal of African Earth Sciences*, 31(2):213-235.

Kyriakidis, P.C., A.M. Shortridge, and M.F. Goodchild, 1999. Geostatistics for conflation and accuracy assessment of digital elevation models, *International Journal of Geographical Information Science*, 13(7):677-707.

Lambrakis, N., A., Antonakos, and G. Panagopoulos, 2004. The use of multicomponent statistical analysisin hydrogeological environmental research, *Water Research*, 38(7):1862-1872.

Lang, H., R.,Welch, Y. Miyazaki, , B. Bailey, and G. Kelly, 1996. The ASTER along-track stereo experiment: a potential source of global DEM data in the late 1990's.

Proceedings of SPIE, 21 October, 1996, vol. 2817, *The International Society for Optical Engineering*, pp. 95– 97.

Larson, R. L., H.W. Menard, and S. M. Smith, 1968. Gulf of California: A result of ocean-floor spreading and transform faulting, *Science,* 161:781–784.

Latrubesse, E.M., A. Rancy, 2000. Neotectonic influence on tropical rivers of southwestern Amazon during the late quaternary: the Moa and Ipixuna river basins, Brazil, *Quaternary International*, 72(1):67-72.

Lebart, L., A. Morineau, and M. Piron, 1995. *Statistique Exploratoire Multidimensionnelle*, Dunod, Paris, France, 439p

Ledesma-Vázquez J., and M.E. Johnson, 2001. Miocene-Pleistocene tectono-sedimentary evolution of Bahía Concepción Region, Baja California Sur (Mexico), *Sedimentary Geology*, 144:83-96.

Lee, J., M.M. Miller, R. Crippen, B. Hacker, and J. Ledesma-Vasquez, 1996. Middle Miocene extension in the Gulf Extensional Province, Baja California: Evidence from the southern Sierra Juarez, *Geological Society of America Bulletin*, 108: 505-525.

Leeder, M.R., and R.L. Gawthorpe, 1987. Sedimentary models for extensional tilt-block/half-graben basins, *Continental Extensional Tectonics* (M. P Coward, J. F Dewey and P. L Hancock editors), *Geological Society of America Special Publication* 28:139–152.

Le Hegarat-Mascle, S., A. Quesney, and D. Vidal-Madjar, 2000. Land cover discrimination from multitemporal ERS images and multispectral Landsat images: a study case in an agricultural area in France, *International Journal of Remote Sensing,* 21: 435-456.

Leica, 2005. *Manual of ERDAS Software*, v. 8.6. ERDAS Inc., Atlanta, Georgia, 686 p.

Leprieur, C.E., J.M. Durand, and J.L. Peyron, 1988. Influence of topography on forest reflectance using Landsat thematic mapper and digital terrain data, *Photogrammetric Engineering and Remote Sensing*, 54:491–496.

Leser, C., 2002. Operationelle Biotoptypenkartierung mit HRSC-Daten – Probleme und Lösungsansätze, *GIS und Fernerkundung: Neue Sensoren – Innovative Methoden* (T. Blaschke, editor), Wichmann Verlag, Heidelberg, pp. 88-97.

Lewinski, S., 2006. Applying fused multispectral and panchromatic data of Landsat ETM+ to object oriented classification, *Proccedings of the 26th EARSeL Symposium, New Developments and Challenges in Remote Sensing*, May 29-June 2, 2006, Warsaw, Poland, pp.1-7.

Lillesand, T.M., and R.W. Kiefer, 1987. *Remote-Sensing and Image Interpretation*, JohnWiley and Sons, New York, N.Y., 736 p.

Liu, X. H., 2000. Change detection for urban growth modeling: an artificial neural network approach, *Proceeding of 4th International Conference on Integrating GIS and Environmental Modeling (GIS/EM4): Problems, Prospects and Research Needs*, 2-8 September, 2000, Banff, Alberta, Canada, Abstract.

Lloyd, C.D., and P.M. Atkinson, 2002. Deriving DSMs from LiDAR data with kriging, *International Journal of Remote Sensing*, 23(12):2519–2524.

Lobo, A., 1997. Image segmentation and discriminant analysis for the identification of land cover units in ecology, *IEEE Transactions on Geoscience and Remote Sensing*, 35:1136–1145.

Lohani, B. and D.C. Mason, 1999. Construction of a digital elevation model of the Holderness Coast using the waterline method and Airborne Thematic Mapper data, *International Journal of Remote Sensing*, 20(3): 593-607.

Lonsdale, P., 1989. Geological and tectonic history of the Gulf of California, *The Eastern Pacific Ocean and Hawaii* (D. Winterer, M. Hussong and R. W. Decker, editors), *Geological Society of America,* Boulder, Colorado., The Geology of North America, v. N, pp. 499-521.

Lonsdale, P., 1991. Structural patterns of the Pacific floor offshore of peninsular California, *The gulf and peninsular province of the Californias* (J.P. Dauphin and B.T. Simoneit, editors), *American Association of Petroleum Geologists, AAPG Memoir,* Tulsa, Oklahoma, 47:87–125.

Love, D. A., H. C. Alan, and G. Keith, 2004. The lithologic, stratigraphic, and structural setting of the giant antamina copper-zinc skarn deposit, Ancash, Peru, *Economic Geology,* 99:887–916.

Lyle, M., and G.E. Ness, 1991. The Opening of the Southern Gulf of California, *The Gulf and Peninsular Province of the California*, (J.P. Dauphin and B.R.T. Simoneit, editors), *American Association of Petroleum Geologists*, *AAPG Memoir,* Tulsa, Oklahoma, pp. 403-423.

Maddy, D., D.R. Bridgeland, and C.P. Green, 2000. Crustal uplift in southern England: evidence from the river terrace records, *Geomorphology,* 33:167-181.

Mammerickx, J., and K.D., 1982. Klitgord, Northern East Pacific Rise - evolution from 25 My Bp to the present, *Journal of Geophysical Research*, 87(8):6751-6759.

Mark, D., 1975. Geomorphometric parameters, a review and evaluation, *Geographiska Annaler,* 57(A):1461-1467.

Martin, Y., and M. Church, 2004. Numerical modeling of landscape evolution, geomorphological prospectives, *Progress in Physical Geography*, 28:317-39.

Mather P., Tso B., 2001. *Remote Sensing Imagery Analysis and Classification,* An Advanced Course, Springer Verlag, Berlin.

Mather, A., 2000. Adjustment of a drainage network to capture induced base-level change: an example from the Sorbas Basin, SE Spain, *Geomorphology*,34:271–289.

Mather, G., F. Verstraten, and S. Anstis, 1998. *The Motion Aftereffect: A Modern Perspective*, MIT Press, Cambridge, Massachusetts , 232 p.

Mather, P.M., 1987. *Computer processing of Remotely Sensed Image, An introduction*, John Wiley and Sons, New York, N.Y., 357p.

Mather, P.M., and J.C. Doornkamp, 1970. Multivariate analysis in geography, with particular reference to drainage basin morphometry, *Transactions of the Institute of British Geographers*, (51):163-187.

Matsuyama, T., 1989, Expert systems for image processing: knowledge-based composition of image analysis processes, *Computer Vision, Graphics,&Image Processing,* 48:22-49.

McClay, K.R., and P.G. Ellis, 1987. Analogue models of extensional fault geometry's, *Continental Extensional Tectonics* (M.P. Coward, T.S. Daltaban, and H.D. Johnson, editors), *Geological Society of London Special Publications*, 28:109–125.

McDowell, F.W., and S.E. Clabaugh, 1979. Ignimbrites of the Sierra Madre Occidental and their relation to the tectonic history of western Mexico, *Ash-Flow Tuffs* (C.E. Chapin and W.E. Elston, editors), *Geological Society of America Special Paper*, 180:113–124.

McLachlan, G.J., and K.E. Basford, 1988. *Mixture Models: Inference and Applications to Clustering*, Marcel Dekker, New York, N.Y., 253p.

Melloul, A., and M. Collin, 1992. The principal components statistical method as a complementary approach to geochemical methods in water-quality factor identification. Application to the coastal plain aquifer of Israel, *Journal of Hydrology*, 140:49-73.

Merritts, D., and K.R. Vincent, 1989. Geomorphic response of coastal streams to low, intermediate, and high rates of uplift, Mendocino junction region, northern California, *Geological Society of America Bulletin*, 101:1373–1388.

Miranda, A.C., H.S. Miranda, J. Lloyd, J. Grace, J.A. Mcintyre, P. Meir, P. Riggan, R. Lockwood, and J. Brass, 1996. Carbon dioxide fluxes over a cerrado sensu stricto in central Brazil, *Amazonian Deforestation and Climate* (J.H.C Gash, C.A. Nobre,., J.M. Roberts, R.L. Victoria, editors) , first edition, JohnWiley and Sons, New York, N.Y., pp. 353–363.

Mitri G.H., and Gitas I.Z., 2002. The development of an object-oriented classification model for operational burned area mapping on the Mediterranean island of Thasos using LANDSAT TM images, *IV International Conference on Forest Fire*

Research (D.X. Viegas, editor), 18-23 November, 2002, Millpress, Luso, Portugal, 79p.

Moik, J. P., 1980. *Digital Processing of Remotely Sensed Images*, NASA SP-431 Washington, DC, National Aeronautics and Space Administration, 431p.

Molnar, P., 1973. Fault plane solutions of earthquakes and direction of motion in the Gulf of California and on the Rivera Fracture Zone, *Geological Society of America Bulletin*, 84:1651–1658.

Moloney, K., O. Chic, and N. Chiarello. 1998. Analysis of fine-scale spatial pattern of a grassland from remotely-sensed imagery and field collected data. Land. *Ecology*, 13:111–131.

Monbet V., and M. Prevosto, 2000. Bivariate simulation of non stationary and non Gaussian observed processes: Application to sea state parameters, *Applied Ocean Research,* 23:139-146.

Monecke, K., J. Winsemann, and J. Hanisch, 2001. Climatic response of quaternary alluvial deposits in the upper Kali Gandaki valley (West Nepal), *Global and Planetary Change,* 28:293–302.

Montgomery, D. R., and E. Foufoula-Georgiou, 1993. Channel network source representation using digital elevation models, *Water Resources Research*, 29(12):3925–3934.

Montgomery, D.R., 2001. Slope distributions, threshold hillslopes, and steady-state topography, *American Journal of Science*, 301:432–454.

Montgomery, D.R., and M.T. Brandon, 2002. Topographic controls on erosion rates in tectonically active mountain ranges, *Earth and Planetary Science Letters*, 201:481– 489.

Moore A.E., and P. Larkin, 2001. Drainage evolution in south-central Africa since the breakup of Gondwana, *South African Journal of Geology*, 104:47-68.

Moore, A.W., and J.S. Russell, 1967. Comparison of coefficients and grouping procedures in numerical analysis of soil trace element data, *Geoderma,* 1:129–158.

Moore, I. D., R. B. Grayson, and A. R. Ladson., 1991. Digital terrain modelling: A review of hydrological, geomorphological and biological applications, *Hydrology Proceedings,* 5:3-30.

Murtagh, F., 1985. *Multidimensional Cluster Algorithms*, Lectures in Computational Statistics, Physica Verlag, Vienna, 15p.

Nava-Sanchez, E., G. Gorsline, A. Molina-Cruz, 2001. The Baja California peninsular borderland: structural and sedimentological characteristics, *Sedimentary Geology,* 144:63–82.

Nicholson, C., C.C. Sorlien, T. Atwater, J.C. Crowell and B.P. Luyendyk, 1994. Microplate capture, rotation of the western Transverse Ranges, and initiation of the San Andreas transform as a low-angle fault system, *Geology*, 22:491–495.

Normark,W. R., and J. R. Curray, 1968. Geology and structure of the tip of Baja California, Mexico, *Geological Society of America Bulletin*, 79:1589–1600.

Norris, R. H., and A. Georges, 1993. Analysis and interpretation of benthic macro-invertebrate surveys, *Freshwater Biomonitoring and Benthic Macro-Invertebrates* (D. M. Rosenberg, and V. H. Resh, editors), Chapman and Hall, London and NewYork, pp. 234–286.

Nowak, B., 1998. Contents and relationship of elements in human hair for a non-industrialized population in Poland, *Science of the Total Environment*, 209:59–68.

Ochoa-Landín, L., 1998. *Geological, Sedimentological and Geochemical Studies of the Boleo Cu-Co-An Deposit, Santa Rosalía, Baja California, Mexico*, Ph.D. dissertation, University of Arizona, Tucson, , 148 p.

Ohmori, H., 1993. Changes in the hypsometric curve through mountain building resulting from concurrent tectonics and denudation, *Geomorphology*, 8(4):263-277.

Olea, R.A., 1994. Fundamentals of semivariogram estimation, modeling, and usage, *Stochastic Modeling and Geostatistics Principles, Methods and Case Studies* (J. Yarus and R. L. Chambers, editors), American Association of Petroleum Geologists*,* Tulsa, Oklahoma, pp.27-35.

Oliver, M.A., R. Webster, and K. Slocum, 2000. Filtering SPOT imagery by kriging analysis, *International Journal of Remote Sensing*, 21(4): 735–752.

Oliver, M.A., R. Webster, and J. Gerrard, 1989a. Geostatistics in physical geography. I. Theory, *Transactions of the Institute of British Geographers*, 14(3):259-69.

Oliver, M.A., Webster, R., and Gerrard, J., 1989b. Geostatistics in physical geography. II. Applications, *Transactions of the Institute of British Geographers*, 14(3):270-80.

Ortlieb, L., 1980. Neotectonics from marine terraces along the Gulf of California, *Earth Rheology, Eustasy, and Isostasy* (N.A. Mörner, editor), Wiley Interscience, New York, pp. 497–504.

Palmer, T. N., 1993. Extended-range prediction and the Lorenz model*, Bulletin of the American Meteorological Society*, 74:49-65.

Paola, J. D. and R. A. Schowengerdt, 1994. Comparisons of neural networks to standard techniques for image classification and correlation, *Proceedings of the International Geoscience and Remote Sensing Symposium* (IGARSS 94), Pasadena, California, 8-12 August, vol. 3 (Piscataway NJ: I.E.E.E. Press), pp. 1404-1406.

Paola, J. D., and R. A. Schowengerdt, 1994. Comparisons of Neural Networks to Standard Techniques for Image Classification and Correlation, *Proceedings of the 14th Annual International Geoscience and Remote Sensing Symposium,* August 8-12, 1994, Pasadena, Calefornia, 3:1404-1406,.

Pavoni, N., H. Maurer, P. Roth, and N. Deichmann, 1997. Seismicity and seismotectonics of the Swiss Alps, *Deep Structure of the Alps, Results of NRP20*, Birkhauser, Basel, Switzerland, pp. 241–250.

Pekkarinen, A., 2002. A method for the segmentation of very high spatial resolution images of forested landscapes, *International Journal of Remote Sensing,* 23(14):2817-2836.

Pienitz, R. P., J. P. Smol, and D. R. S. Lean, 1997a. Physical and chemical limnology of 59 lakes located between the southern Yukon and the Tuktoyaktuk Peninsula, Northwest Territories (Canada), *Canadian Journal of Fisheries and Aquatic Sciences*, 54:330–346.

Pienitz, R. P., J. P. Smol, and D. R. S. Lean, 1997b. Physical and chemical limnology of 24 lakes located between Yellowknife and Contwoyto Lake, Northwest Territories (Canada), *Canadian Journal of Fisheries and Aquatic Sciences*, 54:347–358.

Powell, C.McA., Z.X. Li, M.W. McElhinny, J.G. Meert, and J.K. Park, 1993. Paleomagnetic constraints on the timing of the Neoproterozoic breakup of Rodinia and the Cambrian formation of Gondwana, *Geology*, 21:889-892.

Prat, N. F., M. A. Puig, G. Gonzalez, M. F. Tort, and M. Estrada, 1984. Llobregat, *Ecology of European Rivers* (B. A. Whitton, editor), Blackwell Scientific, London, UK, pp. 527–552

Quinn, H.A., and T.M. Cronin, 1984. Micro-paleontology and depositional environments of the Imperial and Palm Spring Formations, Imperial Valley, California, *The Imperial Basin, Tectonics, Sedimentation and Thermal Aspects* (C.A. Rigsby, editor), *Society of Economic Paleontologists and Mineralogists*, 40:71-85.

Rabus, B., M. Eineder, A. Roth, and R. Bamler, 2003. The shuttle radar topography mission- a new class of digital elevation models acquired by spaceborne radar, *Photogrammetry & Remote Sensing*, 57: 241-262.

Reidel, and K. Schröter, 2005. Global biomass mapping for an improved understanding of the CO2 balance—the Earth observation mission Carbon-3D, *Remote Sensing of the Environment*, 94:94-104.

Replumaz, A., R. Lacassin, P. Tapponnier, and P.H. Leloup, 2001. Large river offsets and Plio-Quaternary dextral slip rate on the Red River fault (Yunnan, China), *Journal of Geophysical Research*, 106:819–836.

Richards, J.A., D.A. Ndgrebe., and P.H. Swain, 1982. A means for utilising ancillary information in multispectral classification, *Remote Sensing of Environment,* 12:463-77.

Richards, J., 1993. *Remote Sensing Digital Image Analysis*, 2nd edition, Springer-Verlag New York, 340 p.

Richards, J.A., and X. Jia, 1999. *Remote Sensing Digital Image Analysis, An Introduction*, 3rd edition. Springer-Verlag, Germany, 363 p.

Rockwell, T.K., E.A. Keller, M.N. Clark, and D.L. Johnson, 1984. Chronology and rates of faulting of Vertura river terraces, California, *Bulletin of the Geological Society of America*, 95:146–1474.

Roe, G.H., D.R. Montgomery, and B. Hallet, 2002. Effects of orographic precipitation variations on the concavity of steady-state river profiles, *Geology*, 30:143–146.

Rossi, R.E., J.L. Dungan, and L.R. Beck, 1994. Kriging in the shadows: geostatistical interpolation for remote sensing, *Remote Sensing of Environment*, 49:32-40.

Sabater, F., J. Amengol, and S. Sabater, 1989. Measuring discontinuities in the Ter River, *Regulated Rivers: Research and Management,* 3**:**133–142.

Sabater, F., J. Armengol, and S. Sabater. 1991. Physical–chemical disturbances associated with spatial and temporal variation in a Mediterranean river, *Journal of the North American Benthological Society,* 10:2–13.

Sahin, A., S. G. Ghori, A. Z. Ali, H. F. El-Sahn, H. M. Hassan, and A. Al-Sanounah, 1998. Geological Ccontrols of variograms in a complex carbonate reservoir, eastern province, Saudi Arabia, *Mathematical Geology*, 30(3):309-322.

Saporta, G., 1990. *Probabilités, Analyse des Données et Statistique,* Editions Technip, Paris, France, 493p.

Savian, F.R., and D. Landgrebe, 1991. A survey of decision tree classifier methodology, *IEEE Transaction on Systems*, *Man and Cybernetics*, 21(3):660-674.

Sawlan, M.G., and J.G. Smith, 1984. Petrologic characteristics, age and tectonic setting of Neogene volcanic rocks in northern Baja California Sur, Mexico, *Geology of the Baja California Peninsula: Pacific Section* (J. V. A. Frizzell, editor), *Society of Economic Paleontologists and Mineralogists*, pp. 219–236.

Schlunegger, F., and M. Hinderer, 2001. Crustal uplift in the Alps: why the drainage pattern matters, *Terra Nova*, 13:425-432.

Schlunegger, F., R. Slingerland, and A. Matter, 1998. Crustal thickening and crustal extension as controls on the evolution of the drainage network of the central Swiss Alps between 30 Ma and the present: constraints from the stratigraphy of the North Alpine Foreland Basin and the structural evolution of the Alps, *Basin Research*, 10:197–212.

Schmidt, E.K., 1975. *Plate Tectonics, Volcanic Petrology and Ore Formation of the Santa Rosalía Area, Baja California, Mexico*, MA.Thesis, University of Arizona, Tucson, 194 p.

Schorghofer, N., and D. H. Rothman, 2001. Basins of attraction on random topography, *Physical Review*, 63:26-112.

Schowengerdt, R. A., 1997. *Remote Sensing: Models and Methods for Image Processing*, 2nd edition, Academic Press, San Diego, California, 522 p.

Schumm, S. A., 1977. *The Fluvial System*, John Wiley and Sons, New York, N.Y., 338 pp.

Seeber, L., and V. Gornitz, 1983. River profiles along the Himalayan arc as indicators of active tectonics, *Tectonophysics*, 92:335–367.

Seidl, M.A., and W.E. Dietrich, 1992. The problem of channel erosion into bedrock, *Catena*, supplement, 23:101–124.

Seidl, M.A., J.K. Weissel, and L.F. Pratson, 1996. The kinematics and pattern of escarpment retreat across the rifted continental margin of SE Australia, *Basin Research*, 12:301-316.

Sheps, K., 2004. *Quantitative Paleoenvironmental Analysis of Carbonate Platform Sediments on the Marion Plateau (NE Australia, ODP Leg 194),* MA. Thesis, Univirsity of South Florida, Tampa, 105 p.

Silva A.M., Souza Filho C.O., Toledo C.L.B., and Dantas E.C. 2003. Amalgamation of different crustal blocks in the southernmost part of the São Francisco Craton, constrained by airborne geophysical data, Brazil 14-18 September, 2003*, Brazil Geophysical Society*, 8th International Geophysical Congress, Rio de Janeiro.

Skidmore, A.K., B.J. Turner, W. Brinkhof, and E. Knowles, 1997. Performance of a neural network: mapping forests using GIS and remotely sensed data, *Photogrammetric Engineering and Remote Sensing,* 63:501-514.

Skidmore, A.K., W., Wietske, K. Schmidt, and L. Kumar, 1997. Use of remote sensing and GIS for sustainable land management, *ITC Journal,* ¾:1-15.

Sklar, L.S., and W.E. Dietrich, 1998. River longitudinal profiles and bedrock incision models: Stream power and the influence of sediment supply, Rivers Over Rock: Fluvial Processes in Bedrock Channels (K. Tinkler and E.E. Wohl, editors), *American Geophysical Union Geophysical Monograph,* 107:237–260.

Sklar, L.S., and W.E. Dietrich, 2001. Sediment and rock strength controls on river incision into bedrock, *Geology*, 29:1087–1090.

Smith ,T. S., S. Herrero, and T. D. Debruyn, 2005. Alaskan brown bears, habituation and humans, *Ursus,* 16:1–10.

Smith, D. L., P.B. Gans, and E.L. Miller, 1991. Palinspastic restoration of Cenozoic extension in the central and eastern Basin and Range Province at latitude 39-40 degrees N, *Geology and Ore Deposits of the Great Basin* (G. L. Raines, R.E. Lisle, R.W. Schafer and W.H. Wilkinson, editors), symposium proceedings, April 1–5, 1990, Reno, NV, *Geological Society of Nevada*, pp. 75-86.

Smith, T.R. and F.P. Bretherton, 1972. Stability and the conservation of mass in drainage basin evolution, *Water Resources Research,* 8:1506-1529.

Smith, V. H., B. L. Foster, J. P. Grover, and R. D. Holt, et al., 2005. Phytoplankton species richness scales consistently from laboratory microcosms to the world's oceans, *Proceedings of the National Academy of Science*, January 4, 2005, 102:4393–4396.

Smosna, R., and S.M. Warshauer, 1979. A scheme for multivariate analysis in carbonate petrology with an example from the Silurian Tonoloway Limestone, *Journal of Sedimentary Petrology*, 49:257-271.

Snyder, N. P., K. X. Whipple, G. E. Tucker, and D. J. Merritts, 2000. Landscape response to tectonic forcing: digital elevation model analysis of stream profiles in the mendocino triple junction region, Northern California, *Geological Society of American Bulletin*, 112:1250.

Solaiman and M.C. Mouchot, 1994. A comparative study of conventional and Neural Network classification of multispectral data, *Intemational Geoscience and Remote Sensing Symposium*, IGARSS'94, August 8-12, 1994, Pasadena, California, pp. 8-12.

Spencer, J. E., and W. R. Normark, 1979. Tosco-Abreojos fault zone: A Neogene transform plate boundary within the Pacific margin of southern Baja California, *Geology*, 7:554–557.

St. Onge, B. A., and F. Cavayas, 1997. Automated forest structure mapping from high resolution imagery based on directional semivariogram estimation, *Remote Sensing and Environment*, 61:82-95.

Stewart-Oaten, A., 1996. Problems in the analysis of environmental monitoring data. *In*: Schmitt RJ, Osenberg CW, editors. Detecting ecological impacts: concepts and applications in coastal habitats, *Academic*, pp. 109–131.

Stock, J. M., and K. V. Hodges, 1989. Pre-Pliocene extension around the Gulf of California and the transfer of the Baja California peninsula to the Pacific plate, *Tectonics*, 8:99-115.

Stock, J.D., and D.R. Montgomery, 1999. Geologic constraints on bedrock river incision using the stream power law, *Journal of Geophysical Research*, 104:4983-4993.

Stock, J.M., and J. Lee, 1994. Do microplates in subduction zones leave a geological record?, *Tectonics*, 13 (6):1472–1487.

Stohr, C. J., and T. R. West, 1975. Terrain and look angle effects upon multispectral scanner response, *Photogrammetric Engineering and Remote Sensing*, 51:229–235.

Stokes, M., and A.E. Mather, 2000. Response of Plio-Pleistocene alluvial systems to tectonically induced base-level changes, Vera Basin, SE Spain, *Geological Society of London*, 157:303-316.

Stokes, M., and A.E. Mather, 2003. Tectonic origin and evolution of a transverse drainage: the Rio Almanzora, Betic Cordillera, SE Spain, *Geomorphology*, 50:59-81.

Stouthamer, E., and H.J.A., Berendsen, 2000. Factors controlling the Holocene avulsion history of the Rhine-Meuse delta (The Netherlands), *Journal of Sedimentary Research*, 70(5):1051-1064.

Strahler, A. H., T. L. Logan, and N. A. Bryant, 1978. Improving forest cover classification accuracy from LANDSAT by incorporating topographic information, *Proceedings of the 12th International Symposium on Remote Sensing of the Environment,* 13–16 October, 1969, University of Michigan, Ann Arbor, Michigan, pp. 927-942.

Strahler, A. N., 1952. Hypsometric (areal-altitude) analysis of erosional topography, *Bulletin Geological Society of America*, 63:1117-1142.

Streeting, M., and Hamilton, C., 1991. An economic analysis of the forests of south-eastern Australia, *Resource Assessment Commission Research*, Paper no. 5, Canberra, December.

Suarez-Vidal, F., R. Armijo, G. Morgan, P. Bodin, and R. G. Gastil, 1991. Framework of recent and active faulting in northern Baja California, *The Gulf and Peninsula Province of the California* (J. P. Dauphin and B. R. T. Simoneit, editors), *American Association of Petroleum Geologists Memoir,* 47:285–300.

Summerfield, M.A., 1991. Sub-aerial denudation of passive margins: regional elevation versus local relief models, *Earth and Planetary Science Letters*, 102:460-469.

Sun, T., P. Meakin, and T. Jøssang, 2001. A computer model for meandering rivers with multiple bed load sediment sizes: 2. Computer simulations, *Water Resources Research*, 37(8):2243–2258.

Tarboton, D. G., 1997. A new method for the determination of flow directions and contributing areas in grid digital elevation models, *Water Resources Research*, 33(2): 309-319.

Tarboton, D. G., R. L. Bras, and I. Rodriguez-Iturbe, 1991. On the extraction of channel networks from digital elevation data, *Hydrologic Processes*, 5(1): 81-100.

Tebbens, L.A., and A. Veldkamp, 2000. Late Quaternary evolution of fluvial sediment composition: a modeling case study of the River Meuse, *Global and Planetary Change*, 27:187-206.

Teillet, P.M., B. Guindon, and D.G. Goodenough, 1982. On the slope-aspect correction of multispectral scanner data, *Canadian Journal of Remote Sensing*, 8:84–106.

Templ, M., 2003. *Cluster Analysis Applied to Geochemical Data*, Diploma Thesis, Vienna University of Technology, Vienna, Austria, 137pp.

Ten Brink, U., and T. Stern, 1992. Rift flank uplifts and hinterland basins: comparison of the transantarctic mountains with the great escarpment of southern Africa, *Journal of Geophysical Research*, 97:569-585.

Thomson, A.G., and C. Jones, 1990. Effects of topography on radiance from upland vegetation in North Wales, *International Journal of Remote Sensing*, 11:829–840.

Thomson, S. N., 1994. Fission track analysis of the crystalline basement rocks of the Oligo-Miocene late-orogenic extension and erosion, *Tectonophysics*, 238:331-352.

Thurstone, L. L.,1931. Multiple factor analysis, *Psychological Review,* 38:406-427.

Tortorici, L., C. Monaco, C. Tansi, and O. Cocina, 1995. Recent and active tectonics in the Calabrian arc (southern Italy), *Tectonophysics*, 243:37-55.

Tryon, R. C., 1939. *Cluster Analysis*, Edwards Brothers, Ann Arbor, Michigan, URL: <*http://www.statsoft.com/textbook/glosc.html*>

Tso B., and P. M. Mather, 2001. *Classification Methods for Remotely Sensed Data*, Taylor and Francis, New York,332 p.

Tucker, G. E., and R. L. Bras, 1998. Hillslope processes, drainage density and landscape morphology, *Water Resources Research*, 34(10):2751–2764.

Tucker, G. E., and R. L. Bras, 2000. A stochastic approach to modeling the role of rainfall variability in drainage basin evolution, *Water Resources Research,* 36(7):1953–1964,

Tucker, G.E., and R.L. Slingerland, 1996. Predicting sediment flux from fold and thrust belts, *Basin Research*, 8:329-349.

Umhoefer, P. J., and K. A. Stone, 1996. Description and kinematics of the SE Loreto basin fault array, Baja California Sur, Mexico:A positive field test of oblique-rift models, *Journal of Structural Geology*, 18:595–614.

Umhoefer, P.J., and R.J. Dorsey, 1997. Translation of terranes: A perspective from the central domain of the Baja California peninsula, Mexico, *Geology*, 25:1007–1010.

Umhoefer, P.J., M.E. Rusmore, and G.J. Woodsworth, 1994. Mesozoic tectonostratigraphy and Cretaceous-Tertiary structures in the Eastern Coast Belt near Chilko Lake (51° to 52° N), British Columbia: The difficulty of terrane analysis in adjacent arc and basinal successions, *Canadian Journal of Earth Sciences*, 31:1700-1713.

Umhoefer, P.J., P. Schiarizza, and M. Robinson, 2002. Relay Montain Group, Tyaughton Methow basin, southwest British Columbia: a major Middle Jurassic to Early Cretaceous terrane overlap assemblage, *Canadian Journal of Earth Sciences,* 39:1143–67.

van Tongeren, O. F. R., L. van Liere, R. D. Gulati, G. Postema, and P. J. Boesewinkel-De Bruyn, 1992. Multivariate analysis of the plankton communities in the

Loosdrecht lakes: relationship with the chemical and physical environment, *Hydrobiologia,* 233:105–117.

Veldkamp, A., and J.J. Van Dijke, 2000. Simulating internal and external controls on fluvial terrace stratigraphy: a qualitative comparison with the Maas record, *Geomorphology*, 33:225-236.

Verrios S., V. Zygouri, and S. Kokkalas, 2004. morphotectonic analysis in the eliki fault zone (Gulf of Corinth, Greece), *Bulletin of the Geological Society of Greece, Proceedings of the 10th International Congress*, Thessaloniki, 1706-1715.

Wackernagel, H., 2003. *Multivariate Geostatistics: An Introduction with Applications, 3rd ed*, Springer-Verlag, Berlin, Germany, 387 p.

Walker, J. P., and G. R. Willgoose, 1999. On the effect of digital elevation model accuracy on hydrology and geomorphology, *Water Resources Research*, 35:2259-2268.

Webster, R., M.A. Oliver, 1990. *Statistical Methods in Soil and Land Resource Survey*, Oxford Univ. Press, Oxford, 328 p.

Weibel, R., and M. Heller, 1991. Digital terrain modeling, *Geographical Information Systems: Principles and Applications* (D.J. Maguire, M.F. Goodchild and D.W. Rhind, editors), Longman, London, pp. 269-297.

Wells, S. G., T. F. Bullard, C. M. Menges, P. G. Drake, P. A. Karas, K. I. Kelson, J. B. Ritter, and J. R. Wesling, 1988. Regional variations in tectonic geomorphology along a segmented convergent plate boundary, Pacific coast of Costa Rica, *Geomorphology*, 1:239-266.

Wende R., 1995. Drainage and valley asymmetry in the Tertiary Hills of Lower Bavaria, Germany, *Geomorphology,* 14:255–265.

Whipple, K., 2004. Bedrock rivers and the geomorphology of active orogens, *Annual Review of Earth and Planetary Science*, 32:151–185.

Whipple, K.X., and G.E. Tucker, 1999. Dynamics of the stream power river incision model: implications for height limits of mountain ranges, landscape response timescales and research needs, *Journal of Geophysical Research,* 104(17):661-674.

Whipple, K.X., N.P. Snyder, and K. Dollenmayer, 2000b. Rates and processes of bedrock incision by the Upper Ukak River since 1912 Novarupta ash flow in the Valley of Ten Thousand Smokes, Alaska, *Geology,* 28:835–38.

Whipple, K.X., R.S. Anderson, and G.S. Dick, 2000a. River incision into bedrock: Mechanics and relative efficacy of plucking, abrasion, and cavitation, *Geological Society of America Bulletin*, 112:490–503.

Willgoose, G., R. L. Bras, and I. Rodriguez-Iturbe, 1991a. A coupled channel network growth and hillslope evolution model, 1, Theory, *Water Resources Research,* 27(7):1671–1684.

Willgoose, G., R. L. Bras, and I. Rodriguez-Iturbe, 1991b. A coupled channel network growth and hillslope evolution model, 2, Nondimensionalization and applications, *Water Resources Research*, 27(7):1685–1696.

Williams, D., 2000. Landsat 7 Enhanced Thematic Mapper-Plus (ETM+) Data Quality and Geographic Coverage, URL: http://landsat.gsfc.nasa.gov/announcements/feb02qa.html, NASA (last date accessed: 15 July 2004).

Wilson, J. P., and J. C. Gallant, 2000. Secondary topographic attributes, *Terrain Analysis: Principles and Applications* (J. P. Wilson and J. C. Gallant, editors), New York, John Wiley and Sons, pp. 87-131.

Winker, C. D., and S. M. Kidwell, 1996. Stratigraphy of a marine rift basin: Neogene of the western Salton Trough, California, *Field Conference Guidebook and Volume for the Annual Convention, San Diego, California* (P. L. Abbott and J. D. Cooper, editors), May, 1996, Bakersfield, California, Pacific Section, *American Association of Petroleum Geologist*, pp. 295-336.

Winker, C.D., 1987. *Neogene Stratigraphy of the Fish Creek - Vallecito Section, Southern California: Implications for Early History of the Northern Gulf of California and Colorado Delta*, Ph.D. dissertation, University of Arizona, Tucson, 494 p.

Wolock, D. M., and C. V. Price, 1994. Effects of digital elevation model map scale and data resolution on a topography based watershed model, *Water Resources Research* 30: 3041-3052.

Wright, J. F., D. Moss, P. D. Armitage, and M. T. Furse, 1984. A preliminary classification of running-water sites in Great Britain based on macroinvertebrate species and the prediction of community type using environmental data, *Freshwater Biology* 14:221–256.

Wright, J. F., M. T. Furse, and P. D. Armitage, 1993. RIVPACS: A technique for evaluating the biological quality of rivers in the UK, *European Water Pollution Control* 3:15–25.

Xue, G., A. Datta-Gupta, P. Valko, and T. A. Blasingame, 1996. Optimal transformations for multiple regression: application to permeability estimation from well logs, *SPE*, 35412: 85-93.

Yamaguchi, Y., A.B. Kahle, H. Tsu, T. Kawakami, and M. Pniel, 1998. Overview of advanced spaceborne thermal emission and reflection radiometer (ASTER), *IEEE Transactions on Geoscience and Remote Sensing*, 36(4): 1062–1071.

Yongming, H., D. Peixuan, C. Junji, and E.S. Posmentier, 2006. Multivariate analysis of heavy metal contamination in urban dusts of Xi'an, Central China, *Science of the Total Environment*, 355:176–186.

Young, F.J. and R.D. Hammer, 2000. Defining geographic soil bodies by landscape position, soil taxonomy, and cluster analysis, *Soil Science Society of American Journal*, 64(3):989-998.

Zanchi, A., 1994. The opening of the Gulf of California near Loreto, Baja California, Mexico: From basin and range extension to transtensional tectonics, *Journal of Structural Geology*, 16:1619–1639.

Zhang, W.H. and D.R. Montgomery, 1994. Digital elevation model grid size, landscape representation and hydrologic simulations, *Water Resources Research*, 30:1019-28.

Zovoili E., E. Konstantinidi, and I.K. Koukouvelas, 2004. Tectonic geomorphology of escarpments: the cases of Kompotades and Nea Anchialos Faults, *Bulletin of the Geological Society of Greece, Proceedings of the 10th International Congress*, Thessaloniki, 1716-1725.

Zwahlen, E.D., LBNL, and T.W. Patzek, 1997. A comparison of mapping schemes for reservoir characterization, *SPE,* 38264, p. 11

Zwolsman, J.J.G., G.W. Berger, and G.T.M. Van Eck, 1993. Sediment accumulation rates, historical input, postdepositional mobility, and retention of major elements trace metals in salt marsh sediments of the Scheldt estuary, SW-Netherlands, *Marine Chemistry,* 44:73–94.

Zwolsman, J.J.G., T.M. Bert, G.T.M. Van Eck, and H Cornelis, 1997. Geochemistry of dissolved trace metals (cadmium, copper, zinc) in the Scheldt estuary, southwestern Netherlands: impact of seasonal variability, *Geochimica et Cosmochimica Acta,* 61:1635–1652.

VITA

Name: Hesham Farouk El-Sobky

Address:
Department of Geology and Geophysics
Texas A&M University,
College Station, Texas 77843,
Phone: 979-458-0117
Fax: 979-845-6162,
e-mail: elsobky@geo.tamu.edu

Education

M.S. Degree in geology, September, 1999 (Structural geology & remote sensing), Geology Department, Alexandria University, Egypt.

B.S. Degree in Geology, September, 1999, Geology Department, Alexandria University, Egypt.

Experience

2002-2007
Research and Teaching Assistant at Department of Geology and Geophysics, Texas A&M University

1999-2001
Lecturer Assistant at Geology Dept., Faculty of Science, Alexandria University, Egypt.